An Integrated Nanoaperture Optical-Fiber Tweezer

for Developing Single-Photon Sources

by

Jamal Mehemed Ehtaiba

B.Sc., University of Tripoli, 1992

M.Sc., Al-Academeya Allibeya, 2007

A Dissertation Submitted in Partial Fulfillment of the

Requirements for the Degree of

**DOCTOR OF PHILOSOPHY**

in the Department of Electrical and Computer Engineering

An Integrated Nanoaperture Optical-Fiber Tweezer

for Developing Single-Photon Sources

by

Jamal Mehemed Ehtaiba

B.Sc., University of Tripoli, 1992

M.Sc., Al-Academeya Allibeya, 2007

Supervisory Committee

---

Dr. Reuven Gordon, Supervisor

(Department of Electrical and Computer Engineering)

---

Dr. Jens Bornemann, Departmental Member

(Department of Electrical and Computer Engineering)

---

Dr. Frank Van Veggel, Outside Member

(Department of Chemistry)

## ABSTRACT

In this thesis, an approach for developing single-photon sources at the 1550 nm wavelength will be demonstrated, based on optical trapping of luminescent upconverting nanoparticles. A single-photon source is a source that emits a single photon at a time, and hence it is a source of quantum bits that constitutes the basic building units in quantum computers and quantum communications. The approach exploits the plasmonic properties of gold films and the waveguiding characteristics of single-mode optical fibers (SMFs). We start by planar nanofabrication of subwavelength nanoapertures in a thin gold film based on finite difference time domain simulations for a peak transmission at the wavelength in question. Subsequently, using ultraviolet-curable epoxy adhesion material, a nanoaperture patterned on a gold film can be transferred to an SMF tip forming a nanoantenna enhanced optical fiber tweezer (NAFT). As a final step in building the optical tweezer, a test of the capability of the integrated optical fiber tweezer to trap 20 nm, and 30 nm polystyrene nanospheres, as well as luminescent upconverting nanoparticles (UCNPs), has been experimentally realized with encouraging results. In addition to the optical trapping of the luminescent nanoparticles, the nano aperture antenna can improve light coupling into the low-loss optical fiber guiding channel. Also, it could have a positive influence on enhancing the photon-emission rate through the Purcell effect. Furthermore, we have combined NAFT with a low-insertion-loss wave splitter, a wavelength-division multiplexer (WDM), to allow measuring the 1550 nm photon-emission statistics on a cooled superconducting nanowire single-photon detector (SNSPD) at $\sim 2.4^{o}$ K. Eventually, nanoantenna enhanced optical fiber tweezers can play an essential role in optical trapping towards developing single-photon sources and the emerging technology of quantum information processing, computation, and cryptography.

# Contents

# List of Tables

# List of Figures

# Acknowledgements

Praise be to Allah, and blessings and peace be upon the Messenger of Allah, but after:

I thank my supervisor, Dr. R. Gordon, for his guidance and support throughout this work. Thank you also to my supervisory committee members, Dr. F. V. Veggel and Dr. J. Bornemann. It was a great honor for me to have supervision and guidance from them.

Thank you to Dr. A. Saleh, the external examiner, and Dr. D. Hore, the Chair of the Oral Exam Committee, for their valuable time.

Thank you to those who helped me by a way or another throughout the time of my study program. I want to say to all of them thank you very much.

To the best of good companions, my mother, I say thank you so much. Thank you to my brothers and sisters for their care and encouragement. Thank you to my wife and my kids for their patience and support. Thank you to everyone.

Last but not least, all the gratitude to 17-Febrayer and the Ministry of Education of Libya for their trust and full financial support.

# Dedication

To the soul of my brother, Faraj, I ask Allah to forgive and mercy him.

# List of Symbols

The following list describes the symbols and abbreviations used in this thesis:

| | |
|---|---|
| $\alpha$ | Polarizability |
| $\beta$- | Hexagonal phase |
| $\langle \quad \rangle$ | Time average |
| $\boldsymbol{\chi}$ | Dipole matrix element |
| $\epsilon_o$ | Free space permittivity |
| $\gamma$ | Deactivation rate |
| $\gamma_{nr}$ | Photon nonradiative emission rate |
| $\gamma_r$ | Photon radiative emission rate |
| $\hbar$ | Modified Blank's constant |
| $\lambda$ | Wavelength |
| $\nabla$ | Gradient operator |
| $\omega_o$ | Emission angular frequency |
| $\overleftrightarrow{\mathbf{G}}$ | Dyadic Green function |

$\rho_o$ Free space local density of states

$\rho_p$ Local density of states

$\tau_r$ Radiative decay time (emission lifetime)

$\mathbf{E}$ Electric field vector

$\mathbf{F}_g$ Gradient force field vector

$\mathbf{F}_s$ Scattering force field vector

$\mathbf{n}_\chi$ Dipole unit vector

$\mathbf{p}$ Dipole moment

$\mathbf{r}_o$ Position vector

$\mathbf{u}_g$ Gradient force unit vector points towards the point of highest field intensity

$\mathbf{u}_s$ Scattering force unit vector in the direction of beam propagation

$\zeta$ Electron colision frequeny

$D$ Detector

$E(t)$ Time dependent electric field

$E_e$ Excited-state energy level

$E_g$ Ground-state energy level

$E_{exc}$ Excitation energy

$E_{gap}$ Band-gap energy

$F_p$ Purcell factor

$g^{(2)}(\tau)$ Second-order correlation function

$I(t)$ Time dependent light intensity

$I_o$ Light intensity (magnitude)

$n$ Refractive index

$n_m$ Medium's refractive index

$n_p$ Particle's relative index

$P_o$ Free space radiated power

$P_r$ Radiated power in a given environment

$Q$ Quality factor

$r$ Particle's radius

$t$ Time

$V$ Volume

FDTD Finite difference time domain

HBT Hanbury Brown and Twiss, interferometer

HOM Hong-Ou-Mandel, interferometer

LDOS Local density of states

NA Numerical aperture

NAFT Nanoaperture optical fiber tweezer

PML Perfectly matched layer

QD Quantum dot

SM Single molecule

SMF Single mode optical fiber

SNSPD Super-conductor nanowire single-photon detector

SPS Single-photon source

TFSF Total field scatter field

UCNP Upconverting nanoparticle

# Chapter 1

# Introduction

## 1.1 Research, brief introductory

Exciting a single luminescent nanoparticle and efficiently coupling its emission into a low-loss guiding channel are two significant challenges in developing single-photon sources (SPSs). A SPS is a quantum radiator that emits, perhaps on demand, a single photon at a time. Examples of nanoparticles that can be utilized to generate such non-classical photons include upconverting nanoparticles (UCNPs), quantum dots (QDs), and single-molecules (SMs), among others. These nanoparticles, when optically excited, radiate photons in all directions with different radiation rates depending on the type and composition of the radiating nanoparticle. Some nanoparticles, e.g. semiconductor quantum dots, have high radiative transition rates, $\gamma$ ($\sim 10^9 \mathrm{s}^{-1}$), compared to other nanoparticles which have low radiation rates, e.g. UCNPs ($\sim 10^3 \mathrm{s}^{-1}$). Nanofabricated plasmonic nanoaperture antennas, however, can be used to enhance the spontaneous decay rate and directivity of a nanoemitter by coupling its photon emission with the antenna subwavelength plasmonic mode [1]. Furthermore, coupling radiation from an emitting nanoparticle into an integrated low-loss channel, e.g. a standard telecommunication optical fiber waveguide, enhances collected signal

strength and, hence, photon detection. Luminescent nanoparticles, in addition to their potentially wide use in different application areas such as bioimaging and life sciences, can play an essential role in developing SPSs and the emerging technologies of quantum information processing, computation, and cryptography.

### 1.1.1 Single-photon source

A single-photon source is a light source that emits a single photon at a time. An example of such emission is the spontaneous radiation from a single atom. A single quantum-emitter, e.g. a single atom, can be represented by a simple two-energy-level system as shown in Fig. 1.1a. In this system, the *ground* state, $E_g$, and the *excited* state, $E_e$, energy levels are separated by an energy gap, $E_{gap} = E_e - E_g$. An electron at the $E_g$ level can be excited to jump into the $E_e$ level if it gains equivalent energy ($E_{exc} = E_{gap}$). This excited electron returns (by a deactivation or relaxation process) to the $E_g$ level and releases the excessive energy radiatively (spontaneously), represented by the blue solid arrow and the symbol $\gamma_r$ in Fig. 1.1a, or nonradiatively, represented by the blue dashed arrow and the symbol $\gamma_{nr}$. The total relaxation rate of the system is the sum of the two deactivation rates, i.e. $\gamma = \gamma_r + \gamma_{nr}$.

The photon emission rate, $\gamma_r$, and the nonradiative decay rate, $\gamma_{nr}$, differ from one photon emitter to another affected by the internal electronic distribution, the quantized energy levels of each, and by the physical and chemical properties of the emitter. However, the spontaneous emission rate is not an intrinsic property of the emitter, rather, it can be influenced by the electromagnetic environment of the emitter (e.g. a combination of a radiating photon source and an optical antenna).

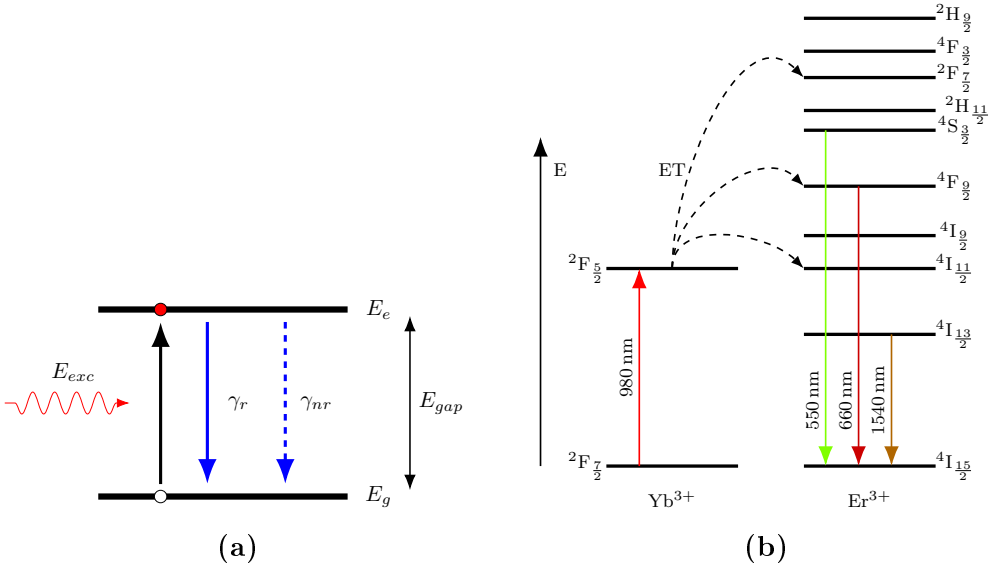


**Figure 1.1:** (a) Illustrative 2-level atomic energy system. $E_{exc}$ represents exciting photon energy; $E_g$, $E_e$, and $E_{gap}$ represent the ground, excited, and gap energy levels respectively. $\gamma_r$ and $\gamma_{nr}$ correspond to the radiative and nonradiative deactivation rates of the system. (b) Schematic energy level diagram (not precise) for $Yb^{3+}$-$Er^{3+}$ energy transfer under 980 nm excitation. Some of the upconversion ($\sim 550\,\&\,660$ nm) and downconversion ($\sim 1540$ nm) emissions are illustrated. The dashed arrows indicate energy transfer (ET) and the most left vertical arrow shows the direction of energy-level increase, modified and reprinted from Ref. [2].

### 1.1.2 Lanthanide-based UCNPs as 1550 nm wavelength photons source

Lanthanide-based upconverting nanoparticles are chemically adapted solid-state particles, with size $< 100$ nm, and composed of low phonon energy host materials, e.g. fluorides, chlorides, oxides, and bromides, doped with some predefined amounts of specific lanthanide ions. Examples of lanthanide ions used as dopants in the host material include erbium $Er^{3+}$, thulium $Tm^{3+}$, holmium $Ho^{3+}$, and ytterbium $Yb^{3+}$. Hexagonal phase ($\beta$-) sodium yttrium fluoride ($NaYF_4$) crystals have been co-doped with erbium ions ($Er^{3+}$) and ytterbium ions ($Yb^{3+}$) and introduced as some of the most efficient upconversion nanoparticles to date [3, 4]. The $Er^{3+}$ ions, called *activators*, emit light

when excited through an energy transfer process provided by the $Yb^{3+}$ ions, called *sensitizers*, within the host material. In contrast to quantum dots, these chemically adapted nanoparticles can produce photons in the visible band (e.g., $\sim 550\,\text{nm}$ and $\sim 660\,\text{nm}$) as well as in the near-infrared band (e.g., $\sim 1550\,\text{nm}$) when pumped at 980 nm wavelength. Furthermore, $\beta$-$NaYF_4$:$Yb^{3+}/Er^{3+}$ nanoparticles possess good chemical and photo stabilities, are nontoxic, are resistance to photobleaching, and can emit light at room temperature. The emission spectra for this type of UCNPs, measured with two different optical spectrometers, show several colors (see Fig. A.2 in Appendix A.1). UCNPs, however, have low upconversion efficiency where, based on integrating sphere measurement setups, the green-light quantum yield was found to be 0.005 % for core and 0.3 % for core-shell for 30 nm $\beta$-$NaYF_4$:20%$Yb^{3+}$/2%$Er^{3+}$ UCNPs, with incident power density equal to $150\,\text{W/cm}^2$ [5]; and 0.43 % for core 25 nm $\beta$-$NaYF_4$:17%$Yb^{3+}$/3%$Er^{3+}$ UCNPs, with incident power density equal to $410\,\text{W/cm}^2$ [6].

Energy transfer and up and downconversion of energy in a $Y^{3+}/\,Er^{3+}$ co-doped nanocrystal can be simplified, as shown in Fig. 1.1b. The $Y^{3+}$ ion absorbs some of the excitation energy and transfers it to the $Er^{3+}$ ion, which emits light in the visible ($\sim$ 550 & 660nm) and the near-infrared (1540 nm). Due to the screening effect in lanthanide ions, luminescence from $Er^{3+}$ under 980 nm is always in the same region and at the same color.

It is worth mentioning here at the beginning of this research that our use of the term UCNPs does not mean that the nanoparticles can only upconvert energy. It is just a common name (throughout this thesis) for the nanoparticles (or nanocrystals), e.g., $NaYF_4$ : $Yb^{3+}/Er^{3+}$, that are doped with lanthanide ions, and the process of energy conversion within these nanoparticles does not necessarily mean the upconversion of photon energy but also the downconversion as well.

### 1.1.3 Optical low-loss guiding channel

An optical fiber channel is more efficient than an open-air channel in guiding and coupling light emission from a nanoscale emitter to a photon detector. A 1550 nm optical fiber channel is characterized by: low propagation loss, typically 0.2 dB/km (0.0002dB/m) [7, 8]; extremely wide transmission bandwidth; and mechanical flexibility property. The low-loss property allows for long-distance guidance of the light signal, whereas the mechanical flexibility allows for easy coupling with the photodetector input terminal and improves photon detectability. The challenge in using the optical fiber to guide a wave is how to efficiently couple a light wave, e.g. emission from an excited nanoparticle, into the fiber channel. Although an optical fiber waveguide has a small numerical aperture, a typical acceptance angle is $\sim 8^{\circ}$ for standard 1.55 $\mu$m single-mode fiber (SMF); this challenge can be overcome by bringing the radiating nanoparticle close to the optical fiber facet and utilizing a directional antenna.

### 1.1.4 Plasmonic nanoantenna

A plasmonic nanoantenna is a metallic nanostructure that can confine near field electromagnetic energy in a subwavelength dielectric volume because of the field localization. An example of such metals is gold (Au), which is characterized by a dielectric constant of negative real part. Nanoantennas can be classified into two classes, the nanoparticles class and the nanoaperture class. Nanoparticle optical antennas can be made of nanowires, or plasmonic nanorods, e.g. a dipole nanoantenna made of gold nanorods. Nanoaperture optical antennas are made of subwavelength-size holes in plasmonic metal films, e.g. a double nanohole milled in an Au film. However, nanoantennas have been widely used in different application areas including Raman signal detection and optical trapping, and as coupling devices in optical circuits.

In accordance with the Purcell effect, the radiation rate of an optical emitter located in the gap of a nanoantenna can be enhanced by coupling its radiation with the gap field mode, by a factor that is inversely proportional to the field mode volume [9, 10]. Based on this principle, the emitter radiation rate can then be significantly modified by shrinking the field-mode volume, assuming that the nanoantenna is perfectly tuned to the particle's emission wavelength.

## 1.2 Research objectives and approach

The objective of this research is to propose an optical tweezer composed of an aperture type nanoantenna integrated with an optical fiber waveguide for enhancing optical trapping and developing single-photon sources. The concept is based on trapping a luminescent nanoparticle in a high field subwavelength volume and coupling the emission into a standard low-loss guiding channel, the optical fiber. Our approach to accomplish this involves several phases. First, fabrication of a nanostructured trap, which is a nanoaperture antenna in a thin planar gold film, using nanofabrication facilities represented in a focused ion beam (FIB) and a scanning electron microscope (SEM). Second, through a template stripping, the planar nanostructured aperture can then be transferred to the tip of a single-mode optical fiber, forming an integrated nanoaperture optical fiber tweezer. Subsequent phases include testing the ability of the integrated optical tweezer for trapping nanoparticles, coupling light into a SMF channel, and making photon detection measurements using a high sensitivity cooled superconducting nanowire single-photon detector (SNSPD).

Figure 1.2 schematically illustrates the various work steps that have been followed throughout this research. It is worth noting that throughout the three research phases, the finite difference time domain (FDTD) method has been used as the numerical technique for antenna design and near- and far-field calculations. However,

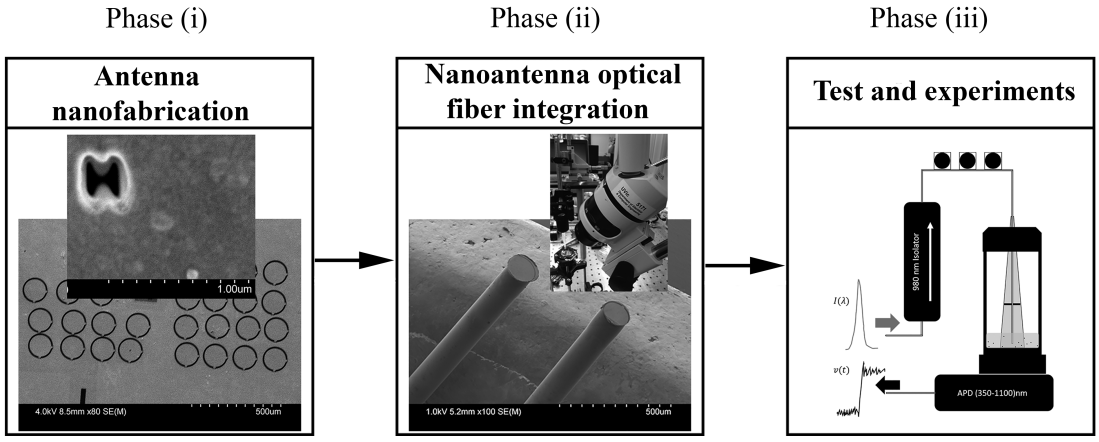


**Figure 1.2** – A schematic diagram shows the various phases of the research work. Phase (i): nanofabrication of the aperture nanoantennas using FIB and SEM. Phase (ii): template-stripping and integration of nanoantenna with the optical fiber. Phase (iii): optical trapping test and single-photon measurements.

the first phase is concerned with the nanofabrication and characterization of metallic nanoapertures using the FIB and SEM. In the second phase, we applied the approach of template stripping to transfer the nanofabricated metallic antenna onto the SMF tip. Details about the setup used in the transferring process will be demonstrated in Chapter 3. In the third phase, we tested the nanoantenna enhanced optical fiber tweezer for trapping nanoparticles (UCNPs) and measured the photon-emission statistics.

## 1.3 Thesis overview

Chapter 2 gives a general background review of the subject and discusses some relevant theoretical considerations. Chapter 3 discusses the fabrication of the nanoantenna and its integration with the single-mode optical fiber waveguide. Chapter 4 presents experimental results obtained by using the nanofabricated antenna enhanced optical tweezer. The results include trapping polystyrene nanospheres and UCNPs.

Chapter 5 demonstrates the enhancement of light coupling into the SMF channel through the use of a circular grating structure around the nanoantenna that we are going to place at the fiber tip. The measurement of light emitted by UCNPs using a single-photon detector will be discussed in Chapter 6. Eventually, a concluding summary for the research work will be given in Chapter 7.

# Chapter 2

# Background and Theory

## 2.1 Background

In classical information theory, digital processing, transmission, detection, computation, and storage of information are quantified using the two-state digital binary *bit*. According to quantum mechanics, a photon can have an infinite number of quantum states (quantum bits, qubits), which may result in developing ultra high-speed and ultra-secure quantum communication and computation systems [11–13]. These emerging SPS-based systems have raised interest in developing nanotechniques aiming to produce reliable and stable on-demand SPSs.

Nonclassical light sources, quantum sources, can be thought of as sources that produce on-demand single photons or sources that produce heralded single photons, also known as entangled photons [14]. Heralded single-photons are correlated photon pairs of nonclassical wavepackets where each wavepacket's peak time is known by observing the other wavepacket in the photon pair. An example of such a correlated photon-pairs source is the splitting of a single photon into two photons in a spontaneous parametric downconversion (SPDC) fluorescence [15]. In an SPDC process, an incident photon from a pump laser with angular frequency $\omega_i$ on a fluorescent

crystal simultaneously produces two photons with angular frequencies $\omega_1$ and $\omega_2$ in a nonlinear process under energy conservation, $\omega_i = \omega_1 + \omega_2$. Alternatively, on-demand single-photons, as briefly defined in Section 1.1.1, are nonclassical wavepackets whose peak time can be triggered on demand [16, 17], and the photons are emitted one at a time (antibunched wavepackets). On-demand single-photon sources can be single-molecules (or single atoms or ions), QDs, defect color centers (e.g. nitrogen vacancy centers in diamond lattice), UCNPs, and others.

### 2.1.1 Single atoms and molecules

The first experimental observation of the antibunching behavior of photons emitted from a beam of sodium atoms was obtained in 1977 [18], followed by extensive research efforts aiming to produce sources of antibunched photons with better photon number emission statistics. One approach was the trapping of a single quantum emitter in vacuum at low temperatures. For instance, an antibunched photon emission at $\sim 560\,\text{nm}$ from a laser-cooling trapped magnesium ion ($Mg^{2+}$) was observed. In this experiment, an ultrahigh-vacuum chamber ($\sim 10^{-11}\,\text{mb}$) and a laser-cooling mechanism were utilized to achieve the nonclassical light emission [19].

Single molecules also have been proposed for creating single-photon sources. An example of single molecules that fluoresce in the visible band is the terrylene molecules embedded in crystalline p-terphenyl at low concentration, $\sim 10^{-11}$ moles of terrylene in one mole of p-terphenyl [16, 20]. The terrylene emits at around 579 nm when it is excited by a 532 nm wavelength continuous-wave laser at room temperature. In the first study, both Poissonian and sub-Poissonian photon emission statistics were observed using a scanning confocal microscope setup. The Poissonian distribution of photon counting was obtained when the laser (a pulsed laser) beam is not focused on a single molecule, whereas the sub-Poissonian distribution of photon counting was

obtained when the laser beam is positioned on a single molecule.

### 2.1.2 Quantum dots and vacancy centers

Semiconductor QDs have also been used for realizing SPSs. Due to the quantum size effect, QDs have an attractive characteristic that allows their light emission to be controlled by changing their size and shape [21–24]. There have been studies demonstrating single-photon emission using QDs embedded in photonic structures, e.g. photonic crystal cavities [25, 26], photonic nanowires [27–29], and pillar cavities [30,31]. However, single-photon emissions of rate $\sim 5\times10^{9}\,\mathrm{s}^{-1}$ and $\sim 4.4\times10^{-4}$ degree of antibunching have been achieved at $\sim$ 1550 nm by embedding a self-assembled indium arsenide (InAs) QD in an indium phosphide (InP) photonic cavities [32,33].

Although QDs have a fast single-photons radiation rate, they suffer from photo-toinstability. Also, the single-photon emission from a QD is affected by the QD size and temperature and requires a cryostat environment for a stable generation.

Diamond also has been widely used as a host matrix for single atoms (vacancy-centers), e.g. nitrogen (N), nickel (Ni), silicon (Si), and others. Diamond is characterized by a wide spectrum transparency and high refractive index [34]. The nitrogen vacancy (NV) center in diamond has emerged as an attractive SPS in the visible range. Examples of antibunched photon emission, and coupled into a SMF, at $\sim$ 660 nm from NV-centers in diamond were demonstrated in [35,36] with an antibunching degree of $< 0.2$.

It is worth noting that the sources mentioned above of single-photons have emission spectra which depend on the electronic transitions in the excited atoms. For example, a photon emission from the nitrogen atom in a diamond matrix under 532 nm excitation would be at $\sim$ 660 nm wavelength [36]. Also, most of the semiconductor QDs, influenced by their size and shape, radiate in the visible and near infrared (NIR)

range of the optical spectrum when excited by ultra violet or visible photons [21]. However, some luminescent materials are not reliable and have photoinstability issues. For example, QDs suffer from the blinking phenomenon, an undesirable effect that causes random fluctuations in the emitted photons, which adversely affect their potential use as SPSs [37, 38].

### 2.1.3 Nanaocrystals

Single lanthanide ions, in crystal hosts, have also been demonstrated as potential sources of single photons. For example, optical detection with nonclassical photon statistics has been demonstrated using praseodymium ions ($Pr^{3+}$) doped in yttrium garnet crystals (YAG) [39], and erbium ions ($Er^{3+}$) doped in yttrium orthosilicate substrate YSO [40]. Electron transition in single erbium ions implanted into a silicon channel of a single-electron transistor has also been exploited to measure photo-induced changes in current flow [41]. It is worth noting here that in the examples given, there was not a single and isolated lanthanide ion; instead, there were a bunch of ions in a host material probably with low concentration.

On the other hand, $Er^{3+}$ and $Yb^{3+}$ doped nanocrystals, particularly the $\beta$-$NaYF_4$ : $20\%Yb^{3+}/2\%Er^{3+}$ nanocrystals, are characterized by their broad emission spectrum and photostability. For instance, multiple and easy to separate emission peaks in the visible and in the NIR spectrum ranges can be obtained from these UCNPs when excited by a 980 nm cw laser (see Fig. A.2 in Appendix A.1). Regarding photostability of these UCNPs, a constant emission intensity which remains stable for a long time (e.g. for 1 hour of continuous laser illumination) without any blinking has been demonstrated [42]. To our knowledge, these nanoparticles have not yet been demonstrated as a potential quantum photon emitter. In addition to the low upconversion efficiency of such UCNPs (see Section 1.1.2), the reasons for them not being used

as SPSs could be any or all of the following: the large number of photon emitters contained in each single nanoparticle, the difficulties in isolating a single UCNP, and the fact that lanthanide ions have long emission lifetime transients. However, according to a recent theoretical study [43], the number of $Er^{3+}$ ions in a single $\beta$-$NaYF_4$ : $20\%Yb^{3+}/2\%Er^{3+}$ nanoparticle (size range in the study between 10 nm and 100 nm) is relatively high (see Fig. A.4 in Appendix A.1).

Last but not least, the $\beta$-$NaYF_4$:$Yb^{3+}/Er^{3+}$ UCNPs have been demonstrated as the most efficient upconversion luminescent material [44, 45]. Most of the previous work connected to UCNPs, particularly the sodium yttrium fluoride ($NaYF_4$) host crystals doped with lanthanide ions, was focused on improving emission color tunability and enhancing the upconversion luminescence of the UCNPS. These nanoparticles have emission spectra extending over the visible and the near-infrared range, e.g. 545 nm, 660 nm, and 1536 nm. Particles sizes have been demonstrated from 5 nm up to 200 nm [45, 46].

### 2.1.4 Photon emission enhancement using plasmonic structures

Single-photon emission from single molecules, vacancy-centers, and QDs, has also been demonstrated through the use of plasmonic nanostructures, optical fibers, and a combination of both. Plasmonic nanocavities have the ability to localize and support high field intensity modes in a subwavelength volume where a single emitter can be positioned (with difficulty) and excited to emit photons. Plasmonic structures also have the potential to enhance the intensity and emission rate of radiation. Development in nanotechnology has made the fabrication of complex subwavelength nanostructures in metals easy. Unlike semiconductor-based microcavities, the small size of nanocavities is a great advantage because of the influence of the cavity mode

volume on the emission rate of a light source. On the other hand, the low-loss waveguiding property of optical fibers has also been exploited to collect and guide light emission from radiating sources.

A considerable amount of literature has been published in the field of photon emission rate enhancement. For example, an increase in the radiation rate by a factor of $\sim 1000$ has been demonstrated using a gap plasmon nanocavity composed of a silver nanowire on a silver substrate separated by a $\sim 5\,\text{nm}$ dielectric bilayer of aluminum dioxide ($Al_2O_3$) and the fluorescent dye molecule tris-(8-hydroxyquinoline) aluminum ($Alq_3$), which has multiple emission peaks in the visible band [47]. A similar study [48] uses a $\sim 80\,\text{nm}$ silver nanocube positioned over a metal film with an $8\,\text{nm}$ dielectric gap that contains fluorescent Ru dye (ruthenium metal complex), which has an intrinsic lifetime of $\sim 600\,\text{ns}$ measured on a glass substrate. The excitation wavelength is $535\,\text{nm}$, and the emission is at $\sim 620\,\text{nm}$. Radiated light was collected using an objective lens with a numerical aperture $\text{NA} = 0.9$. The enhancement in the radiative rate obtained in this study was in the range of $\sim 850$ times.

Subwavelength metallic nanoapertures of various shapes have also been demonstrated to be effective tools for optical trapping and for enhancement of emission intensity, directivity, and decay rate of fluorescent molecules and nanoparticles [49–55]. In these studies, appropriate objective lenses have been used, which play a significant role in the trapping process, to localize a high electric field intensity and to collect radiation from the nanoaperture. For instance, in [54, 55], high numerical aperture objective lenses, $\text{NA} > 1$, have been used in setups equipped with a 3D piezoelectric-stage for precise alignment of the nanostructure with the laser beam.

### 2.1.5 Optical fiber probes

Many attempts at integrating metal nanoapertures with optical fibers have been successfully realized, allowing for the elimination of cumbersome microscopes, sample holders, piezoelectric aligners, etc. Nonfluorescent 20 nm and 40 nm dielectric nanospheres have been trapped using a double nanohole milled in a gold film, coating the tip of an SMF, has been demonstrated [56]. In this case, the nanoaperture is directly excited by the laser beam propagating within the fiber channel. Trapping was observed by monitoring transmission through the nanoaperture. In this research, a cleaved end SMF is first coated with $\sim 100$ nm gold layer, and then a double nanohole is milled on its top using the FIB. This study shows not only easy trapping of nanoparticles, but also that nanoaperture-fiber integration can be utilized as a fluorescence sensor of radiation nanoparticles.

Direct coupling of light emission from luminescent nanoparticles into optical fiber waveguides is an increasingly important area of research in developing single-photon sources. An alignment-free single-photon emission coupling from a nitrogen vacancy (NV) center in diamond into a tapered SMF has been demonstrated [36]. In this approach, Van Der Waals forces were exploited to stick a 200 nm cross-section tapered single-mode diamond micro-waveguide onto a tapered section of a $\sim 500$ nm cross-section single-mode optical fiber. The NV was pumped by a 532 nm laser, and an antibunched photon emission, at $\sim 660$ nm wavelength, was collected at both ends of the SMF. The antibunched generated photons showed a $\sim 0.15$ normalized second-order correlation function at zero delay time on a Hanbury-Brown and Twiss setup where the SMF was used as a wave-splitter.

## 2.2 Theory

### 2.2.1 Spontaneous decay rate

The radiative decay rate (or the lifetime) of a nanoemitter photonic spontaneous emission can be affected by the surrounding environment. It has been demonstrated that an emitter in front of an electromagnetic reflector [57], or within a cavity that is resonant to the emission wavelength [58] will experience some degree of influence on its spontaneous emission rate as well as on its angular luminescence distribution. According to quantum electrodynamics theory, the spontaneous decay rate of a two-level quantum system of a nanoemitter is given by

$$\gamma = \frac{\pi\,\omega_o}{3\,\epsilon_o\,\hbar}\,|\boldsymbol{\chi}|^2\,\rho(\mathbf{r}_o,\omega_o) \tag{2.1}$$

where $\rho(\mathbf{r}_o,\omega_o)$ is the local density of states of the system and is defined as follows [59, 60]:

$$\rho(\mathbf{r}_o,\omega_o) = \begin{cases} \dfrac{{\omega_o}^2}{\pi^2 c^3} & \text{homogeneous free space,} \\ \\ \dfrac{6\omega_o}{\pi c^2}\Big[\mathbf{n}_\chi \cdot Im\big\{\overleftrightarrow{\mathbf{G}}(\mathbf{r}_o,\mathbf{r}_o,\omega_o)\big\}\cdot\mathbf{n}_\chi\Big] & \text{nonhomogeneous space.} \end{cases} \tag{2.2}$$

In Eqs.(2.1) and (2.2), $\omega_o$ is the emission, or the atomic transition, angular frequency; $\boldsymbol{\chi}$ is the transition dipole matrix element, or the dipole moment of the atomic system; $\mathbf{r}_o$ is the location of the dipole moment; $\epsilon_o$ is the free space permittivity; $\hbar\,\omega_o$ is the difference in energy between the initial and final electronic states; $c$ is the speed of light in free space; $\overleftrightarrow{\mathbf{G}}(\mathbf{r}_o,\mathbf{r}_o,\omega_o)$ is the dyadic Green function evaluated at the position of the radiating dipole; and $\mathbf{n}_\chi$ is the unit vector in the direction of the dipole moment.

### 2.2.2 Purcell effect

Purcell enhancement is the increase in the spontaneous decay rate of an emitter that occurs when the emitter is placed close to an object, e.g., a nanoantenna. A Purcell factor can be defined as the ratio of the decay rate of the emitter in the vicinity of the object to its decay rate when placed in free space, and is given by the formula [60]

$$F_p = \frac{\gamma}{\gamma_o} \,. \tag{2.3}$$

Based on the two-level system of Fig. 1.1, the photon emission decay time, $\tau$, can be expressed in terms of the radiative decay rate as

$$\tau = \frac{1}{\gamma_r} \,, \tag{2.4}$$

which can be obtained from a time-resolved photon emission measurement by observing the change in the photo detected radiation intensity as a function of time [61]. This change in the photon intensity (photon-count-rate) is usually monoexponential and represents the repetition speed of electromagnetic energy radiation from the quantum emitter and is a key feature in developing single-photon sources. It is obvious from Eq.(2.1) that increasing the LDOS at the nanoemitter position results in shortening the lifetime. It has also been demonstrated that the ratio of Eq.(2.3) is mathematically equivalent to the ratio of a classical dipole radiated power (rate of energy dissipation) in a given environment to its free space radiated power, as follows [60]:

$$F_p = \frac{\gamma}{\gamma_o} \ = \frac{P}{P_o}. \tag{2.5}$$

For optical cavities and field confining structures that are perfectly matched with the emitter, the Purcell factor can also be expressed in terms of the quality factor, $Q$, and the mode volume, $V$, as follows [9, 10, 62, 63]:

$$F_p = \frac{3}{4\pi^2} Q \frac{(\lambda/n)^3}{V}, \tag{2.6}$$

where $\lambda/n$ is the resonance emission wavelength in the medium surrounding the emitter, and $n$ is the medium index of refraction. Equation (2.6) shows that the Purcell factor can be enhanced by either a resonant cavity that has a high $Q$-factor, a small mode volume, or both.

Based on the Purcell effect, therefore, the emission lifetime of an emitter can be modified by changing its surrounding environment. For instance, Fig. 2.1 shows

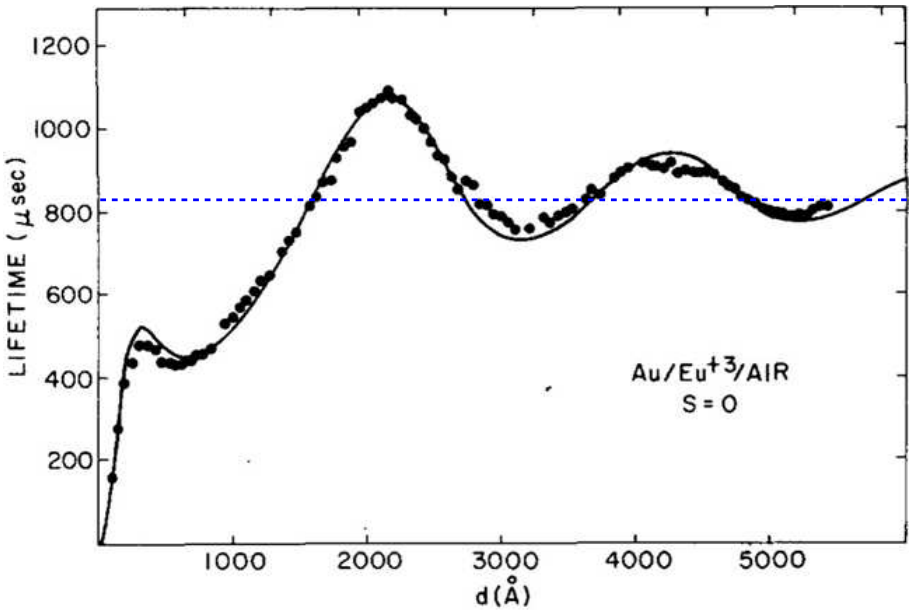


**Figure 2.1** – Emission lifetime of europium ion as a function of distance, d, in front of a gold mirror, from Reference [64]. We approximately added the blue dashed line to indicate the intrinsic lifetime of the $Eu^{3+}$ ion at the 612 nm emission wavelength.

lifetime experimental data results, taken from Reference [64], for a europium ion ($Eu^{3+}$) complex that radiates at 612nm as a function of distance d from a planar gold mirror. The figure shows a noticeable increase in the radiation rate as the emitter comes closer to the mirror ($d < 100\,\text{nm}$), and it increases faster to higher values when it is only a few nanometers from the mirror.

### 2.2.3 Photon antibunching

Photons emitted from a light source are referred to as *bunched* if they propagate more likely close to each other in time than far apart from each other. Conversely, photons are classified as *antibunched* if they are more likely to be produced far apart in time than close to each other.

A single-photon source is a nonclassical-light quantum emitter of antibunched photons with a second-order correlation function, $g^{(2)}(\tau)$, which satisfies the inequality $1 > g^{(2)}(0) \geqslant 0$, where $\tau$ is the photon arrival delay time as depicted in the two-photodetector model shown in Fig. 2.2 [65]. The arrangement of beam splitter, photon detectors, and timing electronics in Fig. 2.2 is usually referred to as a Hanbury Brown-Twiss (HBT) interferometer [66]. Based on this arrangement, the intensity correlation $g^{(2)}(0)$ of the incident light from the source can be measured. It is very obvious from Fig. 2.2 that, for an ideal single-photon source, there is no chance for both the detectors $D_1$ and $D_2$ to observe photon incidence simultaneously; consequently, $g^2(0) = 0$. The interferometer works by recording the relative delay time between the detection of a photon at each of the two photodetectors. For example, detector $D_1$ starts measuring the number of photons in the input intensity field $I(t)$ at time $t$ and stops when detector $D_2$ registers a photon detection from the input intensity field $I(t + \tau)$, after a time delay $\tau$. The second-order correlation function of the two

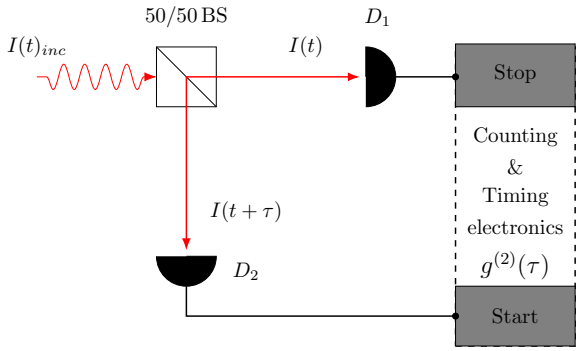


**Figure 2.2:** Hanbury Brown-Twiss interferometer. The incident light (photons) is divided by the beam-splitter, BS, and the outputs are detected by two photodetector units, $D_1$ and $D_2$, which are connected to a timing and coincidence electronics.

optical light intensities can be expressed as follows:

$$g^{(2)}(\tau) = \frac{\langle I(t)I(t+\tau)\rangle}{\langle I(t)\rangle\langle I(t+\tau)\rangle}, \tag{2.7}$$

where $I(t)$ and $I(t+\tau)$ are the intensities at times $t$ and $t+\tau$; $\tau$ is the delay time; and the angle brackets, $\langle\ \rangle$, denote time averaging [14, 65]. A normalized intensity correlation can therefore be obtained by building a histogram of the start-stop delay times between the photon numbers recorded through detectors $D_1$ and $D_2$.

### 2.2.4 Photon indistinguishability

Single-photons can take different quantum states, and therefore, in some applications, for instance, quantum communications and information processing require indistinguishability in the generated photons. Sometimes we need to use multiple single-photon sources in the SP-based quantum system, e.g., an optical quantum transceiver that needs identical sources. In this case, the two single-photon sources are required to be indistinguishable. However, the indistinguishability of single-photons means that the photons have to be identical (have the same quantum state, e.g., same po-

larization and momentum). The indistinguishability of two photons can be measured using HOM interference (Hong-Ou-Mandel interferometer, see Fig. 2.3). In the figure, the two input photons, $\rho_a \,\&\, \rho_b$, will interfere if they both exit the same path, otherwise they will coincide with each other with some probability $\mathrm{P}(\tau_{\mathrm{ab}})$, where $\tau_{ab}$ is the arrival delay time at the beam splitter between the two photons. A closer value of P to zero indicates better indistinguishability between the two photons [67, 68].

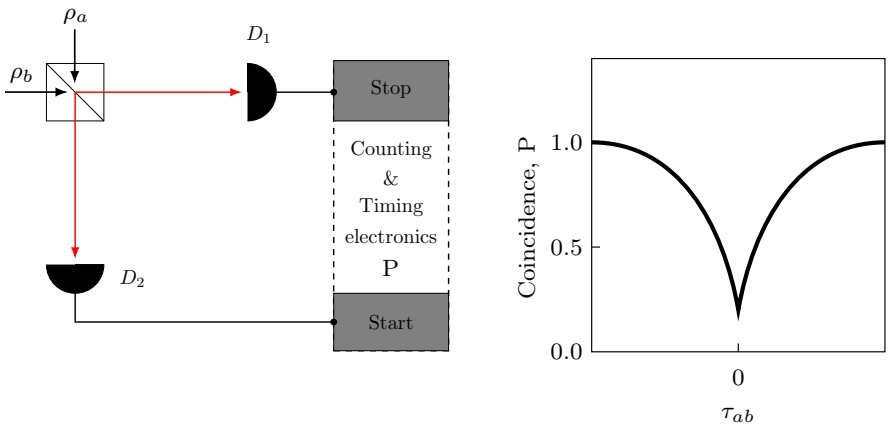


**Figure 2.3:** HOM interferometer (left). The coincidence of the two photons $\rho_a \,\&\, \rho_b$ schematically illustrated in the right sketch. $\tau_{ab}$ is the arrival delay time at the beam splitter.

# Chapter 3

# Integration of nanoaperture antenna with optical fiber

## 3.1 Introduction

Metallic optical nanoantennas, of varying geometrical structures, have been widely used for a variety of purposes. These antennas are characterized by their small size (a fraction of the optical wavelength) and by their ability to localize a high field intensity in a nanoscale volume. Examples of such plasmonic nanoantennas include: the double nanohole, used in optical trapping [54, 56]; the single dipole with circular reflector, used for Raman signals spectroscopy [69, 70]; the circular-hole with plasmonic corrugations, used for fluorescence emission directivity enhancement [52]; the bowtie structure, used for enhancing photon emission from semiconductor materials [50] and for enhancing fluorescence of light emitting single molecules [71]; and so on.

A common feature of most optical nanoantennas is the subwavelength plasmonic gap where electromagnetic field energy can be confined in a nanoscale volume. This is very important, as it is a key feature in utilizing an optical nanoantenna to trap

nanoparticles and to enhance emitter radiation and directivity and as an imaging and spectroscopic scanning probe, etc.

As nanoscience and nanotechnology developed, the fabrication of small-scale antenna structures of different geometries and sizes has become possible. The FIB [72] and SEM [73] are efficient tools that have been widely utilized to directly structure and characterize nanoscale patterns. All nanoantenna structures used in this work have been fabricated and characterized using these nanotechnological facilities available at the University of Victoria.

Using nanoantennas, weak emission from a fluorescent nanoparticle and radiation directivity can both be competently enhanced. Since most photodetectors are fiber-coupled devices, the integration of a radiative source with a low-loss optical fiber channel is a challenging task but one that has many benefits. For example, it eliminates the need for cumbersome optical devices. Also, with a proper antenna structure, signal strength can be enhanced. Therefore, the main focus of our research in developing SPSs is to integrate a nanoantenna structure with a low-loss optical fiber channel, the optical tweezer.

In this chapter, the integration of a bowtie metallic nanoantenna structure with an SMF will be demonstrated.

## 3.2 Nanoantenna fabrication and numerical simulation

In this section, we show the integration steps of a nanofabricated metallic nanoaperture antenna with an SMF channel. The integration is performed using an optically curable epoxy material, Norland Optical Adhesive 61 (NOA 61). More data on NOA 61 regarding its refractive index and optical transmission is provided in Appendix B.

The integration parts can be better visualized by referring to the schematic diagram shown in Fig. 3.1. We used gold, Au, as the metal base-structure to produce the metallic nanoaperture antenna. Gold is a plasmonic material unaffected by air and by most chemical solutions. For the optical channel, we used the standard 1550 nm SMF-28 from Corning.

### 3.2.1 Fabrication

After measuring the emission spectrum of the UCNPs of interest (see Fig. A.2 in Appendix A.1 for the setup used in the measurement), we used the FIB for milling the bowtie-shaped aperture nanoantenna shown in Fig. 3.1. The FIB is an ionic microscope system that generates a powerful beam of high mass gallium ions, $Ga^{+3}$, which can be focused through a set of electrostatic lenses and deflectors [72]. Although using the FIB allows nanofabrication of complex structures in the nanoscale, nanohole milling in metal films with such focused beams usually leaves some defects in the milled hole edges and walls, e.g. rounded edges and nonuniform gaps (see e.g. [74,75]). Producing holes with sharp edges and right corners becomes extremely difficult as the hole size decreases to $< 100$ nm. However, in the FDTD simulations, we have partially corrected these defects by approximating a tapered wall gap, as can be seen in Figures B.2 and B.3 in Appendix B.

Since we are integrating the nanoantenna with a standard optical fiber of a circular cross-section, the nanohole is best milled at the center of a circular Au film of diameter 125 $\mu$m and thickness 100 nm with a high accuracy. Figure 3.2 shows an SEM sample images of a 90 degree cleaved end SMF and FIB milled Au circular film and a nanoaperture bowtie antenna. Typical nanofabrication dimensions are given in the figure caption. The ring was fabricated at 1 k $\times$ magnification and the aperture at 35 k $\times$. The gold appendages at the edge of the circular gold film in the image of

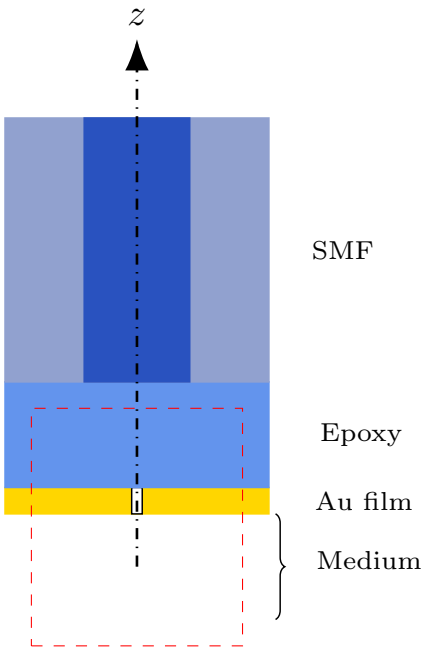


**(a)** A schematic diagram of the nanoantenna-SMF integration.

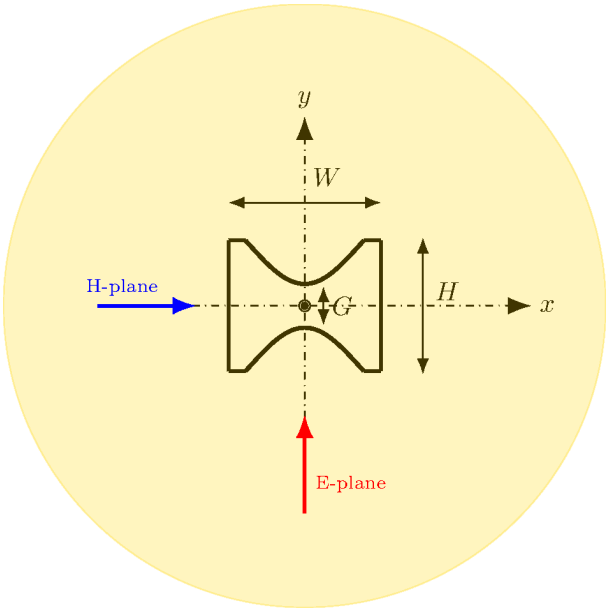


**(b)** Aperture bottom view

**Figure 3.1** – Schematic diagrams. (a) The integrated nanoaperture antenna with SMF. (b) An enlarged bottom view of the nanoaperture antenna centered in the Au film. Typically, dimensions $W$, $H$, and $G$ are $\sim$ 275, 175, and 40 nm. A schematic diagram for the top side of the aperture can be seen in Appendix B.

Fig. 3.2b are for discharging the tip when later imaging in the SEM. They also serve as alignment markers to show the orientation of the nanoaperture.

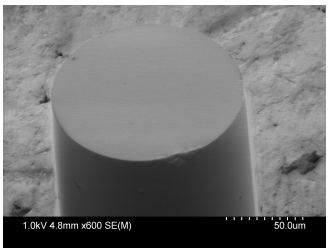


**(a)** SEM image of a 125 $\mu$m diameter jacket stripped SMF.

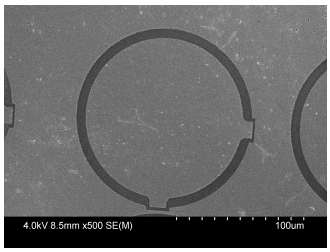


**(b)** SEM image of a 125 $\mu$m Au gold film milled using FIB at 1 k $\times$.

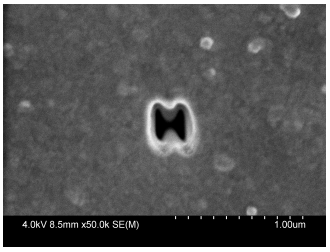


**(c)** SEM image of a nanoaperture antenna milled using FIB at 35 k $\times$.

**Figure 3.2** – SEM images. (a) A cleaved end SMF cut at 90° and prepared for template stripping. (b) A 100 nm Au film after being milled using the FIB. The ring inner diameter is 125 $\mu$m and the outer diameter is 140 $\mu$m. (c) SEM image for the plasmonic aperture. The average aperture gap is $\sim$ 60 nm between the cusps.

The fabrication of the nanoaperture-optical-fiber-tweezer, NAFT, has been accomplished through several steps, which are described in the following subsections.

#### 3.2.1.1 Creating a 100 nm thick gold film

We evaporate gold onto a glass substrate of $\sim$ 1 mm thick and $\sim$ 1 cm$^2$ in area to form a 100 nm thick Au film. Figure 3.3 is a photograph of some of these films. The gold was evaporated onto small-size precut glass substrates to avoid further cutting after evaporation. This approach keeps the film surface clean for FIB milling and

later SEM imaging. It is worth mentioning that the gold was evaporated directly on the glass surface without any adhesion material to facilitate the transferring of the gold onto the fiber tip in later steps.

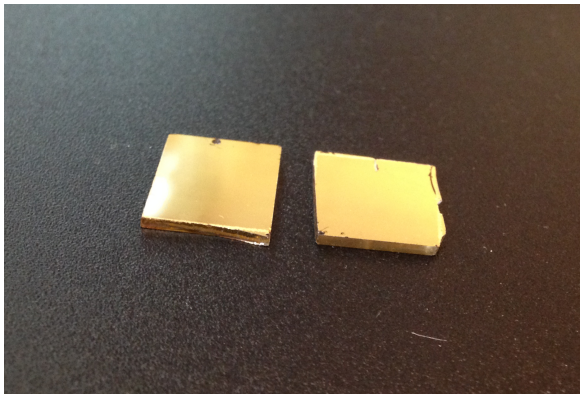

**Figure 3.3** – A photograph of a 100 nm thick gold films evaporated on $\sim 1$ mm glass substrates. The size of each sample is $\sim 1\,\text{cm} \times 1\,\text{cm}$

#### 3.2.1.2 FIB milling

In this step, the Hitachi FB-2100 focused ion beam system is used to mill the pre-defined pattern structures. The patterns are basically bitmap images of the bowtie nanoaperture and the circular gold film. Figure 3.4 shows sample shapes of such patterns. These patterns can be made using any graphics software that supports BMP file format, e.g., Adobe Photoshop. Also, the patterns have to be created within an area of $2000 \times 2000$ pixels taking into consideration the magnification at which the pattern needs to be cut when using the FIB.

The FIB-2100 machine has different $Ga^{+3}$ ions flux density cutting beams, with 40 kV acceleration voltage. High flux density beams have short milling time and are usually used to cut large area patterns at low magnification, e.g., the ring pattern shown in Fig. 3.4a. Lower flux density beams, on the other hand, can be deliberately chosen to fine cut small area features, e.g., the bowtie pattern shown in Fig. 3.4b. Typical examples of relatively high and low flux density beams provided by the FB-

2100 system are the 40.1.300 and 40.1.15 beams where; the numbers xx.y.zzz denote to the beam accelerating voltage, beam convergence mode, and the beam selected-area aperture (Hitachi FB-2100 data manual).

Due to technical problems, e.g. heat, the difficulty of accurately aligning the milling beams, and astigmatism, it is extremely difficult to cut a nanohole that exactly matches its predesigned, or FDTD defined, shape. Consequently, the pattern illustrated in Fig. 3.4b, for instance, is not the optimal shape, rather, it is a shape designed to reduce the effects of heat, inaccuracy in beam alignment, and beam astigmatism. The black colour in the bitmap patterns in Fig. 3.4 represents the area that will be scanned and milled by the FIB. The effect of changing the FIB milling parameters, e.g. scanning time, direction and dwell time, can be exploited to determine the final shape of the structure.

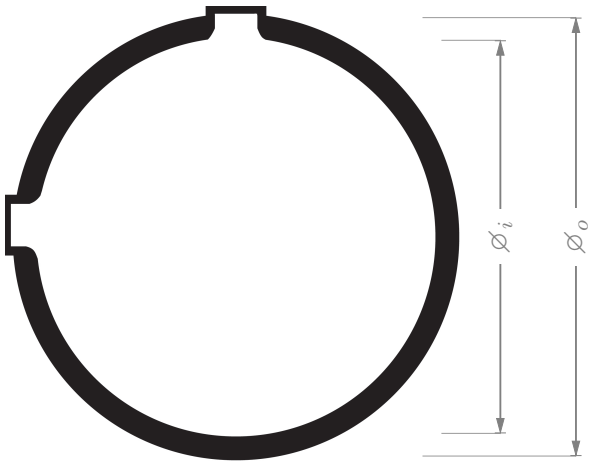


**(a)** A bitmap image of the ring pattern used to FIB the circular Au film. Typical numerical values for $\varnothing_i$ and $\varnothing_o$ are 125 $\mu$m and 145 $\mu$m.

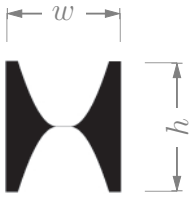


**(b)** A bitmap image of the pattern used to produce the bowtie antenna aperture with the FIB. Typical numerical values of $w$ and $h$ are 265 nm and 165 nm.

**Figure 3.4** – Sample bitmap patterns used to produce the FIB milled structures shown in Figures 3.2b and 3.2c.

The goal of using the FIB is to nanofabricate, in a planar approach, multiple circular gold films with a nanoaperture at the center of each film. This approach

is fast and scalable and requires a single milling beam alignment. Previous efforts at integrating metal nanoapertures with fibers have been operated on the fiber tip directly, which is complicated and not scalable. However, to adapt the approach to large-scale production, the challenge is to perform a standard planar fabrication along with fiber tips. Figure B.1 in Appendix B shows an example of a planar nanofabricated structure that we used for template stripping of gold onto the fiber tips.

#### 3.2.1.3 Nanoaperture-SMF integration

Several approaches to transferring metal nanostructures onto different substrates have been investigated. These include template-stripping of arrays of gold nanotip wedges evaporated on a sharply etched silicon substrate onto a glass surface using epoxy [76] and template-stripping of collections of different nanostructures (like holes, wires, pyramids) from a planar silicon substrate onto a stretchable polydimethylsiloxane [77]. The template-stripping approach has also been used to create a high quality and

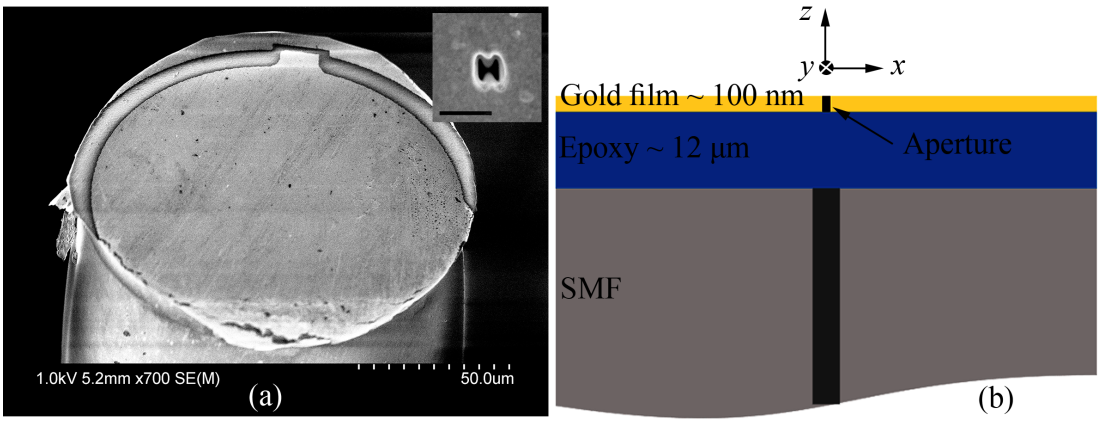


**Figure 3.5** – (a) Scanning electron microscope (SEM) image of the integrated NAFT. The inset shows the plasmonic aperture milled at the center of the NAFT; the scale-bar is 0.5 $\mu$m. (b) Schematic diagram of the integrated NAFT (not to scale). The epoxy used is the Norland optical adhesive 61 (NOA 61), a photopolymer liquid that cures when exposed to ultraviolet light.

ultra sharp near-field imaging probe (with a sharp gold apex on a tungsten wire) [78]. Multiple template double nanoholes on silicon substrate have also been template-stripped onto a glass substrate using epoxy for optical trapping [79].

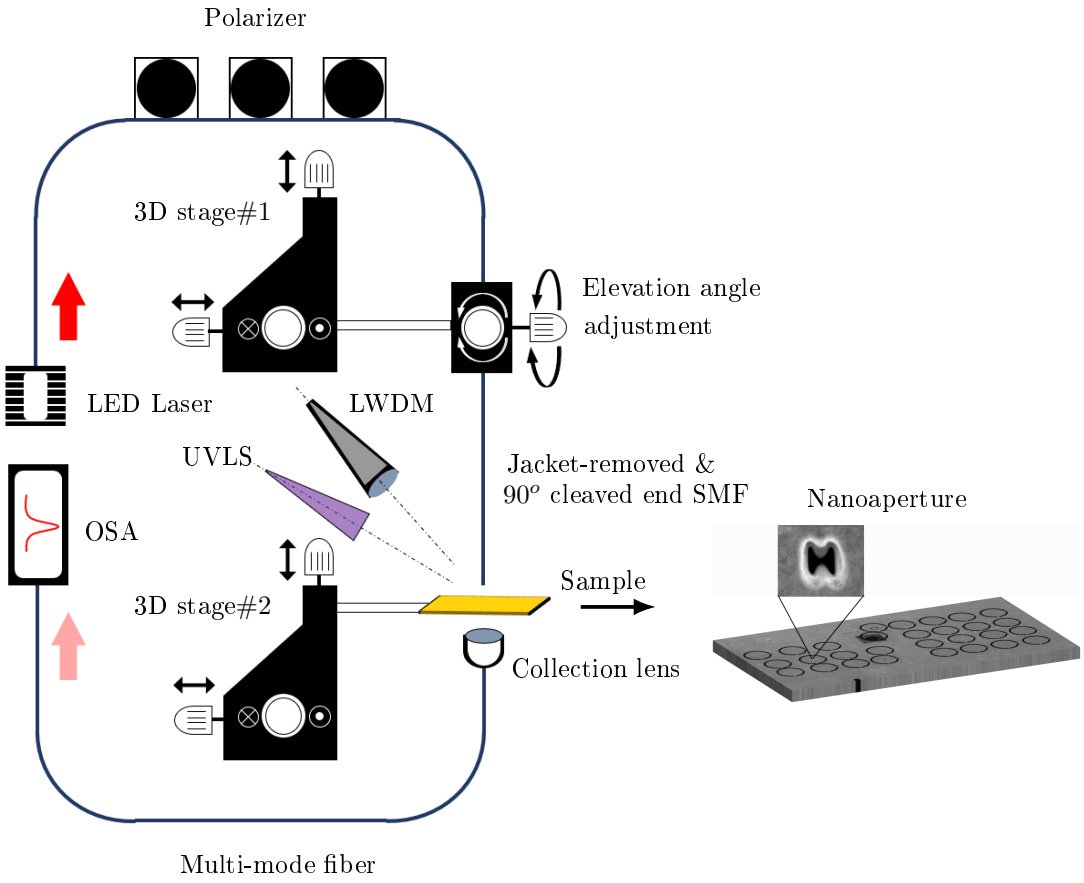


**(a)** Template-stripping setup schematics. **(b)** FIB-milled gold sample.

**Figure 3.6** – Schematic diagram of the setup used for template-stripping of the gold FIB milled circular gold film on an SMF tips (a), and (b) shows a FIB milled gold sample with multiple circular gold films. LED is an abreviation for light emitting diode, OSA is an optical spectrometer analyzer, UVLS is an ultra-violet light source, and LWDM is a long working distance microscope.

Here, we used a carefully aligned stripping approach to get the nanoaperture in the metal film aligned with the core of a standard cleaved-end SMF. This approach is a standard planar nanofabrication technique that allows for broad adoption. Figure 3.5 shows an SEM image and a schematic for the integrated NAFT, where the FIB

structured gold film is directly transferred to the SMF tip in a template-stripping process. Figure 3.6 shows a schematic diagram for the setup used in the process.

To integrate the nanoaperture with the SMF, we started by horizontally placing the FIB milled gold sample on the lower 3D-stage shown in Fig. 3.6. The upper 3D-stage was used to hold the SMF. The gold sample has multiple nanoapertures; each was centered in a circularly milled gold sub-film. Figure B.5 in Appendix B.4 shows more detail regarding the transferring process.

### 3.2.2 FDTD simulation

The FDTD method is one of the most widely used numerical techniques to solve electromagnetic problems involving complicated scatterers and antenna structures. The method is based on discretizing Maxwell's equations in space and time with central difference approximations.

In this research, the FDTD software release 2017b, version 8.18.1365 from Lumerical Solutions Inc., is used to simulate the near and far-fields for the nanoaperture optical fiber tweezer, NAFT. As previously mentioned, one of the purposes of the antenna is to achieve a gradient field force suitable for trapping nanoparticles in the aperture's gap. On the other hand, particle emission enhancement and coupling into the fiber channel are essential too. Based on these requirements, in the FDTD simulation, we used a 980 nm plane wave source to simulate a 3D region composed of the three layers indicated by the dashed red rectangle in Fig. 3.1a. We used the 980 nm wavelength because the experimental research phase on UCNPs requires a laser excitation at this wavelength to excite the nanoparticles to emit light at the peak wavelength of $\sim$ 1540 nm. To simulate the emission from a nanoparticle, we used a dipole source radiating at 1540 nm wavelength and located at the center of the aperture's bottom. However, in both simulations, the FDTD simulation region was

bounded by a PML and the whole computation space was nonuniformly divided into 3D differential cells.

#### 3.2.2.1 980 nm plane wave source FDTD simulation

In this part of the FDTD simulation, the total-field scattered-field (TFSF) source is used to estimate the electric field spatial intensity distribution around the nanoaperture antenna. A TFSF source is a plane wave source with numerical boundaries that enclose an entire field region, i.e. the incident and scattered fields. The rest of the computational space outside of the enclosed region contains only the scattered field. Using this kind of FDTD numerical electromagnetic source allows the nanostructure scattered field to be isolated from the source incident wave field. In this simulation, we used a normally incident 980 nm plane wave with an incident power density of $\sim 0.5\,\mu\mathrm{mW/m^2}$.

Figure 3.7 shows the electric field intensity distribution over three orthogonal planes within the FDTD simulation region caused by a y-polarized plane wave source excitation of the nanoaperture antenna in the gold film. Figures 3.7a and 3.7b show the electric field intensity $|\mathbf{E}|^2$ in the $xy$-plane exactly at the water-gold-film interface (we used water here as a default suspensor for nanoparticles). The hot spot at the center of image (a) shows the high confinement of the electric field within the aperture gap. Image (b) gives a clearer picture of the localized electric field within the nanoantenna aperture. Details about the FDTD simulation region, data recording monitors, the orientation of the excitation source, and the computation space structure are given in Fig. B.4 in Appendix B.3.

The purpose of integrating the plasmonic nanoaperture with the optical fiber waveguide is to use it for trapping nanoparticles suspended in a liquid chemical, e.g. water, ethanol, hexane, among other chemicals; and enhance and inject radiation

into the optical channel. Figures 3.7c, 3.7d, 3.7e, and 3.7f show the spatial electric field intensity distribution in the $xz$- and $yz$-planes, which include the nanoaperture antenna and a large portion of the suspension medium (water in this case). Indeed, this field distribution reveals a high gradient force field vector in the suspension medium towards the antenna aperture center. More discussion about the gradient trapping force is provided in Chapter 4.

#### 3.2.2.2 1540 nm dipole source FDTD simulation

In this part of the simulation, we looked at the nano aperture dimensions (i.e. $W$ and $H$ in Fig. 3.1b) that yield a good transmission enhancement at the 1540 nm wavelength. Taking into considerations the average UCNPs' size ($\sim 30\,\text{nm}$), we adjusted the aperture's gap $G$ to $\sim 40\,\text{nm}$.

Figure 3.8d illustrates the light transmission spectrum of the nanoaperture when it is illuminated using a plane wave source. A transmission peak at $\sim 1550\,\text{nm}$ was obtained for a nanoaperture dimensions of $W = 275\,\text{nm}$ and $H = 175\,\text{nm}$, with a 40 nm gap. The gold film thickness was kept fixed at 100 nm. The excitation source was a wide spectrum TFSF source with wavelength ranging from $0.30\,\mu\text{m}$ to $2.50\,\mu\text{m}$. The scattered field was collected and recorded at a 25 nm distance from the aperture surface in the epoxy region using a 2D FDTD field monitor that extends $10.0\,\mu\text{m}$ along each of the $x$ and $y$ axes.

Figures 3.8a and 3.8b show the 2D electric field intensity (in log scale) in the $xz$- and $yz$-planes. In this simulation, we used a single wavelength dipole source to record the electric field distribution in two orthogonal planes in the epoxy region. The epoxy region separates the gold film and the optical fiber channel. Although, the simulation region is relatively narrower in the $xy$-plane ($10\,\mu\text{m}\times 10\,\mu\text{m}$), both figures reveal a wide emission beam from the nanoaperture.

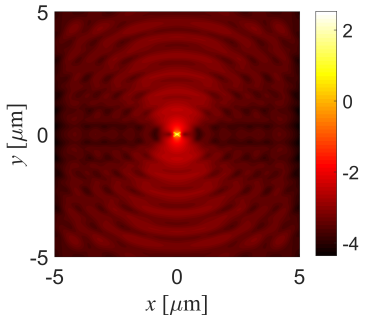


**(a)** Base-10 logarithmic scale, $log_{10}$, of the nanoaperture electric field intensity $|\mathbf{E}|^2$ in the $xy$-plane at $z = 100\,\text{nm}$ of the 3D FDTD simulation region.

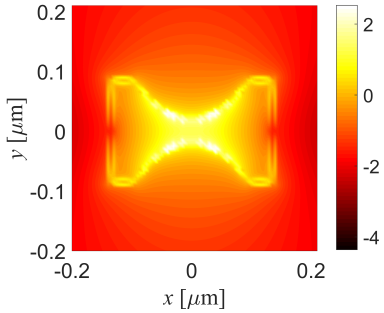


**(b)** Zoom-in view of the aperture field shown in subfigure (a).

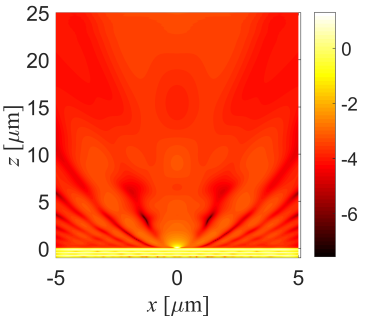


**(c)** Base-10 logarithmic scale, $log_{10}$, of the nanoaperture electric field intensity $|\mathbf{E}|^2$ in the $xz$-plane of the 3D FDTD simulation region.

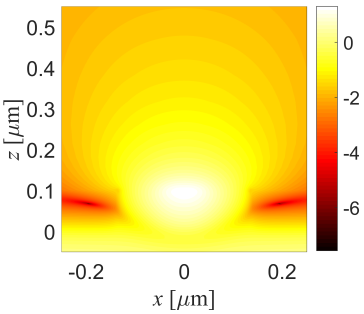


**(d)** Zoom-in view of the aperture field shown in subfigure (c).

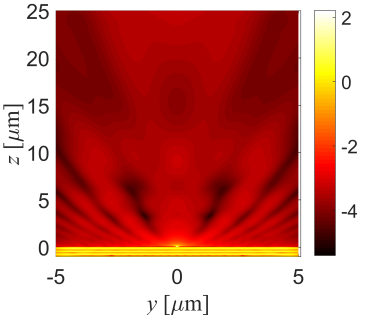


**(e)** Base-10 logarithmic scale, $log_{10}$, of the nanoaperture electric field intensity $|\mathbf{E}|^2$ in the $yz$-plane of the 3D FDTD simulation region.

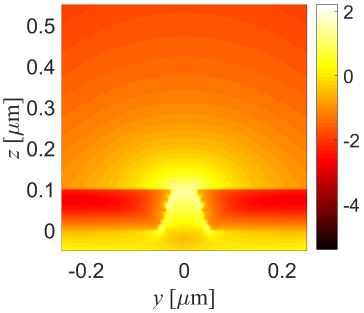


**(f)** Zoom-in view of the aperture field shown in subfigure (e).

**Figure 3.7:** 980 nm excitation near fields. Color bars show field intensity in base 10 logarithmic scale.

To give a clearer picture of the radiation pattern of the nanoaperture in the epoxy region, we used the FDTD method to transfer the aperture's near-field into a far-

field. Figure 3.8c shows the polar plot of the nanoaperture far field in two orthogonal planes (the $xz$-plane or $\phi = 0^{o}$-plane and the $yz$-plane or $\phi = 90^{o}$-plane, where $\phi$ is the azimuthal angle). As a matter of concern, the small NA of the SMF constitutes an extremely difficult challenge in the performance of the integration of the nanoantenna with the optical fiber. The small acceptance angle of the SMF ($\sim 11^{o}$) overlaps with only $\sim 10{-}15\,\%$ with the nanoantenna beam solid angle in the epoxy region, assuming the optical fiber waveguide and the antenna are vertically aligned.

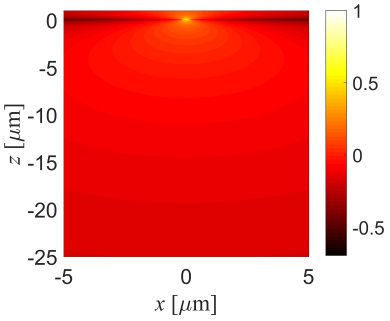


**(a)** Base-10 logarithmic scale, $log_{10}$, of the electric field intensity $|\mathbf{E}|^2$ normalized to the maximum value in the $xz$-plane of the epoxy layer due to a y-polarized dipole radiating at 1540 nm.

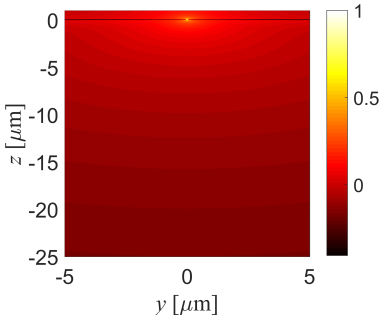


**(b)** Base-10 logarithmic scale, $log_{10}$, of the electric field intensity $|\mathbf{E}|^2$ normalized to the maximum value in the $yz$-plane of the epoxy layer due to a y-polarized dipole radiating at 1540nm.

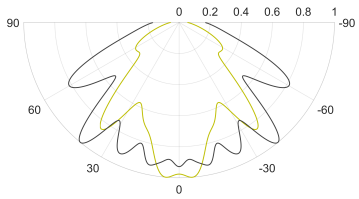


**(c)** Normalized polar plot of the electric field intensity $|E|^2$: in the $xz$-plane (azimuthal angle, $\phi = 0^{o}$-plane; green line), and in the $yz$-plane ($\phi = 90^{o}$-plane; black line).

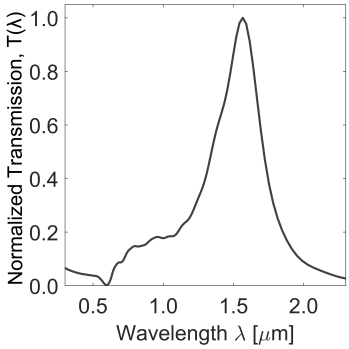


**(d)** Scattered light transmission through a $10\,\mu$m $\times$ $10\,\mu$m imaginary surface located 25nm away from the bowtie aperture of dimensions, $W = 275$ nm, 175 nm, and $G = 40$ nm. the gold film is 100 nm thick.

**Figure 3.8:** 1540 nm dipole source simulation figures. (a) Electric field intensity $|\mathbf{E}|^2$ in the $xz$-plane, (b) electric field intensity $|\mathbf{E}|^2$ in the $yz$-plane, (c) Polar plot of $|\mathbf{E}|^2$ in the two orthogonal planes, and (d) scattered field transmission spectrum.

#### 3.2.2.3 Discussion

The simulation results illustrated in Fig. 3.7 show the confinement of the electric field intensity in the subwavelength aperture gap of the bowtie antenna. The spatial field distribution illustrated in Figures 3.7c and 3.7e shows an obvious gradient in the field strength. It is high at the gap position and low at the far positions. This gradient in the field strength gives an indication of the electric force field vector and its direction which is important for optical trapping.

The simulation illustrated in Fig. 3.8 for the 1540 nm dipole emitter, on the other hand, shows a good enhancement of the antenna aperture for the 1540 nm emission wavelength. The directivity is also relatively good for a single antenna element.

## 3.3 Summary

In this chapter, we showed the fabrication steps of the nano aperture optical fiber tweezer (NAFT). We used the template-stripping method to transfer a circular metal-film, containing a nanoaperture at the center, onto the SMF tip. Also, we demonstrated the results of FDTD simulations regarding the bowtie nanoantenna radiation and transmission characteristics at 1540 nm (UCNPs luminescence), and 980 nm (trapping wavelength).

# Chapter 4

# Optical trapping using the nanoaperture optical fiber tweezer

## 4.1 Introduction

In this research, the nanoantenna discussed in the previous chapter has two preliminary functions. The first is to localize a high electric field intensity in a subwavelength volume when excited by a laser beam. An electric force field vector will be established due to the gradient of the localized electric field intensity within and around the antenna gap. This gradient in the intensity acts as the trapping force of the optical tweezer. The second function of the antenna is, upon trapping a nanoemitter, to enhance the light emission rate and radiation directivity of the trapped nanoparticle.

These two concepts are schematically illustrated in Fig. 4.1. A laser beam of excitation wavelength $\lambda_{exc}$ and power density, W/m$^2$, hits a plasmonic subwavelength aperture (shown as a black strip with a hole in Fig. 4.1) with a gap size $G$ and produces a localized electric field intensity $\mathbf{E}$ within the gap. This nanoaperture-supported electric field will, first, establish a gradient electric force field vector, which

is required for trapping nanoparticles suspended in the liquid chemical as illustrated in Fig. 4.1a. Secondly, once a luminescent nanoobject is drawn into the gap, it will be excited by the localized electric field and starts emitting photons as schematically illustrated in Fig. 4.1b.

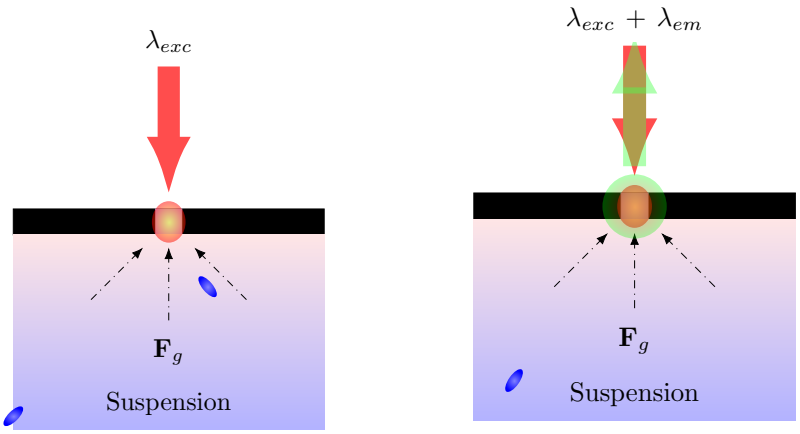


**(a)** Nanoparticle trapping.

**(b)** Trapped nanoparticle emission enhancement.

**Figure 4.1** – Schematic sketch illustrates the two main functions of the optical nanoantenna. The symbol $\mathbf{F}_g$, represents a gradient force field vector.

Taking advantage of previous work on trapping using aperture type nanoantennas, e.g. DNH [56], along with knowledge of the UCNPs' size and emission spectra, we found, based on FDTD simulations (some of which are discussed in Section 3.2.2), that the proposed bowtie shape was a good design option.

## 4.2 Optical trapping

Optical trapping is the use of electromagnetic radiation, particularly laser light, to locate small particles. These particles can be of a size comparable to or greater than the wavelength of the trapping electric field, or they can be of smaller size down to less than $\sim 10^{-2}$ of the wavelength. However, the interaction of the incident electric field

and the particle's electrons, in a Rayleigh scattering regime, results in an oscillating dipole moment that is proportional to the particle polarizability $\alpha$, and to the strength of the electric field vector $\mathbf{E}$, as follows [80]:

$$\mathbf{p} = n_m^2 \, r^3 \left( \frac{m^2 - 1}{m^2 + 2} \right) \mathbf{E} = \alpha \, \mathbf{E} \tag{4.1}$$

where $r$ is the particle's radius, and $m = \frac{n_p}{n_m}$, which is the relative refractive index of the particle, defined as the ratio of the particle's refractive index to that of the surrounding medium. This oscillating dipole moment scatters the incident field and changes its momentum.

A Rayleigh particle (r << $\lambda$, where $\lambda$ is the wavelength of the incident field) submerged in an electromagnetic radiation beam can be moved to the position of the highest electric field intensity of the beam. Two electromagnetic force field vectors spatially influence the net motion of the particle. One is the scattering force field vector $\mathbf{F}_\mathrm{s}$, and the other is the gradient force field vector $\mathbf{F}_\mathrm{g}$ [81]. The scattering force can be expressed as

$$\mathbf{F}_s = \frac{I_o}{c} \frac{128 \pi^5 r^6}{3 \lambda^4} \left( \frac{m^2 - 1}{m^2 + 2} \right)^2 n_m \, \mathbf{u}_s, \tag{4.2}$$

and the gradient force can be expressed as

$$\mathbf{F}_g = \frac{n_m}{2} \, \alpha \, \nabla |\mathbf{E}|^2 \, \mathbf{u}_g = \frac{n_m^3 r^3}{2} \left( \frac{m^2 - 1}{m^2 + 2} \right) \nabla |\mathbf{E}|^2 \, \mathbf{u}_g, \tag{4.3}$$

where $I_o$ is the intensity of the radiation beam, $\mathbf{u}_\mathrm{s}$ is the unit vector in the direction of the radiation beam, and $\mathbf{u}_\mathrm{g}$ is the unit vector in the direction of the point of highest field intensity as illustrated in Fig. 4.2.

Equation 4.2 shows that the scattered field force scales with the optical intensity of the radiation field and acts in the direction of the incident field. Differently,

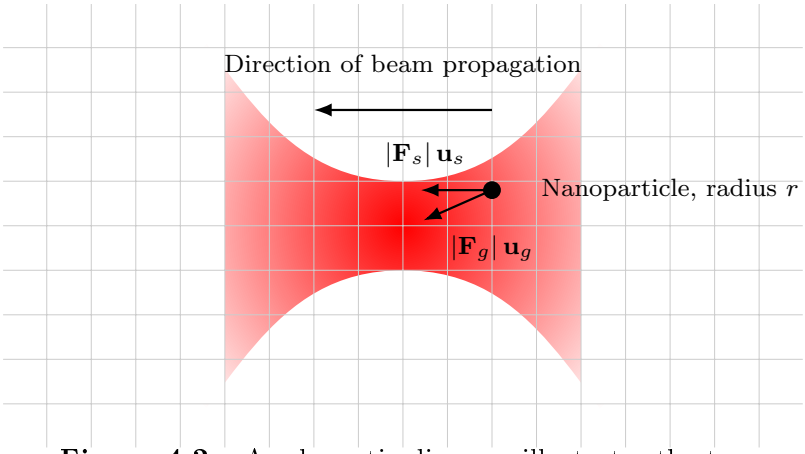


**Figure 4.2** – A schematic diagram illustrates the two trapping force vectors on a Rayleigh particle in a focused Gaussian beam. The dark spot at the minimum of the beam width represents the beam waste where the intensity of the field is highest.

Equation 4.3 shows that the gradient field force is proportional to the gradient of the electric field intensity and acts in the direction of the field's highest concentration. It should also be noticed that the scattering force scales with the $6^{th}$ power of the particle's size, whereas the gradient force scales with the $3^{rd}$ power of the particle's size, which makes it dominant over the scattered field force for subwavelength particles, $< 100\,\text{nm}$.

## 4.3 Near-field trapping using NAFT

Conventional optical tweezers, which use microscope setups, focus laser beams to trap micron and submicron particles [81]. Because of diffraction limitations, it is challenging to trap particles less than 100 nm in size, while keeping beam intensity within reasonable limits. Furthermore, Equation 4.3 shows that the gradient force field vector is proportional to the $3^{rd}$ power of the particle size. Therefore, trapping smaller particles requires an enhancement of the electric field intensity, which can be

provided by plasmonic nanoapertures.

An enhancement to the near-field optical trapping using nanoapertures in metal films is the self-induced back-action effect (SIBA) [82]. The SIBA effect is an interaction of the trapped object with the enhanced field within the trap. Small size particles can move faster in a suspension than bigger size particles, due to temperature fluctuation and low friction with the surrounding. Consequently, as the particle gets drawn into the trapping gap (potential well), unbalance in the system momentum occurs due to change in refractive index and this causes a restoring force to be established to balance the change in the particle's momentum and hence to enhance the particle's position in the trap.

Single and dual SMF waveguides (probes), which remove the need for a cumbersome microscope setup, have also been used for optical trapping . They are still subject to diffraction and can only trap relatively large particles [83–93]. Figures 4.3a and 4.3b schematically illustrate the use of single and dual optical fiber probes for trapping micrometer-sized dielectric particles.

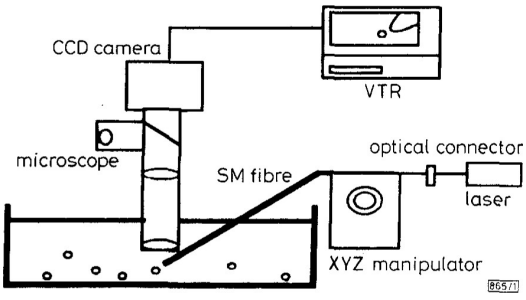


**(a)** Trapping micrometer-sized particles using single-fiber probe. Figure reprinted from [83].

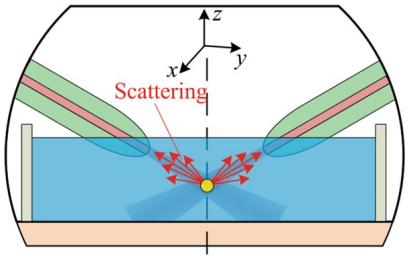


**(b)** Trapping micrometer-sized particles using dual-fibers probes. Figure reprinted from [93].

**Figure 4.3** – Schematic diagrams show the use of single and dual optical fibers to trap micrometer-sized particles. More details can be found in the relevant references.

To overcome the diffraction limitation, nanoholes in metal films have been exploited to

confine a high field intensity in a subwavelength volume scale. For example, double nanohole plasmonic nanoapertures, milled in a 100 nm thick gold film, have been successfully used to trap 20 nm dielectric nanospheres [54,94]. Fig. 4.4 shows a narrow gap nanoaperture used in a cumbersome microscope setup to trap the 20 nm dielectric beads.

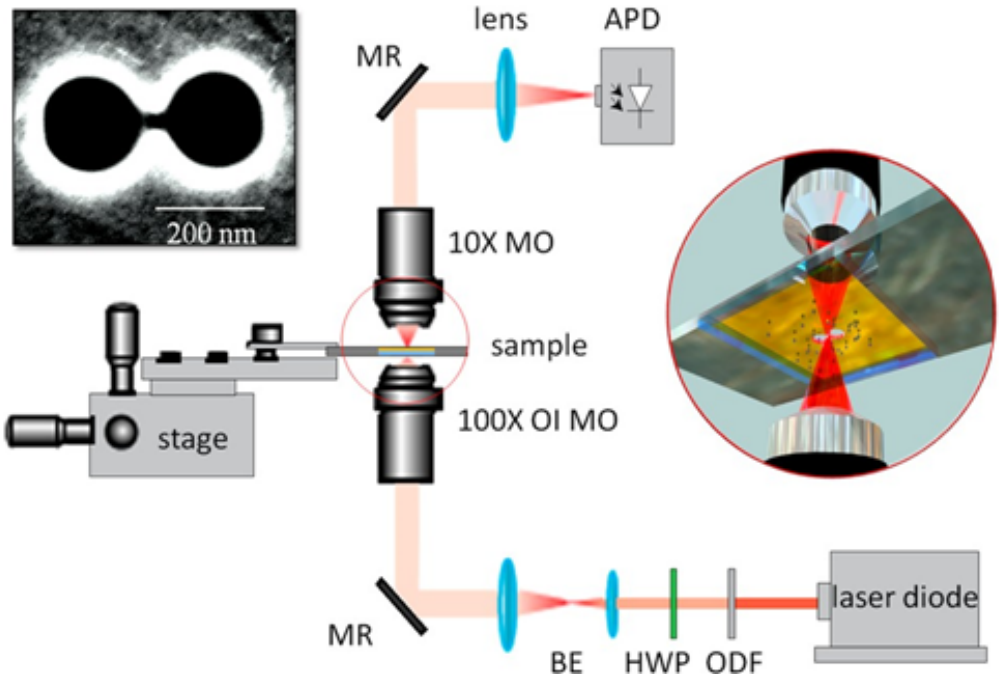


**Figure 4.4** – A metallic double-nanohole aperture, in a complex trapping setup, used for trapping 20 nm polystyrene nanospheres in a subwavelength gap. Figure reprinted from reference [94].

Different metallic nanoapertures have also been integrated on the tips of optical fibers, taking advantage of the superior waveguiding properties of the latter. For example, a near-field scanning aperture probe has been constructed using nanofabrication of a $\sim$ 100 nm circular hole on the end face of a metal-coated tapered optical fiber [95]. Another example is the direct nanofabrication of a double-nanohole on the tip of a

gold-coated optical fiber which has been used as an optical tweezer for trapping 20 and 40 nm size dielectric polystyrene nanospheres [56]. Our approach to integrating the metallic nano-aperture with the optical fiber, NAFT, is a template-stripping of planar nanofabricated nanoapertures. This direct planar nanofabrication of the nanoapertures on a metallic film is different from previous research [56, 96], in which nanofabrication was carried out on the fiber tip in the FIB.

In this section, the trapping results obtained by using NAFT are demonstrated. We show results of trapping 20 nm and 30 nm polystyrene nanospheres as well as the $NaYF_4$:20%$Yb^{3+}$/2%$Er^{3+}$ UCNPs.

### 4.3.1 Trapping 20 nm and 30 nm polystyrene nanospheres

Figure 4.5a shows the setup used to trap nanoparticles using the NAFT. The setup comprises a fiber-coupled 980 nm laser, fiber polarization control paddles, the integrated NAFT, a suspension vial, a neutral density filter, and a femtowatt photodetector. The neutral density filter was used to prevent saturation of the photodetector. The setup is flexible and compact. It is free of any microscope imaging optics or optical beam-alignment systems.

We used the same integrated NAFT for trapping two differently sized polystyrene nanospheres (refractive index 1.5731 [97]) of diameters 20 nm and 30 nm suspended in deionized-water with a percentage of 0.1 % $w/v$. The optical power incident on the nanoaperture was estimated to be $\sim 0.5\,\mathrm{mW}/\mu\mathrm{m}^2$ for $\sim 50$ mW of laser power. The polarization was oriented along the $y$-axis (see Fig. B.5c). Figures 4.5b and 4.5c show the time windows of the trapping events of the two nanoparticles as detected by the photodetector and recorded by a data acquisition unit. Both insets show small jumps of around 0.7 % and 0.9 %, respectively. A particle trapping release signature is also illustrated in Fig. 4.5d for the 30 nm polystyrene bead when the laser power is turned

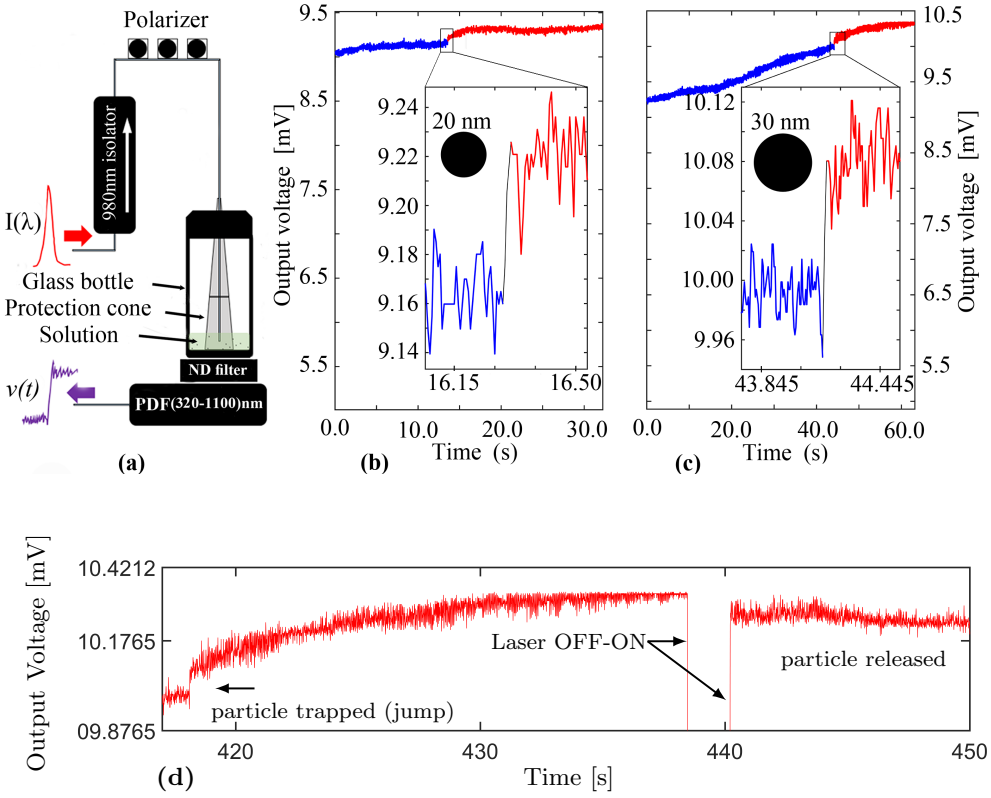


**Figure 4.5** – (a) Schematic of the experimental setup used for trapping 20nm and 30nm polystyrene nanospheres, where I($\lambda$) (red pulse) represents the laser signal and $v(t)$ (purple waveform) represents the output voltage. (b) 20nm particle trapping signal record. Trapping event in this time-window occurred after 13.585 seconds from turning on the laser. The inset is just an enlarged view of the trapping jump. (c) 30nm particle trapping signal record. Trapping event in this time-window occurred after 44.175 seconds from turning on the laser. The inset is an enlarged view of the trapping jump. (d) The 30nm particle release signature in response to turning off the laser power.

off and on. With deionized water alone, no jumps were observed. The experiment was repeated to achieve multiple trapping events for each particle size and on multiple fibers.

### 4.3.2 Trapping of UCNPs

The erbium-doped UCNPs ( $\beta$-$NaYF_4$:20%$Yb^{3+}$/2%$Er^{3+}$) are the source of 1550 nm photon emission in this study of single-photon sources. The emission from a cluster

of such nanoparticles was measured, and their emission spectrum in the wavelength ranges between $\sim 350\,\text{nm}$ to $\sim 1700\,\text{nm}$ is shown in Fig. A.2 in Appendix A. Having good trapping test results for the optical tweezer, trapping a single UCNP from these synthesized crystals is, therefore, a significant step in the study of photon emission statistics for these nanoparticles. For this purpose, we used the setup shown in Fig. 4.6**b**, which is simple and consists of the trapping medium (hexane), the NAFT, a 980/1550 nm optical fiber wavelength division multiplexer (WDM), and an APD. In the setup schematic diagram, the WDM has three ports (fibers); the red fiber represents the 980 nm port; the blue fiber represents the 1550 nm port; and the black fiber represents the common port. The WDM was designed to split or combine waves at the two different wavelengths. The excitation laser beam ($\sim 20\,\text{mW}$ at $\lambda = 980\,\text{nm}$) is inserted into the 980 nm arm of the WDM through an isolator and a polarizer (see Fig. 4.5**a**). Coupling of radiation (due to reflection, emission, or both) into the core of the SMF from the nanoantenna is guided to the APD aperture through the 1550 nm arm of the WDM and some density filters (not shown in the figure).

Unlike the trapping setup we used to trap the polystyrene nanospheres, which is based on change in transmitted field (or forward radiation) to register a trapping event, the setup we used to trap the UCNPs, which is shown in Fig. 4.6**b**, is based on the backward coupling of the field. A change in the refractive index in the gap of the nanoantenna causes the field intensity (radiation) to increase by a small amount which can be observed by the APD. Any potential emission from the trapped particle would also add to the field intensity coupled into the fiber. In this setup we used a $1 \times 2$ WDM coupler that is characterized by a low insertion loss ($\leq 0.3\,\textbf{dB}$, and high transmission $\sim 90\%$) at the desired wavelength, and a high suppression to the wave at the specified wavelength of the other arm of the WDM.

Figure 4.6 shows an example of trapping time-records for UCNPs suspended in

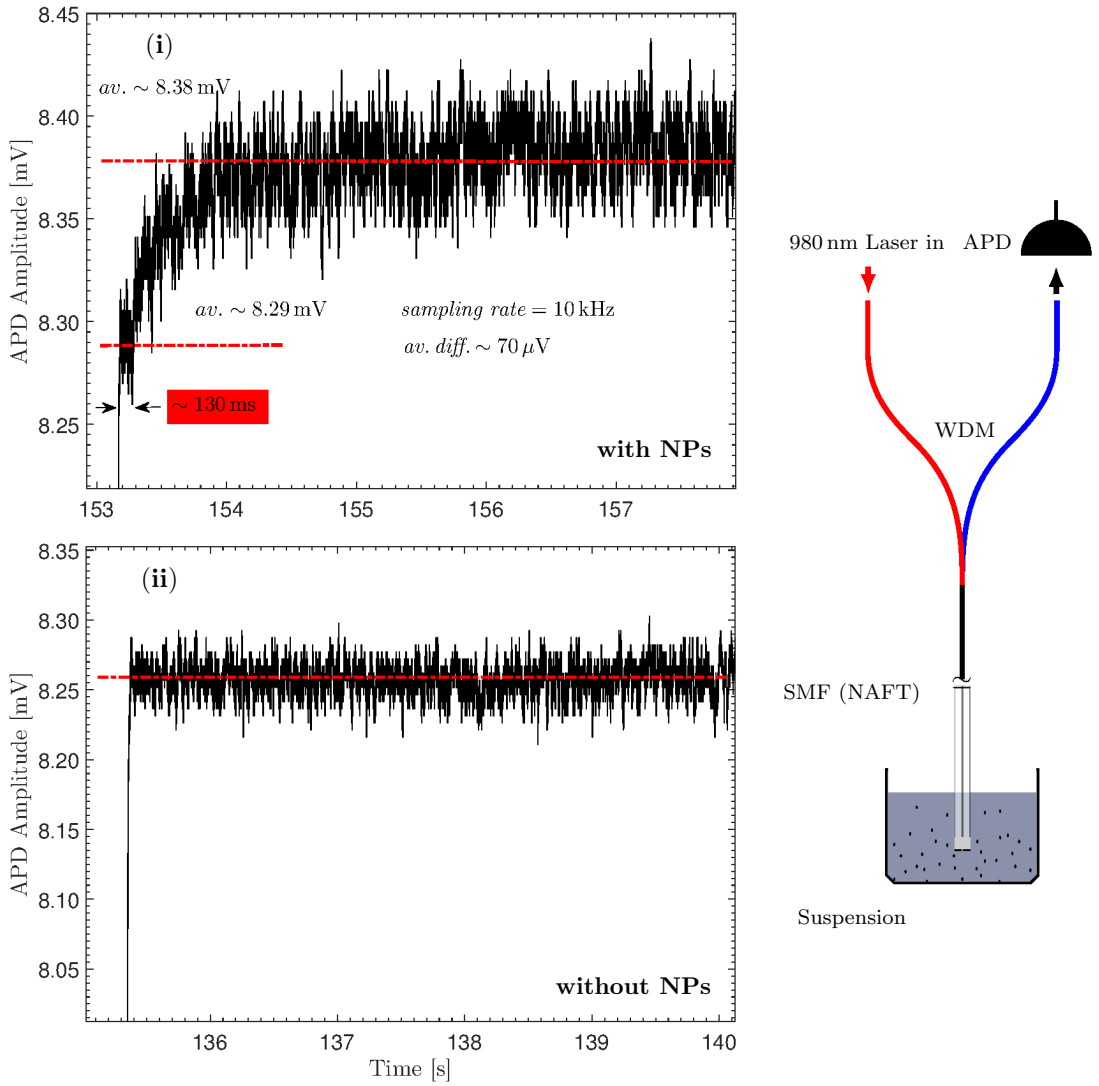


**Figure 4.6** – $\beta$-$NaYF_4$:20%$Yb^{3+}$/2%$Er^{3+}$ UCNPs trapping. (a) Trapping signal trace. (b) Schematic diagram for the trapping setup. The suspension is 1.5 mg of UCNPS in 1.0 mL of hexane. Longer trap signal traces can be found in Appendix B.6.

hexane. Plots of Figures 4.6(a)i and (a)ii demonstrate two trapping signals obtained experimentally using the setup shown schematically on the right of the figure. Figure 4.6(a)ii shows the case when the trapping medium is a pure hexane (no UCNPs). The signal in Fig. 4.6(a)i illustrates the case when the trapping medium contains

suspended UCNPs; suspension was sonicated for half an hour. It is worth noting here that the starting time of both signals represent the moment the laser was switched on. It is also obvious from the time trace of the two signals that they are different and have negligible time correlation at their start times.

The two fundamental differences between the No-trap and Trap signals can be observed through two markers in the sampled signals. The first is the change in signals average values, and the second is the signal amplitude fluctuation around the average. In the No-trap signal, the average value is mostly constant over time, and the signal fluctuation around the average is relatively small compared to that of the Trap signal. In the Trap signal time trace, there is a little positive jump in the signal average which is most probably caused by a nanoparticle being drawn into the high field region of the nanoantenna, trapped. Also, in the Trap case, the signal has a bigger fluctuation amplitude than that of the No-trap case.

To enhance our intuition that the time-trace of what we called a Trap signal reflects an event (a trapping event) caused by a change in the electric field intensity in the trapping gap, we looked at the correlation of each of the two signals. Figure 4.7**c** demonstrates the auto-correlation of the trapping signals (signal time slots are shown in (a) and (b)), which first shows the non-similarity between the two signals, and secondly, it shows that the No-trap signal decays a little faster than the Trap signal (the latter has greater correlation than the former) and this agrees with previous results on trapping a 20 nm polystyrene nanosphere in a DNH optical trap [94].

## 4.4 FDTD simulation of the trapping jump

In this section, we discuss the positive trapping jumps of the 20 nm and 30 nm polystyrene nanospheres. Using the FDTD technique, the change in far-field electric field intensity can be investigated by positioning a 25 nm polystyrene nanosphere

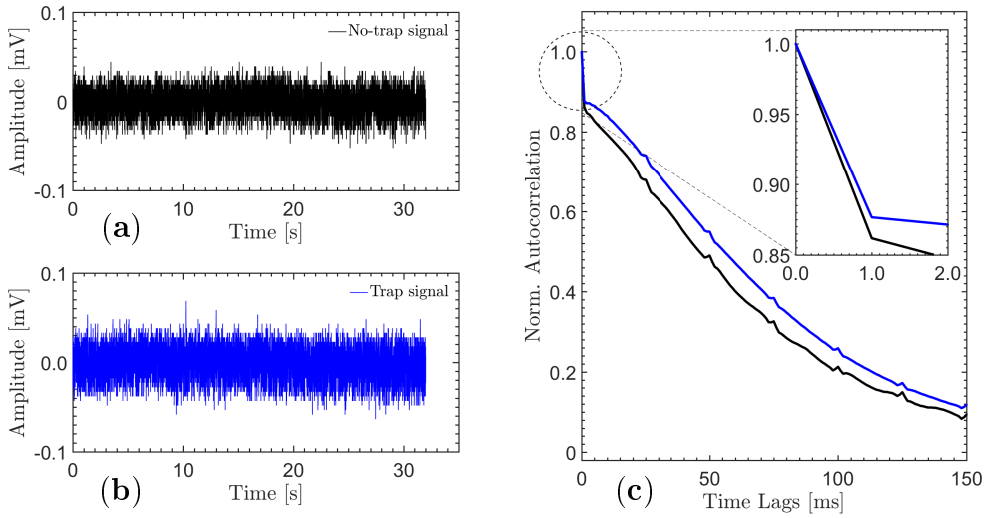


**Figure 4.7** – Trapping signals correlation: (**a**) 32 seconds of No-trap signal trace. (**b**) 32 seconds of Trap signal trace. (**c**) The normalized auto-correlation of each of the two signals. Each of the two trapping signals time windows given in (**a**) and (**b**) represent a 32 s time-slot taken from the full APD records as illustrated in Fig. B.8 in Section B.6.

in the aperture gap. As is well known, the far-field of an antenna can be measured by probing the near fields over an enclosing surface [98–100]. Numerically, however, we can record the near field amplitude and phase at points on a virtual surface in the numerical computation space, which can be located very close to the near field source. We used a $5\,\mu$m $\times$ $5\,\mu$m $\times$ $2.3\,\mu$m 3D FDTD simulation region divided, along the $z$-axis, into three main material regions: the epoxy region, $1.2\,\mu$m; the gold film region (includes the nanoaperture), $0.1\,\mu$m; and the water region, $1.0\,\mu$m, with the nanoaperture centered in the simulation region in the $xy$-plane. The aperture size extends 225 nm in the x-dimension, 175 nm in the $y$-dimension, and 100 nm in the $z$-dimension. To excite the structure, a $y$-polarized 980 nm plane-wave source located in the epoxy region at $1.0\,\mu$m away from the gold film. To calculate the near field, however, a field data monitor recorder with a virtual planar surface, which is only 2.5 nm away from the nanoaperture surface in the $+z$-direction, is used. The field

monitor records all the six electric and magnetic field components. The total number of the 3D cells generated is 52,032,946, from which 252,000 uniform cells, with a total size of 225 nm × 175 nm × 100 nm, fill the whole aperture region for the sake of improving simulation accuracy. The size of each of these uniform grids is 2.5 nm × 2.5 nm × 2.5 nm, whereas the cell size in the rest of the computation space is nonuniform. Besides, the simulation accuracy of the FDTD calculator was set to level 5/8 to reduce numerical simulation errors, the time stability factor to 0.95, and the FDTD simulation auto-shutoff to $1 \times 10^{-5}$. The auto-shutoff value is a measure of the energy left in the simulation region, and it is used to end the numerical calculations upon reaching this value.

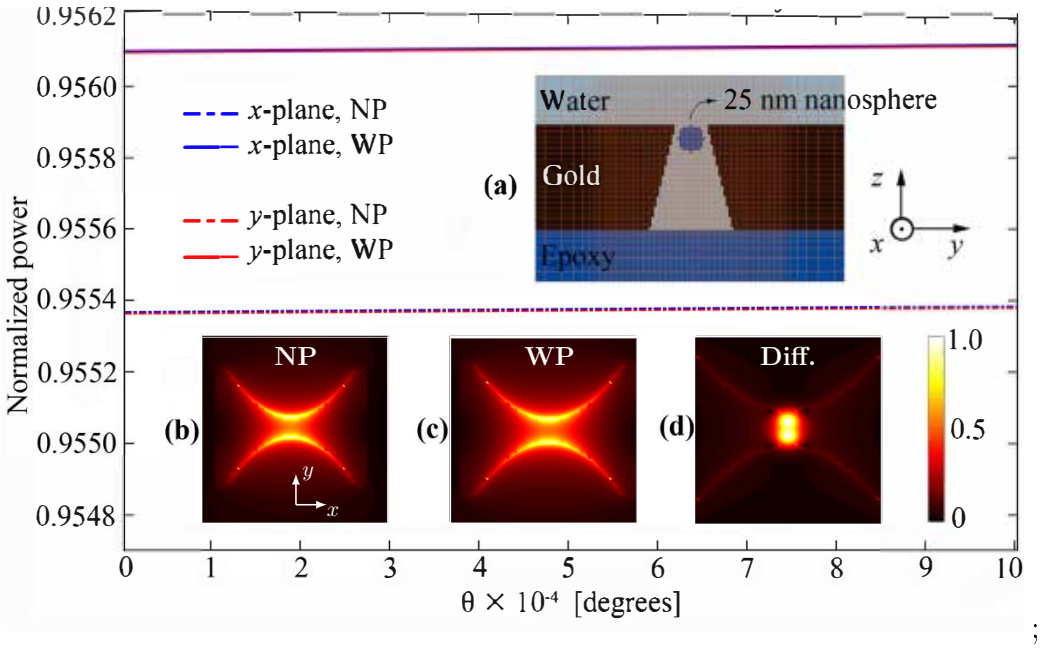


**Figure 4.8** – $x$-plane (blue lines) and $y$-plane (red lines) far-field normalized power for the no-particle (dash-dotted lines) and with-particle (solid lines) cases. Patterns are FDTD calculated 50 mm away from the nanoaperture for a cone-half-angle of 0.63° dictated by a photodetector aperture diameter of 1.1 mm. Inset (a) shows an enlarged view of a central part of the $yz$-plane ($x = 0$ plane) of the 3D simulation region with the 25 nm particle located in the tapered aperture. Insets (b), (c), and (d) show the no particle (NP), with particle (WP), and the difference (Diff.) in electric near field intensity at 2.5 nm away from the aperture's water-side surface.

Figure 4.8 shows the normalized far-field power emerging from the aperture, calculated within a cone specified by the photodetector aperture, both with and without the nanoparticle (25 nm). The observed step in the power pattern is nearly 0.079 % when the particle enters the hole. This step is too small compared to the measured trapping jump, but reasonable considering that we did not place the particle at the highest intensity point and that there are differences between an idealized antenna structure and the one fabricated. Another FDTD simulation (see Fig. B.9 in Appendix B), with the 25nm particle placed close to one of the nanoantenna gap crusts, shows a little better enhancement in power radiation and a jump of about 0.083%.

## 4.5 Summary

We have shown in this chapter the use of the optical fiber tweezer, NAFT, as an easy way to trap nanoparticles where 20 and 30 nm size polystyrene nanospheres trapping has been demonstrated. More importantly, trapping of light-emitting UCNPs has also been discussed, and a new trapping setup that uses the WDM has been illustrated. We showed in the trapping experiments that no cumbersome microscope nor other conventional optics are needed in the trapping process. The success in trapping the UCNPs is a crucial start for continuous work on the study of photon emission from a single UCNP, and it motivates us with the hope that we may get able to measure their photon statistics. Besides, we have demonstrated numerically, using the FDTD method, the positive trapping jumps for the polystyrene nanosphere.

# Chapter 5

# Plasmonic enhancement of light coupling into the SMF

## 5.1 Introduction

The coupling of electromagnetic field radiation into SMF waveguide channel is the most critical issue in building an efficient optical fiber tweezer. Since any impairments in the field intensity coupling, from communication perspectives, have a direct impact on the whole optical detection process. This issue is evident, particularly when extremely-low light emission intensity sources are concerned, e.g. luminescent single molecules and nanoparticles. As we previously mentioned in Section 1.1.3, the single-mode optical fiber has a low attenuation rate over the standard communication window ($\sim 1500-1600\,\mathrm{nm}$), but it also has a small numerical aperture that influences its ability to support a randomly incident radiation beam. We also have shown in Section 3.2.2.2, through an FDTD simulation, that the radiation pattern of a point source positioned at the center of a nanoaperture bowtie antenna has a broad angular field distribution and that only a fraction of the scattered power can be injected into

a low acceptance angle channel, the SMF. However, improving power coupling into the optical fiber can be achieved through enhancing the directivity of the antenna's radiated field. Nanoantenna performance betterment can be accomplished through harnessing the plasmonic properties of the gold film that contains the nanoaperture antenna by performing periodic discontinuities in the surface around the nanohole to enhance directivity and electric field intensity.

In this chapter, we discuss the numerical aperture concept of the SMF and introduce the basics of surface plasmon polariton waves that can be supported by a metal-insulator interface; and also, the experimental work that we carried out for improving power coupling into the SMF from the nano aperture antenna integrated at the fiber tip.

## 5.2 A quick insight about the optical waveguide

### 5.2.1 Geometrical description

In this section, we present a brief description of the optical fiber structure and the mechanism of total internal reflection that leads to waveguiding within the fiber. Optical fiber waveguides are fabricated from a high purity silica glass, which allows the diffusion of electromagnetic energy with shallow propagation loss. Further advantages of optical fiber channel are the enormous spectrum, electrical isolation, immunity to interference and crosstalk, ruggedness and flexibility, and small size and weight. An optical fiber channel is classified as a multi-mode fiber (MMF) channel or as a single-mode fiber (SMF) channel. The main difference between the two kinds of channels is the core size. However, a single-mode optical fiber waveguide has a tiny core diameter, which is in the range of $\sim 8.0 - 10.0\,\mu$m, and allows the propagation of the fundamental electromagnetic hybrid mode only, the $HE_{11}$ mode. Fig. 5.1a

is an optical microscope image that shows a typical single-mode optical fiber in size comparison with a sharpened pencil tip. The frontmost part of the fiber (see Fig. 5.1a) is a bare fiber, where the primary buffer coating (jacket) has been removed using a micro-stripper.

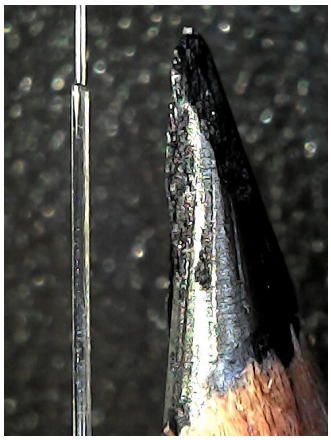

**(a)** SMF in comparison to a sharpened pencil.

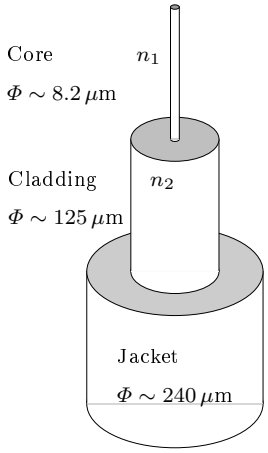


**(b)** A schemtaic diagram of SMF Core, cladding, and jacket.

**Figure 5.1** – Typical single-mode optical fiber (a), and schematic diagram (b).

Figure 5.1b shows a schematic for a typical structure of a single-mode optical fiber waveguide, a standard SMF that we have used in all of our experimental work presented in this thesis. It consists of a transparent silica glass core of size $8.2\,\mu$m and refractive index $n_1$, surrounded by an optically transparent cladding cylinder of size $125\,\mu$m and slightly smaller refractive index $n_2$, and the whole structure is surrounded by a primary protection jacket. Typical values for $n_1$ and $n_2$ are 1.4707 and 1.4640 (based on effective refractive index of 1.4679 and $NA = 0.14$ at 1550 nm). Ultimately, optical energy propagating in the fiber waveguide is supported by both the core and cladding, where most of it is confined in the core.

### 5.2.2 Numerical aperture

Propagation of light within the optical fiber waveguide can be described using simple ray optics as illustrated in Fig. 5.2. For an incident ray, which makes an angle $\phi_{oi}$ with the fiber axis (z-axis), on the interface between a medium of refractive index $n_o$ and the fiber's core, reflection and refraction occurs due to the index mismatch. Depending on the ratio $\frac{n_o}{n_1}$, the refracted ray in the core region tends to bend away from the z-axis (ratio $>1$) with a refraction angle $\phi_{1t}$ greater than $\phi_{oi}$ , or it bends towards the z-axis (ratio $<1$) with $\phi_{1t}$ is less than $\phi_{oi}$. Using Snell's law of refraction, the incidence and refraction angles of the impinging ray can be related to each other as follows [101]:

$$n_o \sin \phi_{oi} = n_1 \sin \phi_{1t}. \tag{5.1}$$

When the refracted ray in the cladding becomes parallel to the interface with the core,

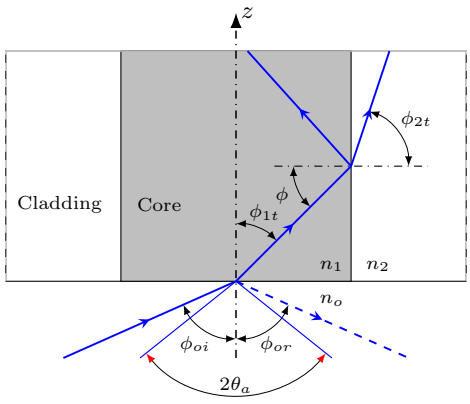


**Figure 5.2** – Ray optics picture of total internal reflection in single-mode step index fiber. All incident rays for which $\phi \geq \phi_c$ are totally reflected within the fiber core.

i.e. at $\phi_{2t} = 90^o$, the incident ray makes an angle that is less than $90^o$ (typically, it is very close to $90^o$). Therefore, based on the relation $n_1 > n_2$, there is a critical angle $\phi_c = \sin^{-1}(\frac{n_2}{n_1})$ for which all rays within the fiber core with $\phi > \phi_c$ will experience

total internal reflections, remain confined within the fiber core, and propagate over the optical channel.

The maximum value for the incident angle $\phi_{oi}$ that satisfy the condition of total internal reflection is referred to as the acceptance angle, $\theta_a$, of the optical fiber and, according to Eq. 5.1, is related to the critical angle as follows:

$$n_o \sin\theta_a = n_1 \cos\phi_c = (n_1^2 - n_2^2)^{\frac{1}{2}}. \tag{5.2}$$

The term $n_o \sin\theta_a$ is known as the numerical aperture (NA), which represents the

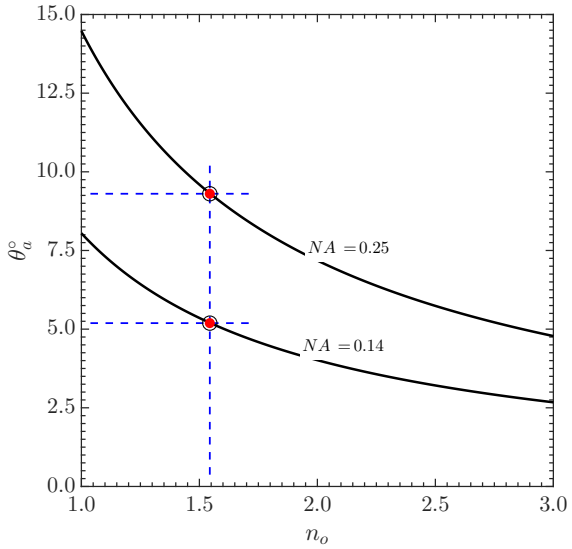


**Figure 5.3** – SMF acceptance angle, $\theta_a$, as a function of the surrounding medium refractive index $n_o$ for $NA = 0.14$ and $NA = 0.25$. The red dots on the curves highlight the acceptance angle of the SMF when the external medium has $n_o = 1.54$, the NOA61 epoxy index at 1550 nm wavelength.

capacity of the optical fiber to collect light. The graph in Fig. 5.3 is a plot of Eq. 5.2 for a range of $n_o$ values with $n_2$ set to a typically value of 1.464. For the case of a 0.14 NA, the plot shows that the acceptance angle has a maximum value of $\sim 8.0^o$ when the external medium refractive index has a value of 1 (air), and decrease to lower values as the index increases. In contrast, when the fiber NA is 0.25, the acceptance angle

reaches 14.5 degrees. However, at $\sim 1.54$ refractive index, which is a typical value for the epoxy material at 1540 nm wavelength, the full acceptance angle is $\sim 10.5°$ for 0.14 NA SMF, and $\sim 18.5°$ for 0.25 NA SMF.

## 5.3 Surface plasmon polaritons

### 5.3.1 Metal-dielectric interface SPPs

The existence of electromagnetic fields at the interface between a metal and a dielectric material pushes the metal free electrons at the surface to oscillate, and a new surface plasmon polariton (SPP) wave of energy confined to the interface can be created. The creation of such SPP wave requires that its propagation constant has to be greater than the wavevector of light on the dielectric material side of the interface, and that the two materials have opposite sign dielectric constants. The SPP energy confinement can be visualized as a result of the interaction of the transverse magnetic wave (with the electric field vector in the transverse plane perpendicular to the metal surface) with the metal surface charges. The SPP normal electric field component exponentially decays with distance from the surface (evanescent near field) [102, 103], see Fig. 5.4. Solving Maxwell's electromagnetic equations at the interface between an insulator, with a real and positive dielectric constant $\epsilon_d$, and a metal region of relative complex permittivity $\epsilon_m$ with negative real part, leads to the following dispersion relation [104]:

$$\beta = \frac{\omega}{c}\sqrt{\frac{\epsilon_d \epsilon_m}{\epsilon_d + \epsilon_m}}, \tag{5.3}$$

where $\beta$ is the wavevector of the supported SPP wave propagating at the interface between the two regions (note that it is declared as $K_{sp}$ in Fig. 5.4). More details regarding the derivation of Eq. (5.3) can be found in Appendix C.1.

Figure 5.5 is a plot for both of the gold dielectric constant $\epsilon_g(\omega)$, and the dispersion

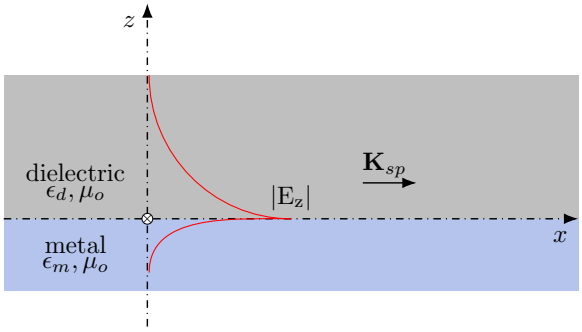


**Figure 5.4** – A schematic sketch shows the metal-dielectric interface in a 2D-view. Red line represents evanescent SPP wave propagating in the $x-$direction and decaying into the metal and dielectric materials, and perpendicular to the interface.

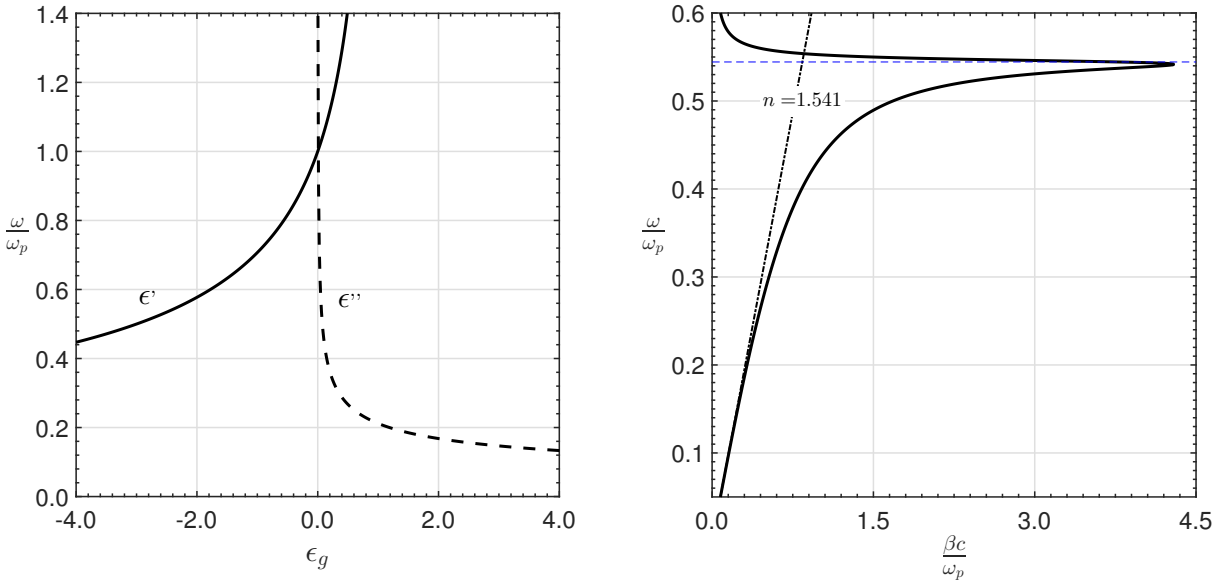


**Figure 5.5** – Left: gold $\epsilon_m(\omega) = \epsilon_m^{'}(\omega) + j\,\epsilon_m^{''}(\omega)$. Right: dispersion relation of Eq.(5.3) of a SPP at the interface between a Drude gold (plasma frequency $\omega_p = 1.323 \times 10^{16}$ rad. s$^{-1}$, and damping frequency $\zeta = 1.26 \times 10^{14}$ rad. s$^{-1}$) and epoxy dielectric material ($n = 1.541$).

relation of Eq. (5.3) for the gold-epoxy structure in the wavelength range from 100 nm up to 2000 nm. The dispersion curve for the SPP lies to the right of the epoxy material light line $\omega = cK_d$, where $K_d$ is the wavevector of light in the epoxy region. The SPP dispersion curve shows that electromagnetic energy confinement to the interface is more significant when the electromagnetic field oscillating frequency is closer to

the surface plasmon frequency (e.g. UCNPs green/red emission at $\sim 600\,\text{nm}$) than when the field oscillates at lower frequencies (e.g. UCNPs emission at $\sim 1540\,\text{nm}$). This wavelength dependence of SPPs influences the degree plasmonics to enhance nanoantenna field radiation intensity and directivity.

There are several ways to couple light to SPPs waves at a metal-dielectric interface. One method is through a prism that can be positioned directly, or with a nanometer-scale dielectric separation, on a negative permittivity thin metal film, Kretschmann and Otto configurations [105, 106]. Another way to excite SPPs at a single metal-dielectric interface is through shining light on a metal film that has protrusions, subwavelength holes, or periodic corrugations in the metal film [102, 103, 107–109].

### 5.3.2 Plasmonic grating

Figure 5.6 shows a schematic diagram of a rectangular grating, with a period $\Lambda$, composed of a metal and a dielectric (insulating) material. The momentum carried by a diffracted optical wave, of wavelength $\lambda$ and a wavenumber $K_d = K_o n_d$, where $K_o$ and $n_d$ are the free-space wavenumber and the dielectric material refractive index, at the grating surface can be enhanced to match the energy confinement requirements of a SPP wave at the interface. The $x$-component of the wavevector $\mathbf{K}_d$ of the diffracted

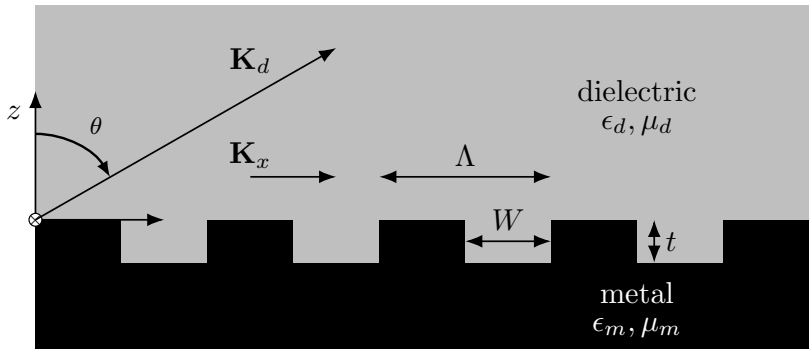


**Figure 5.6** – Diffraction of light at the surface of a metal-dielectric grating

optical wave parallel to the surface could be modified as following [102, 110]:

$$K_x \pm mK_g = K_x^{'}, \tag{5.4}$$

where $K_x$ is the $x$-component of the wavevector of the diffracted optical wave, $m$ is an integer, $K_g = \frac{2\pi}{\Lambda}$ represents the wavenumber of the grating, and $K_x^{'}$ is the modified wavenumber in the $x$-direction. Assuming nonmagnetic materials, the increase in momentum, to match that of a surface plasmon polariton wave, for the horizontal component of the diffracted optical wave given in Eq. (5.4) can be rewritten as follows:

$$K_o\, n_d \sin(\theta) \pm m\, K_g = K_o \sqrt{\frac{\epsilon_d\, \epsilon_m}{\epsilon_d + \epsilon_m}}, \tag{5.5}$$

where $\theta$ is the angle made by the diffracted wave with the normal to the grating surface, as shown in Fig. 5.6. Equation (5.5) shows that the diffracted wavevectors at the grating can be transformed into surface plasmon by taking up $\delta K_x = K_g$ and confine high field intensity at the gold film surface. The opposite can also take place where SPPs supported by the grating at the film surface can lose momentum (same $\delta K_x$) so that coupling of energy into a radiating light can occur.

## 5.4 Beaming light through a bow-tie nanoaperture at the tip of a single-mode optical fiber

In the previous sections, we mentioned that coupling light emission into a small numerical aperture SMF is a critical issue. In this section, we demonstrate numerical and experimental data regarding improving light coupling into the SMF using a subwavelength metallic nanoaperture at its tip. More precisely, we demonstrate light coupling into the SMF through enhancing radiation intensity from the nanoaperture

using a circular grating with a numerically optimized grating period.

### 5.4.1 Background

Substantial efforts have been devoted to improving light transmission through subwavelength apertures in a metal film since the reemergence of the plasmonics field motivated by the advancement in nanotechnology and nanoscale microscopy in the past two decades. Although a single nanoaperture can increase the field focus intensity in subwavelength dimensions, which makes it an essential element in optical tweezers [111–114] and plasmon-enhanced photon emission [115–118], it also scatters light in a broad radiation space resulting in poor directivity [119, 120]. This broad scattering limits the single nanoaperture use in applications requiring narrow-beam radiation. However, single and multiple (arrays) nanoapertures on thin metallic films have been widely used in manipulating light transmission and luminescence detection enhancement from a variety of fluorophores, e.g., emission from quantum dots [121–124], nitrogen-vacancy centers and molecules [125–128].

Several approaches have been proposed to improve photon emission using subwavelength apertures. One strategy is to texture a planar metal surface containing the nanoaperture deliberately. For instance, periodic sculpting of straight grooves on both sides of a nanoslit [121, 129–132] and circular grooves around a central photons source [126, 127, 133–137] are two examples that show improvement in the transmitted field intensity and directivity. Another approach to improve emission from single emitters, which has been theoretically proposed and demonstrated, is the use of a tapered metal probe with surface corrugation at the tip to enhance radiation directivity from a near light emitter [138]. In these previously mentioned configurations, photon detection can be efficiently achieved, with increased detection system complexity, by proper alignment of an objective lens with the planar structure that contains the sub-

wavelength aperture, or the emission source, which is not always easily achievable. An efficient method to collect photons from a single emitter is to directly couple radiation to a fiber channel, which can efficiently guide the signal to a light detector aperture. Different techniques of integrating a single nanoaperture with an optical fiber waveguide have been demonstrated. These nanoaperture optical fiber integrated probes have the advantage of making a flexible, alignment-free, compact, and easy excite-collect system [56, 139–144]. In other words, placing a plasmonic nanoantenna at the tip of an optical fiber channel will allow efficient radiation coupling into the fiber core. The design of such nanostructures often incorporates SPPs that confine light to the metal-dielectric interface and thereby enhance field intensity in the subwavelength aperture. Above all, adding corrugations on the transmission side of the integrated nanoaperture to enhance light coupling into the SMF core is still challenging and has not yet been demonstrated.

Plasmonic gratings have been extensively studied due to their geometric structure effect on SPPs. The momentum of these electromagnetic surface waves, waves that are supported by and confined to a dielectric-metal interface, can be harnessed to enhance the emerging field intensity and directivity of a plasmonic nanoaperture by modulating the interface periodically, a grating. Indeed, an optical grating has many geometrical parameters that can be controlled to achieve the performance required at a particular wavelength. Accordingly, analytical and numerical studies have been demonstrated for optimizing the grating structure, e.g., period, groove depth, and first groove center radius for circular gratings [145, 146].

In previous studies, separate dielectric and plasmonic gratings were utilized to couple light into an optical fiber channel, or a detector aperture (for example, a relatively high numerical aperture lens) [122, 147–151]. An alternative approach, also using a grating structure, is to directly integrate a grating-flanked nanoaperture in a

metal film with the SMF tip. This approach has the advantage over an objective lens scheme, where the radiation source can be placed very close to the fiber facet reducing collector-source alignment time and eliminating the cumbersome microscope lens system. Although low guiding losses characterize a regular communications SMF, it has a small NA that makes coupling of a divergent optical power from a nanoaperture into the fiber core difficult.

Here, using design supported with FDTD analysis, we experimentally demonstrate the enhancement of a 1536 nm free-space wavelength electromagnetic field radiation emerging from a nanoaperture that is directly placed at the SMF tip. The aperture is bow-tie-shaped and flanked with circular grooves in a 100 nm thick gold film. The grating can be tuned to a chosen wavelength through its geometric parameters. However, the interest in integrating the corrugated metal film with the fiber tip arises because it can effectively participate in supporting SPP waves on the metal surface, which can enhance the field emerging from the nanoaperture.

### 5.4.2 Plasmonic structure and integration with optical fiber

To realize the integration of a grating-supported plasmonic nanoaperture in Au film with the optical fiber tip, we followed three steps. First, we sputtered a 100 nm thick Au-film on a 1.0 cm $\times$ 1.0 cm smooth-surface glass substrate of 1.0 mm thickness. Second, we used the FIB to perforate the structures, shown in Fig. 5.7, in the metal film. After that, we used the previously described stripping method to transfer the structured gold film onto the SMF tip [144]. The milled circular film shown in Fig. 5.7a has a diameter of 130 $\mu$m (the outer FIB milling diameter is 144.8 $\mu$m). The bow-tie nanoaperture, Fig. 5.7c, which has dimensions of 350 nm $\times$ 170 nm in the xy plane, 100 nm thick, and an average gap of 60 nm along the z-axis, was milled at the center of the circular grooves that were dug centered in the circular Au film. A schematic view

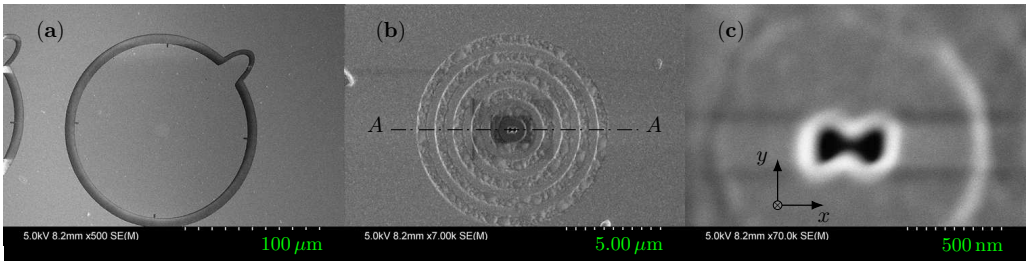


**Figure 5.7** – Scanning electron microscope (SEM) images. Image (a) shows one of multiple 130 $\mu$m diameter circular Au films performed by milling rings of outer diameter 144.8 $\mu$m using the FIB. The showing ring contains a grating (bullseye) structure at the center, which is shown enlarged in Image (b), flanking a center bow-tie hole. The hole is zoomed and shown in Image (c). The grating has a period of 980 nm; an outer diameter equals 9.8 $\mu$m and depth of $\sim$ 25 nm. The aperture has the dimensions 350 nm$\times$ 170 nm in the xy-plane and a 100 nm depth, and 60 nm average gap at the center. The dark spot at the center of Image (b) is due to SEM electron beam focusing. The small wing appears at the right-top of the film ring is for discharging when imaging the fiber tip using the SEM. Section A-A in (b) is schematically illustrated in Fig. 5.8b.

for the grating is shown in Fig. 5.8b, where $\Lambda$ (optimized to 980 nm) is the grating period, $t$ is the grating depth, and $a$ (980 nm) is the first groove center radius. The grating period was optimized using the FDTD method based on fixing the groove depth to $\sim$ 25 nm at the 1536 nm wavelength. Also, we performed several FDTD simulations at different groove depths, though, limiting our design to 25 nm groove depth to minimize direct transmission through the gold and ensure that the milling process could be prevented from going too deep given the tolerances of around 10 nm. Besides, and through practical experience, we found that increasing grooves depth causes the process of stripping-off the gold film from the glass substrate unsuccessful.

Gold has a complex dielectric function $\epsilon_m = \epsilon'_m + j\epsilon''_m = -112.80 + j10.97$ at 1536 nm wavelength, where $\epsilon'_m$ and $\epsilon''_m$ are the real and imaginary parts of the relative permittivity [152]. Between the Au film and the epoxy layer, a weak SPP wave can be guided at the interface with a wavenumber determined from the materials' dielectric constants as given by Eq. (5.3). At 1536 nm wavelength, Eq. (5.3) shows that a surface plasmon polariton mode with wavelength $\lambda_{sp} = 2\pi/\Re\{K_{sp}\} = 986$ nm can be

supported at the gold-epoxy interface, where $\Re$ means the real part. The grating is designed to match the momentum of the surface plasmon to the propagating beamed light. The corresponding skin depth at this wavelength for gold is $\sim 6$ nm [153, 154].

### 5.4.3 FDTD numerical simulations

To find the period for the grating that gives the best improvement in the field intensity and directivity, we used FDTD (Lumerical, FDTD Solutions Version 8.18.1365). We maximized the far-field transmitted power that is contained within a cone defined by the SMF acceptance angle (the angle $\alpha$ in Fig. 5.8b) as a function in the grating period, $\Lambda$.

To define our FDTD computation space, taking into considerations computer capacity to process data, we enclosed only a $15\,\mu$m $\times$ $15\,\mu$m of the Au film containing both the five-grooves grating and nanoaperture in the xy-plane and a $12\,\mu$m along the z-axis, using perfectly matched layer boundaries. Along the z-axis, the simulation region extends from $-2.0\,\mu$m to $10.0\,\mu$m as illustrated in Fig. 5.8a. Also, along the same axis, the Au film extends from $0.0\,\mu$m to $0.1\,\mu$m, and the epoxy layer extends from $0.1\,\mu$m to $10.0\,\mu$m. In addition to the far-field power calculations, this 3D simulation region allows for a direct numerical calculation of the electric field intensity at the expected position of the SMF tip ($\sim 8\,\mu$m from the Au film surface). The maximum extension of the grating in the xy plane considered in the FDTD simulation is $13\,\mu$m, which is $2\,\mu$m smaller than the simulation region extension in the xy plane.

Figure 5.8b shows a cross-sectional schematic diagram for the grating (section $A$-$A$ in Fig. 5.7b) together with part of the SMF in an integrated picture. Our estimation for the adhesion layer thickness, $8\,\mu$m, is based on SEM imaging (not shown here). The excitation source used in this FDTD simulation is a plane wave of 1536 nm wavelength, polarized along the y-axis and positioned at $z = -1.6\,\mu$m in the simulation

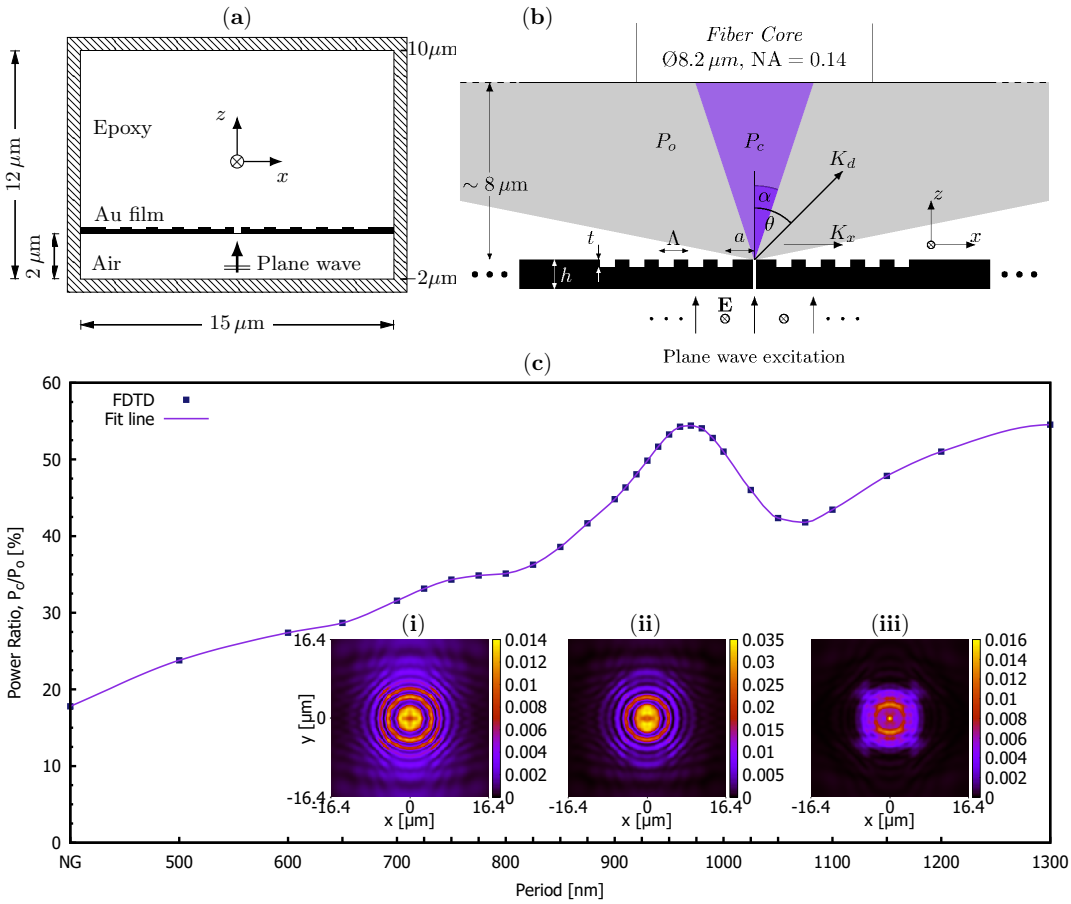


**Figure 5.8** – (a) xz-plane view of the FDTD simulation region. (b) A schematic diagram showing a cross-sectional view (section $A - A$ in Fig. 5.7b) of the grating and part of the SMF in an integrated form. Dimensions of $\Lambda$, $a$, $t$, and $h$ are, 980 nm, 980 nm, 25 nm, and 100 nm. The grey region, labelled as $P_o$, represents the total emerging power from the nanoaperture without grating, while the blue cone represents the maximum possible acceptable power by the SMF, $P_c$. The angle $\alpha$ represents the SMF acceptance angle. (c) FDTD simulation results for the ratio $P_c/P_o$ at different grating periods, $\Lambda$. Inset (**i**) shows the electric field intensity at 8 $\mu$m away from the bow-tie hole in a non-corrugated Au film. Inset (**ii**) shows the field intensity at 8 $\mu$m away from the bow-tie hole in an Au film with 5 annular grooves grating surrounding the hole, $\Lambda = 980$ nm. Inset (**iii**) shows the field intensity when there is no hole at the grating center. The color bar scale represents the field intensity in $(\mathrm{V/m})^2$.

region with a propagation vector in the $+z$-direction.

The simulation results depicted in Fig. 5.8c show the percentage of the maximum possible acceptable power by the fiber, $P_c$, relative to the total power, $P_o$, launched by

the nanoaperture without a grating at different grating periods, $\Lambda$. The graph shows a peak at 980 nm grating period that is in agreement with the SPP wavelength. It is noted that the wavelength of light in the epoxy is 17 nm longer than this period (i.e., the SPP wavelength is closer). $P_c/P_o$ at this period is 55 % which is three times its counterpart ($P_c/P_o = 18\,\%$) when no grating is used with the nanoaperture. We also show, in the same figure, the electric field intensity in the dielectric medium (at 8.0 $\mu$m away from the Au film in the $+z$-direction) for three cases for 10 mW incident power: without grooves (inset i), with five grooves of $\Lambda = 980$ nm around the nanoaperture (inset ii), and with grooves but no hole at the center (inset iii). Inset (iii) of Fig. 5.8c shows that the 100 nm Au film is not completely opaque to electromagnetic power flow, although its thickness is 13 times the skin depth. It also shows the confinement of the transmitted field caused by the grating. However, in all of the FDTD simulations, the optical fiber was not included, and we calculated the far-field power assuming a similar extension of the propagation medium (NOA61 epoxy, 1.541 refractive index at 1536 nm).

The SMF full acceptance angle $2\alpha$, which is defined by its NA, is $\sim 10.5^{\circ}$. This angle is small and presents a significant obstacle in coupling electromagnetic radiation into the SMF core. The data points shown in Fig. 5.8c draw a line of a peak value at the 980 nm grating-period, which corresponds to about 3 times improvement in power confinement.

A light ray emerging from the aperture with a wave number $K_d$ (see Fig. 5.8b) can be transformed into a plasmonic wave by increasing its momentum through the grating defined by the grating constant, $\Delta K_x = 2\pi/\Lambda$ as follows [102]:

$$K_x = n_d K_o \sin(\theta) + \Delta K_x = K_{sp}\,, \tag{5.6}$$

where $K_x$ is the modified wave number component in the x-direction (see Fig. 5.8b).

Quantitatively, from Eq. (5.6), at the 1536 nm excitation-wavelength, the surface plasmon polariton wavelength $\lambda_{sp}$ is 986 nm, which is very close to the optimum grating period, $\Lambda = 980$ nm that we obtained from the FDTD simulation.

### 5.4.4 Experimental results and discussion

Based on the results obtained from the FDTD simulations, which are shown in Fig. 5.8c, we fabricated two groups of circular Au films with a bow-tie-shaped hole at the center of each film, using the FIB. In one group, we sculpted the Au film with circular grooves surrounding the hole, and in the other group, we left the Au film surface smooth. As mentioned earlier, the stripping approach was used to transfer the structured Au film onto the tip of an SMF [144].

Figures 5.9a and b show schematic diagrams of an SMF tip with non-corrugated Au film (left fiber in Fig. 5.9a), and a corrugated Au film (left fiber in Fig. 5.9b). The cleaved end SMF on the right side, which has the same core and cladding size as that of the left SMF, represents the fiber-coupled source beam guiding channel (note that only part of the fiber cladding, which extends $\sim 60\,\mu$m along the radial dimension, is shown in all figures). The source power is 10 mW provided from a laser diode at a wavelength of 1536 nm through the cleaved end SMF with a manual polarization controller. Also, we used both configurations to measure the photon counts per second coupled into the SMF through the two different metal structures. However, during the experiments, we maintained the two fibers separated by a distance, d, of $\sim 25\,\mu$m, and aligned along the z-axis as shown in Fig. 5.9. It is worth mentioning here that each of the optical fibers was tightened to a 3-axis translation stage with differential adjusters, to allow for precise alignment and best response, through a long focal length microscope.

Similarly, Fig. 5.10 shows the photon collection through an objective lens ($\times 20$,

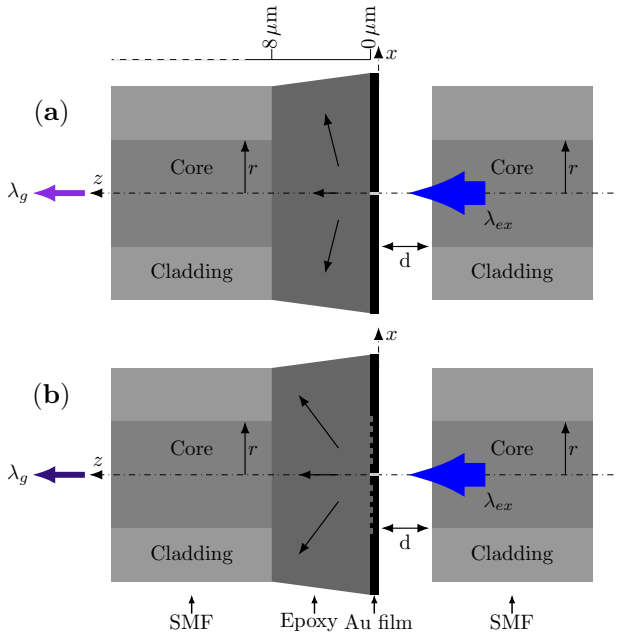


**Figure 5.9** – Fiber-fiber experimental setup partial schematic diagram: (a) Au film, $h = 100\,\text{nm}$, not corrugated, and (b) the film has 5 circular grooves of $\Lambda = a = 980\,\text{nm}$ and $t \sim 25\,\text{nm}$.

NA = 0.4) and the excitation is through the nanoaperture integrated optical fiber as indicated by the blue arrow in the figure. The separation, s, in this case, is dictated by the lens focal length, $\sim 2.5\,\text{mm}$. It is worth noting in Fig. 5.9 and in Fig. 5.10 that the outgoing wavelength is labeled as $\lambda_g$ to emphasize the fact that emission from the nanoaperture can be different from the excitation source wavelength, for example for luminescence studies. Also, we refer to these two schematic diagrams as "fiber-fiber" and "fiber-lens" partial setups for the sake of differentiation.

Figure 5.11 shows the average photon counts obtained from multiple experimental measurements. The data show clearly the effect caused by the plasmonic grating on the emerging field from the nanoaperture. Even though the 100 nm thick gold film is not 100 % opaque, the grating has effectively influenced the transmitted field and enhanced its intensity in a narrower beam. The differences in photon counts in both experiments indicate that an enhancement factor of $> 2$ (2.2 for the fiber-

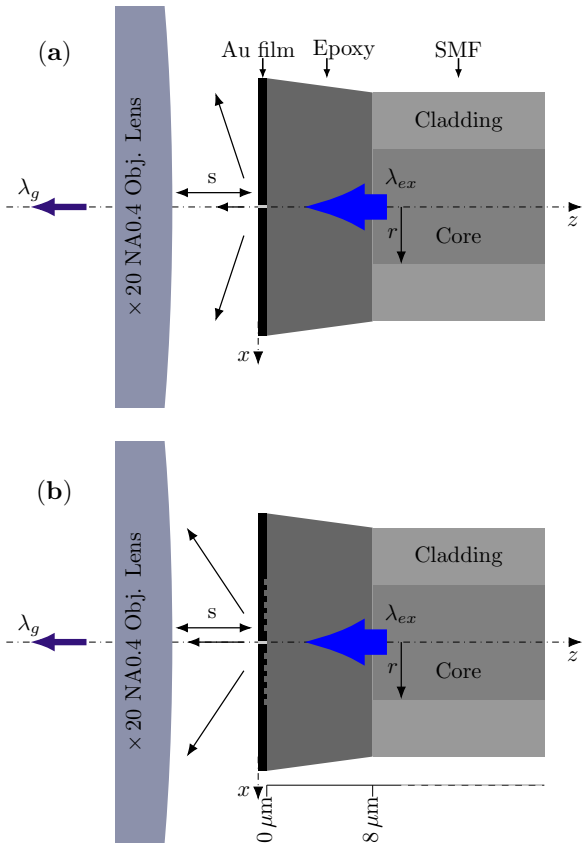


**Figure 5.10** – Fiber-lens experimental setup partial schematic diagram: (a) Gold film, $h = 100\,\text{nm}$, not corrugated, and (b) the film has 5 circular grooves of $\Lambda = a = 980\,\text{nm}$ and $t \sim 25\,\text{nm}$.

fiber experimental setup shown in Fig. 5.9, and 2.4 for the fiber-lens configuration of Fig. 5.10) is achieved due to the presence of the circular grating in the Au film around the nanoaperture. The photon counts measured through the objective lens were higher due to its sizeable numerical aperture, even though there is a large discrepancy in the refraction index of glass and air. Although the effect of the grating on one side of the metal film is noticeable, a dual grating system of circular grooves on both sides of the gold film would have a better coupling efficiency [127, 155, 156].

Fresnel reflection, on the other hand, is small at the fiber-epoxy interface ($\sim 7.2 \times 10^{-4}$, for 1.46 fiber core index and assuming s-polarized electric field), due to the slight difference in the index of refraction between the two media. The experi-

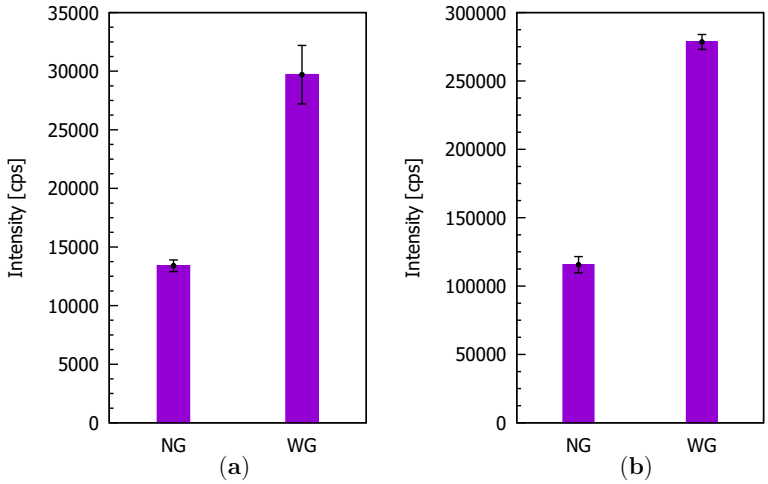


**Figure 5.11** – Average photon-counts, with error bars, obtained from multiple experimental measurements. (a) Fiber-Collection configuration, and (b) Lens-Collection configuration. The bars in the figure were labelled as NG and WG to denote no grooves and with grooves nanoantenna.

mentally measured data are in reasonable agreement with the FDTD data that show an enhancement factor of 3. The obtained results are also promising, particularly when considering the possibility of the radiation field source located within the nano aperture [56, 144, 157]; for instance, through optical trapping of a quantum emitter where a low-loss SMF channel can efficiently collect the emerging radiation through the grating.

## 5.5 Summary

In this chapter, we have discussed multiple points that are relevant to light coupling into the fiber core of the single-mode optical fiber. We presented a brief description of the optical fiber structure, the concept of total internal reflection and the fiber numerical aperture, surface plasmon waves, and the plasmonic grating. We have also demonstrated a $\sim 2-3$ times enhancement in light coupling efficiency through a bow-tie nanoaperture at the tip of an optical fiber, beaming to the SMF waveguide.

Due to the low optical transmissivity of a single nanoaperture in a metallic screen, we measured the photon counts per second to observe the grating influence on power coupling into the detection channel. We demonstrated two experiments for observing radiation enhancement from nanoapertures that we placed at the fiber tip. Based on the experimental results, the beamed field strength within the acceptance angle of the optical fiber, or of the objective lens, was enhanced by a factor of greater than 2 in both cases. Furthermore, we also used the FDTD numerical technique to show that by tuning the rectangular grating period to the plasmonic wavelength, the radiation intensity (directivity) is enhanced, and this agrees well with the experimental results obtained. This achievement can have a positive effect on supporting light emission and detection of nanoscale luminescent objects, e.g., light-emitting quantum dots, single molecules, and upconverting nanoparticles.

# Chapter 6

# Photon emission measurements

## 6.1 Introduction

This chapter is mainly devoted to show photon emission counting measurements at 1550 nm wavelength produced by $NaYF_4 : 2\%Er^{+3}18\%Yb^{+3}$ upconverting nanoparticles under near infra-red (NIR) continuous-wave (CW) laser excitation of 980 nm. More precisely, we are going to use a photon-counting data to estimate emission decay time $\tau$, and the second-order correlation function $g^{(2)}(\tau)$ of an optical signal input to an HBT optical detection setup. The input photon stream is an electromagnetic field that is generated in an optical trapping process using the NAFT and guided in an optical fiber channel to the HBT photon counter. Basic information on the erbium contained UCNPs have been given in Chapter 1, and a measured emission spectrum at 980 nm CW excitation can be found in Fig.A.2 in Appendix A.

In the previous chapters, the focus was on realizing the plasmonic enhanced optical fiber tweezer (NAFT) and improving light coupling into the fiber channel through a plasmonic grating around the tweezer trapping nanoaperture. Here, in this part of the work, our focus is on photon statistics of light that can be captured by the optical tweezer and coupled into the optical fiber channel. In order to do the photon counting

measurements, the light coupling into and propagating in the optical tweezer fiber waveguide is fed to a fiber-coupled superconducting-nanowire single-photon detector (SNSPD) operating at 2.4 °K.

## 6.2 Classification of light

Light consists of photons; each carries a discrete quantum of energy equal to $\hbar\omega$ where $\hbar$ is the reduced Planck's constant ($\frac{6.626}{2\pi} \times 10^{-34}$J.s) and $\omega$ represents the frequency. Depending on the properties of a light source, the statistical distribution data of a stream of emitted photons measured in a photon-counting experiment determine the kind of the light source. There are three fundamental types of light (photons) that can be identified through photon statistics for any stream of photons. Figure 6.1

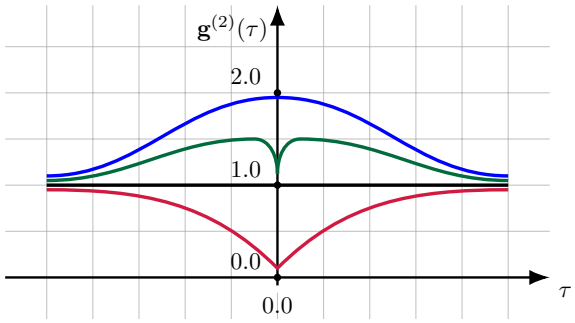


**Figure 6.1** – A sketch diagram showing photon statistics ($2^{nd}$-order coherence function) for three classes of light. The Gaussian blue line represents chaotic light (bunched light), the red line represents a nonclassical light (antibunched), the horizontal black line represents a perfectly stable wave with $\mathbf{g}^{(2)}(\tau) = 1$, and the green line represents a mixed state of light.

depicts a second-order correlation function sketch for the three types of light. The first (Gaussian blue line) represents a chaotic light, e.g., sun light, in which the photons have a bunched photon statistics. Second, the coherent light (black horizontal

line), e.g., a laser light, in which the photons have a constant photon statistics, and finally, the quantum light (red line) in which the photons have an antibunched photon statistics which are different from the previous ones. The electric field of such type of light is quantized and not classical, and it is usually referred to as a nonclassical light, e.g., emission from a single atom. Another state of light is a mixed state in which both bunched and antibunched photon statistics can be observed for a stream of photons (green line) [65, 158, 159].

### 6.2.1 Photon bunching and antibunching

Photons within a photon-stream generated by a monochromatic light source carry the same energy. Photon-streams from different sources have different photon statistics. However, if photons in a stream are more likely to arrive closely spaced in time than further apart, then the photons have a bunching property (classical field), and the source is a classical photons source. The opposite effect is if the wavepackets in the photon-stream are more likely to arrive far apart in time than close together, the photons are antibunched (quantized field), and the source is a nonclassical photons source. Examples of classical bunched photon-streams are those emitted from thermal and laser sources, whereas antibunched photon-streams can be obtained from, e.g., a single excited molecule or a QD. However, light can be attenuated to have a photon variance less than the photon mean number, which is a property of sub-Poissonian photon distribution, but still lacks the antibunching property of nonclassical light [18, 158–160].

### 6.2.2 Second-order correlation function, $\mathbf{g}^{(2)}(\tau)$

Distinguishing differences in photon-statistics of light emitted by different sources can be looked at by measuring the second-order correlation function $g^{(2)}(\tau)$. Each

of the sketch lines in Fig. 6.1 represents a particular photon statistics for a specific weighted series of energy packets. Therefore, measuring the $g^{(2)}(\tau)$ gives an excellent description of photon sources from the bunching and antibunching scale point of view. That is to say, the shape of the $g^{(2)}(\tau)$ curve determines the photon statistics of light emission from a source.

## 6.3 Single-photon detectors

An ideal form of an SPD is a photon sensor that produces a current pulse in response to one photon (at any optical wavelength) exciting its active area, the photosensitive aperture. Such a device would be able to distinguish single photons with 100 % detection efficiency. Also, a perfect SPD would have insignificant (zero valued) latency time, timing jitter, dead time, and be free of any dark counts or afterpulsing sources. Realistically, such a device does not exist; instead, several photon detectors with limited efficiencies are available, which can be used in single-photon measurements. Examples of these detectors include photomultiplier tubes, semiconductor devices, and superconducting nanowire photon detectors. Our experiments regarding single-photon measurements, which we demonstrate in this chapter, were conducted using a cryogenic superconducting nanowire single-photon detector from Single Quantum.

### 6.3.1 Photomultiplier tubes detectors

Photomultiplier tubes (PMTs) are based on their operation on two phenomena. The photoelectric effect (using a photo-sensitive material) and the subsequent generation of electrons (dynodes made of secondary-emissive materials). A few electrons emitted from a metal plate due to photon excitation can be accelerated (typical acceleration potential $\sim$ 1000 V) and multiplied, using multiple dynodes in a vacuum tube, to

produce a measurable current. Therefore, the energy of individual photons of light can be transformed into an electric current. PMTs typically have a dead time of $\sim 10\,\text{ns}$, which is too long for high rate photons. Also, PMTs have limited sensitivity to long wavelength photons, wavelengths that are $> 800\,\text{nm}$ [14, 161].

### 6.3.2 Semiconductor-based single-photon detectors

An example of semiconductor-based SPDs is the SPAD, single-photon avalanche diode. SPAD is a semiconductor *pn* junction device with a micrometer scale light-sensitive area. The device exploits the internal amplification mechanism that occurs due to an impact ionization generated by a high electric field vector in the *pn* junction, where a relatively large electrical current pulse can be generated in response to an incident photon on the sensitive area of the diode. Besides their low cost, small size, ruggedness, low power consumption, and high reliability, semiconductor-based SPDs have higher detection efficiency, especially in the red and near-infrared region of the optical spectrum [162].

### 6.3.3 Superconductor-based single-photon detectors

To measure the minimal amounts of energy packets, an extremely sensitive photon detector with excellent timing resolution is required. Superconducting-nanowires single-photon detectors (SNSPDs) have emerged as a practical choice for photon counting. Recent SNSPDs allow photon counting in less than 100 picoseconds of time, which makes them very useful when measuring photon emissions from quantum emitters that have nanoseconds emission-lifetimes or longer. However, the basic principle of photon-detection in such SNSPDs is based on the superconductivity of a current biased cooled nanowire that constitutes the detector aperture. The nanowire is usually structured in the form of a meandered-bridge that constitutes the active detection

area.

Furthermore, the SNSPD nanowires are maintained at cryogenic temperatures, usually below the critical temperature of the nanowire material. When a photon hits the nanowire, it creates a hotspot (a resistive region formed on the superconductor nanowire due to absorption of photon energy) and affects the bias current that passes through the nanowire bridge-structure [14]. Different superconducting microbridge nanowire sizes have been experimentally implemented; a nanowire of width $0.2\,\mu$m, $1.0\,\mu$m long, and 5.0 nm thick; another meandered nanowire to cover an area of $10\,\mu\text{m}\times 10\,\mu$m have been demonstrated. Fig. 6.2 shows a schematic that describes a nanowire electric circuit model [163–166].

An SPD, in general, is characterized by a bunch of attributes and performance parameters. One attribute is the detection efficiency, which is a measure of the probability that the detector will sense an incident photon, and it depends on the wavelength. Other critical characteristic properties include dark count rate and timing jitter of the detection system. The dark count rate is the average photon count registered by the SPD without any incident light, and it shows the minimum count rate level below which specific real photons cannot be detected. The timing jitter is an indication of the SPD response speed and is determined by its time response function. However, in SNSPDs, the nanowire can be meandered over a large surface area to achieve a high detection efficiency, e.g., $\sim 20\,\mu\text{m} \times 20\mu$m [167]. In this research, we use an SNSPD system that is characterized by a detection efficiency of $\sim 85\,\%$ at the wavelength 1550 nm, and timing resolution of 81 ps, from Single Quantum[1].

In the following sections, we demonstrate single-photon measurements on photon emission from a doped, Erbium (2%) and ytterbium (18%), sodium yttrium fluoride nanocrystals. These measurements represent phase number 3 of the research plan

[1]Single Quantum is a company, founded in 2012, which develops and manufactures single-photon detection systems based on the technology of superconducting nanowires

described in Section 1.2.

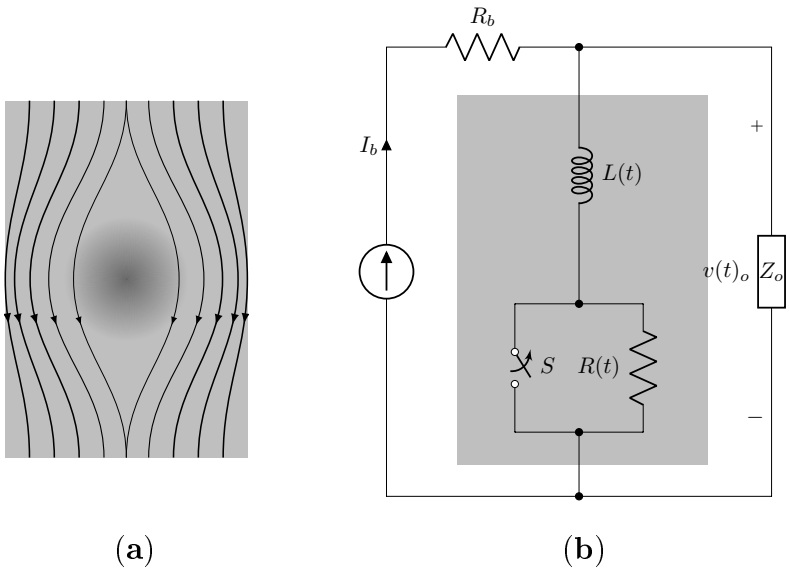


**Figure 6.2** – Simple SNSPD schematics. (a) A nanowire with a hot-spot caused by a photon incidence. The lines and arrows represent current passes in the nanowire. (b) Electric circuit model.

## 6.4 Single-photon sources

Single-photon sources are characterized by the emission of antibunched wavepackets and nonclassical photon statistics. The quality of the single-photon source can be determined by measuring the photon second order coherence function $g^{(2)}(0)$. However, single-photon sources can be broadly classified into two categories: on-demand single photons sources (deterministic), where the wavepackets emission time can be controlled, and sources of heralded pairs of entangled photons where the wavepacket emission time is determined by the detection of one photon of the photon-pair.

### 6.4.1 Deterministic source

Deterministic single-photon sources generate single photons on demand when triggered at a prescribed time. This type of on-demand single-photon sources can be obtained using pulsed laser excitation of a single quantum emitter, e.g., an isolated atom. Furthermore, the on-demand generation of single-photons may require that the process has to be of high efficiency and that the generated photons have to be indistinguishable. A simple sketch of a 2-level quantum emitter can be seen in Fig. 1.1 in Section 1.1.1.

### 6.4.2 Nondeterministic source

An example of nondeterministic single-photon sources is the photon-pairs generated in a parametric down-conversion (PDC) process using nonlinear crystals. In the PDC interaction, a high energy pump photon is converted into two photons (conventionally denoted to as *signal* and *idler*) as shown in Fig. 6.3.

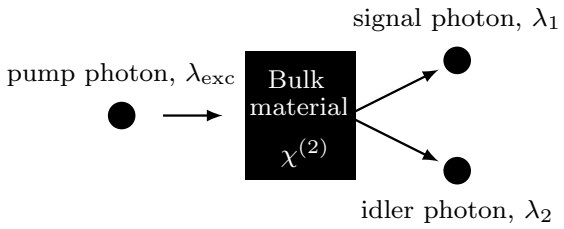


**Figure 6.3** – Schematic diagram of single-photon generation using PDC process.

The conversion of the pump-photon wavelength into two longer wavelengths heralded photons is due to the nonlinear properties of the pumped material. The PDC process is sometimes referred to as a three-wave mixing process where the medium exhibits a nonlinear polarization susceptibility $\chi^{(2)}$. The two photons generated from this nonlinear process are heralded photons, which means that detecting one photon gives a sign to the existence of the other photon [67, 168]. Practically, the PDC approach

to produce single photons is widely used in the quantum key distribution technology due to simplicity, high brightness, hight generation rate of photons, and the wide range of photon spectrum selectivity that can be attained using different pumps and different nonlinear crystals.

## 6.5 Photon counting experiments

In this section, we explore and demonstrate the experimental results that we obtained from photon-counting experiments using a two-channel SNSPD. The photon source we have used in our photon-counting experiments is neither a single quantum emitter nor a nonlinear material based single-photon source. Instead, it is hexagonal NaYF4 nanocrystals doped with erbium ions. The average size of these nanoparticles is $\sim 25\,\text{nm}$, which might contain thousands of luminescent lanthanide ions, $Er^{3+}$. Furthermore, the energy transfer between the sensitizers and activators (photons source) within the UCNP can be considered as a random process, which means that the number of useful activators is a probabilistic distribution; it could be high or low. Also, it has been demonstrated that every single UCNP absorbs much more photons than it emits, i.e., it has a meager quantum yield of $< 1\%$ [5].

### 6.5.1 Artificial photon-counting

As a leading forward step before demonstrating the real photon-counting experimental work results of light emission from the UCNPs, it is wiser to intuitively show some possible results that we might obtain using artificially simulated data. For this purpose, a virtual random-number based beam splitter (RNBBS), as an essential 2-channel HBT setup component, can be introduced to divide an artificially generated input photon-stream into two random streams $n_1(t)$ and $n_2(t+\tau)$, as shown in

Fig. 6.4(a). The random numbers used by the RNBBS have a uniform distribution in the interval $(0, 1)$ with mean equals 0.5, which are an excellent choice for splitting the input beam. The virtual output photons are captured and stored as time vectors where every individual element in each vector indicates a time of arrival for every individual photon-click at each channel path. Consequently, statistical correlation processing can be applied to the virtually stored data, and an image on the virtual-photon statistics $g^{(2)}(\tau)$ can be obtained.

The intensity form of the second-order correlation function $g^{(2)}(\tau)$ given by Eqn. (2.7), can be expressed in terms of random variables representing the number of clicks (photons) as [65, 169]

$$g^{(2)}(\tau) = \frac{\langle n_1(t) n_2(t+\tau) \rangle}{\langle n_1(t) \rangle \langle n_2(t+\tau) \rangle}. \tag{6.1}$$

The numerator of Eqn.(6.1) represents the cross-correlation between the two random variables, $n_1(t)$ and $n_2(t+\tau)$. A value of less than 1 for $g^{(2)}$, at zero time lag, would indicate an antibunched nonclassical kind of light; otherwise, if $g^{(2)}(0) = 1$, it indicates a coherent state of light, or a chaotic light if $g^{(2)}(0) > 1$.

The three different photon statistics of light can be estimated through a virtual simulation where artificial photon-streams of approximate relevant statistical properties can be produced for each kind of light. The fake photons can be then randomly divided into two random streams that can be detected at two virtual channels, as shown in Fig. 6.4(b). Building on that, for the case of quantum light, pure uniformly spaced time impulses can be generated and statistically tested. For instance, Figures 6.4(c,d) show the second-order correlation function $g^{(2)}(\tau)$ of $10,000$ recorded uniformly time spaced photon clicks at the virtual two photodetectors. The obtained $g^{(2)}(\tau)$ shows that the two stored time vectors have zero correlation value at zero time

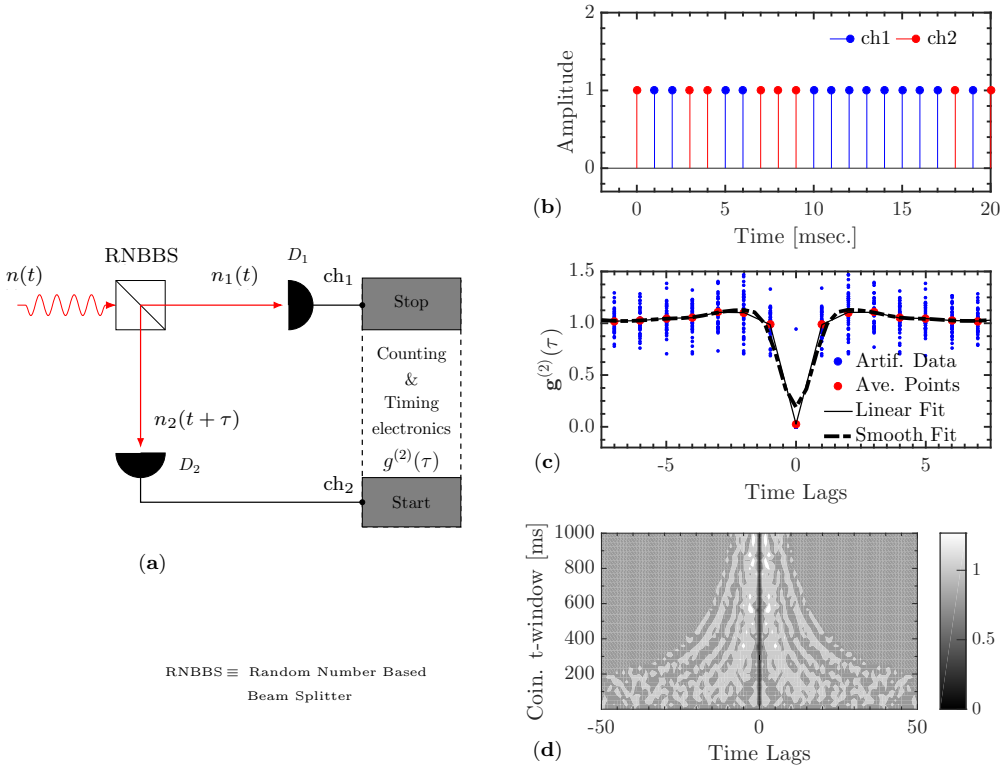


**Figure 6.4:** (a) Virtual HBT setup with artificial input photon-stream. (b) Sample (first 20 clicks) of the uniformly spaced photon stream (1 time unit, e.g., msec., spacing was assumed). (c,d) $g^{(2)}(\tau)$ plots; the first emphasizes the average line graph, and the second emphasizes the change in $g^{(2)}(\tau)$ as the coincidence time window changes.

lag. Also, the $g^{(2)}$ curve settles to the value 1 for increased time lags. Similarly, other randomly generated photon-streams with approximate chaotic and coherent properties can also be artificially generated and simulated through the virtual HBT setup. Graphical results for the later two types of photon streams are shown in Fig. C.2 in Appendix C for each type of light.

### 6.5.2 Experimental photon emission counting

In this section, we discuss the photon-counting results of light detected in a trapping experiment of erbium-doped UCNPs using a 980 nm CW laser. Figure 6.5 shows a

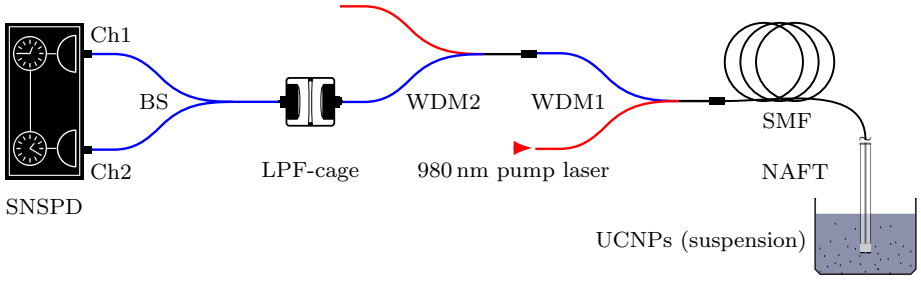


**Figure 6.5** – Schematic diagram for the experimental setup.

schematics of the experimental setup where the optical tweezer (NAFT) constitutes an essential part of the setup and through which the nanoparticle can be trapped and excited to emit light. The WDM allows for pumping using the 980 nm laser, and the backpropagation of light at the 1550 nm wavelength. In the setup, there are two WDMs to minimize back-propagating electromagnetic fields due to (i) reflections at the optical fiber connectors used to form the overall optical path, (ii) scattering at the NAFT tip, due to the metal film, and (iii) the cross-talk between the WDM ports. Also, to provide further blocking to backward propagations, we added a long-pass filter of rejection wavelength equal to 1250 nm. The excitation laser power output from WDM1 was in the range of 40 mW, but only $\sim 1/4$ of it reaches the optical tweezer tip due to the use of Fiber-Connector holder in the fiber path between the fabricated NAFT and the WDM. Moreover, at the filter end side, we have the optical fiber splitter ($50:50 \pm 5\%$), which is connected to channels Ch1 (1550 nm), and Ch2 (1310 nm) of the cryogenic SNSPDs.

In the same way, as we previously demonstrated in Chapters 3 and 4, the nanoantenna at the fiber tip confines a high field intensity in the gap that allows trapping of the hexane-suspended phosphorescent UCNPs. Once a nanoparticle gets trapped in the nanoaperture, absorption of energy becomes possible, as the UCNPs have already been synthesized to absorb energy at 980 nm. Part of the absorbed energy will be internally transferred to the luminescent erbium ions, and emission at 1550 nm as well

as at 550nm and 660 nm becomes possible, assuming energy quenching is insignificant.

The average size of the UCNPs is about 25 nm, which roughly means that thousands of erbium ions are contained in the nanoparticle structure. This massive number of ions means, in case of efficient energy transfer to the erbium ions that multiphoton emission may occur. Eventually, any possible light emission from the UCNP/s can be only partially coupled into the optical fiber channel and guided to the SNSPDs where photon click timestamps can be recorded.

#### 6.5.2.1 Experimental results

Figure 6.6 shows the results that we have obtained from the photon-counting experiment. The shown data represent 5.0 minutes of timestamps registered by the SNSPD using two channels. For comparison, two experiments were carried out to obtain the results given in the figure, one for the case when the hexane does not contain UCNPs, and the other for the case when the hexane contains 0.1 mg/ml of the UCNPs. The data given in Figures. 6.6(a,b) represent histograms for the registered timestamps at each channel (ch1 & ch2 in the figure) of the single-photon detector. The gray window shows the time of data considered in lifetime calculation given in Figures 6.6(c,f). The evaluated decay times (1.60 msec and 1.52 msec) can be conceived as the constant times for the sources of the photons arrived at the SNSPD. Figures 6.6(d,e,g,h) show the second-order correlation function for the two situations computed for 5.0 sec time slot (shown in green color in (a,b)). In both cases, the $g^{(2)}(\tau)$ curve seems slightly fluctuating around the 1.0 value, which means that the detected light is mostly coherent, a laser. Results of two more time slots data analysis, within the specified gray rectangle, produce approximately similar results, see Fig. C.3 in Appendix C.

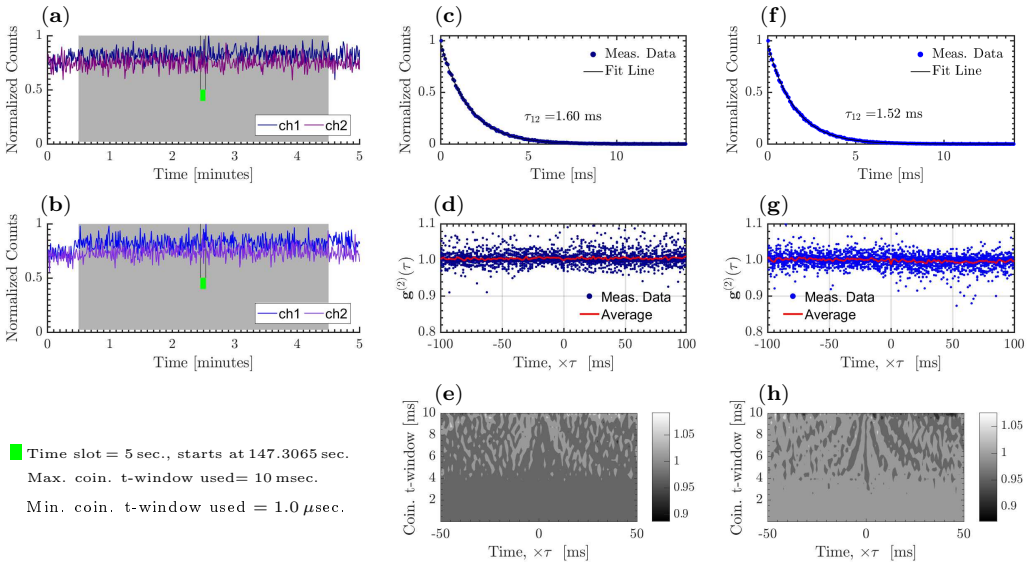


**Figure 6.6** – UCNPs trapping and photon emission measurements using two-channel SNSPD. (a) Photon-counts histogram for pure hexane probed with NAFT using a CW 980 nm pump laser. (b) Photon-counts histogram for 0.1 mg/ml concentration UCNPs suspension, using hexane. (c)-(e) show, respectively, the photon-arrival lifetime, $g^{(2)}(\tau)$, and the contour plot of $g^{(2)}(\tau)$ versus coincidence time window, for the pure hexane case. (f)-(h) show, respectively, the photon-arrival lifetime, $g^{(2)}(\tau)$, and the contour plot of $g^{(2)}(\tau)$ versus coincidence time window, for the UCNPs suspension. The text in the left bottom corner of the figure shows the duration of the time slot, which we used to process the measured data for the two cases. It also indicates the maximum coincidence time-window, in msec, which we used to estimate $g^{(2)}(\tau)$.

#### 6.5.2.2 Results discussion

The experimental data we obtained using the setup illustrated in Fig.6.5 reveal that photons detected by the SNSPD have more coherent statistical properties than any other type of light. In other words, the average second-order correlation function reflects more likely a coherent state of light. This constant state could be due to the detection of more 980 nm photons than any others since the reflection at the fiber tip is high and the cross-talk isolation between the WDM ports is not too high. Another reason could be that there has been no trapping occurred, and hence no other light has been detected. Likewise, there might be an emission from a trapped particle, but there were very few emitted photons that were covered by the presence of the 980 nm

signal.

Figure 6.6(b), the normalized photon counts, shows a clear jump in the count rate at the moment when the laser was switched on. This jump (noticed every time the laser is switched on), recorded by the SNSPD, enhances the interpretation that most of the photons arriving at the channel detectors have more likely coherence property. However, there might be trapping events of a UCNP, but its light emission and coupling into the SMF channel might be too weak that, on average, it could not be seen by the SNSPD.

On the other hand, the $g^{(2)}(\tau)$ contours image of Fig. 6.6(h) shows that chaotic behavior of the photons hitting the nanowires of the SNSPD can be revealed at wide coincidence time windows. In the same figure, narrowing the coincidence time window gives more chance for the coherent and quantum characteristics of photons hitting the nanowires to appear. Also, the $g^{(2)}(\tau)$ contours in both (e) and (h) images show that detected photons, for coincidence time windows of less than $\sim 2.0\,\text{msec}$, have a $g^{(2)}(\tau)$ that is constant ($\sim 1.0$) and independent of time $\tau$.

Finally, the erbium-doped UCNPs experimental photon-counting results, obtained using our nanofabricated optical fiber tweezer (NAFT), can be better improved if a pulsed 980 nm laser was used to excite the nanoparticles. Exciting a few quantum emitters using a CW laser, however, is possible and gives good results regarding $g^{(2)}(\tau)$, but information about emission lifetime becomes uncontrollable as demonstrated in [18, 19]. In either case, better experimental results would be obtained through fusion splicing the optical fiber terminals of the optical waveguide channel in the setup instead of using standard joint connectors. Fusion-splicing has the advantages that it eliminates noise insertion and reflections. Furthermore, from the data obtained regarding photon-number counting, the 980 nm photons were not adequately filtered.

Ultimately, it is worth mentioning here that all the results of the previous photon-counting tests are only preliminary and have not been repeated many times due to technical malfunction in the only available nanofabrication unit (FIB).

# Chapter 7

# Conclusion

In this thesis, we have demonstrated the phases of nanofabrication, integration, and usage of a simple optical tweezer for trapping luminescent nanoparticles and photon-counting measurements. The optical tweezer integrates the plasmonic properties of metals - more specifically, their ability to localize a high field intensity in a small gap - and the low-loss waveguiding properties of single-mode optical fibers. Plasmonic structures with tiny gaps can confine high field intensity in the subwavelength gap, which is essential in trapping particles of size $\leq 100\,\text{nm}$. The single-mode optical fiber, on the other hand, provides an excellent low-loss channel for guiding light over long distances at the 1550 nm.

The plasmonic nanoantenna has three main functions: it acts as an optical trap, trapping nanoparticles in its gap; it improves light emission beaming towards the optical fiber core; it enhances the radiation rate according to the Purcell effect. It is worth noting that the core size of a single-mode optical fiber is $\sim 9\mu$m, whereas the plasmonic aperture size is $\sim 0.3\,\mu$m. Accordingly, light coupling from a radiating nanoparticle trapped at the center of the plasmonic nanostructure into the optical fiber will undoubtedly be more efficient when the antenna and fiber are combined. Our approach to achieving the research goals was to divide the work-plan into three

stages: the nanofabrication stage, the integration stage, and the experimental stage.

In order to combine a subwavelength hole in a thin gold film with a single-mode fiber, we first performed planar nanofabrication of bowtie aperture nanoantennas, using the focused ion beam technology. Second, we used the template-stripping approach, utilizing ultra-violet curable epoxy as an adhesion material, to transfer a patterned gold film onto the optical fiber's tip. It is worth noting that aligning the fiber core with the nanoantenna along a common optical axis is a critical step in the integration process. For this reason, we used a low power laser beam injected into the fiber and monitored on an optical spectrometer for maximum transmission. Eventually, we have confidently realized a new optical fiber tweezer with a metal nanoantenna at the tip. We also think that our trapping technique will have a positive impact on replacing the current complicated optical trapping methods, which make use of costly and cumbersome optics.

In the experimental stage, we successfully trapped 20 nm and 30 nm polystyrene nanospheres as well as the upconverting nanoparticles, $\beta - \mathrm{NaYF_4}$:20 %$\mathrm{Yb^{3+}}$/2 %$\mathrm{Er^{3+}}$. What distinguishes our integrated nanoaperture fiber tweezer (NAFT), is that it replaces bulky microscope optics required in conventional trapping setups. It also enables faster experimental trapping efforts and with less expensive optics. In addition to the experimental work, particularly in the case of trapping the polystyrene nanospheres, we also used the FDTD numerical method to investigate the positive trapping jumps by comparing far-field intensities of light transmitted in both trapping and no-trapping situations. We showed through the FDTD simulation results that the positive trapping jump sensed by the APD is due to a minor increase in the detected radiation intensity caused by the trapping of the particle in the antenna high-field gap.

Since every single photon in photon-counting measurements is valuable, we fur-

ther improved the performance of light coupling into the SMF through surface corrugation, grating. The output metal-surface of the nanoantenna (from the 1550 nm light emission perspective) was textured with concentric circular grooves around the nanoaperture. Experimentally, we achieved an improvement in the light-beaming of factor $\sim 2.4$.

We also did some photon-counting measurements using a superconducting nanowire single-photon detector. The photons source we used was the erbium-yttrium co-doped NaYF4 nanocrystals, where NAFT was an essential part of the experiment's setup. The preliminary results we obtained about the photon-statistics of light emission from the UCNPs were not satisfactory as the 980 nm CW excitation laser photons were more likely to hit the single-photon detector nanowires as observed through the photon-counting and $g^{(2)}(\tau)$. In the end, it was impossible to quantify the numerical data we obtained, e.g., lifetime and $g^{(2)}(\tau)$, and relate it to our proposed source due to the domination of the high CW laser signal.

# Publications and Contributions

- **J. M. Ehtaiba** & R. Gordon, "Beaming light through a bow-tie nanoaperture at the tip of a single-mode optical fiber," Optics Express: vol. 27, Issue 10, pp. 14112-14120 (2019); https://doi.org/10.1364/OE.27.014112

- **J. M. Ehtaiba** & R. Gordon, "Integrated nanoaperture optical fiber tweezer," SPIE Conference: Nanoscience + Engineering, 2018, San Diego, California, United States; Proceedings volume 10723, Optical Trapping and Optical Micromanipulation xv; 1072330 (2018); https://doi.org/10.1117/12.2318907

- **J. M. Ehtaiba** & Gordon, R. (2018). "Template-stripped nanoaperture tweezer integrated with optical fiber," Optics Express: vol. 26, Issue 8, pp. 9607-9613 (2018); https://doi.org/10.1364/OE.26.009607

# Bibliography

[1] B. Lounis and M. Orrit, "Single-photon sources," *Reports Prog. Phys.*, vol. 68, no. 5, pp. 1129–1179, 2005.

[2] L. Huo, J. Zhou, R. Wu, J. Ren, S. Zhang, J. Zhang, and S. Xu, "Dual-functional $\beta$-NaYF4: Yb3+, Er3+ nanoparticles for bioimaging and temperature sensing," *Optical Materials Express*, vol. 6, no. 4, pp. 1056–1064, 2016.

[3] G. S. Yi and G. M. Chow, "Synthesis of hexagonal-phase NaYF4: Yb, Er and NaYF4: Yb, Tm nanocrystals with efficient up-conversion fluorescence," *Adv. Funct. Mater.*, vol. 16, no. 18, pp. 2324–2329, 2006.

[4] S. Fan, S. Wang, H. Sun, S. Sun, G. Gao, and L. Hu, "Efficient dual-mode up-conversion and down-shifting emission in $\beta$-NaYF4 :Yb3+ ,Er3+ microcrystals via ion exchange," *J. Am. Ceram. Soc.*, vol. 100, no. 7, pp. 1–9, 2017.

[5] J.-C. Boyer and F. C. Van Veggel, "Absolute quantum yield measurements of colloidal NaYF4: Yb3+, Er3+ upconverting nanoparticles," *Nanoscale*, vol. 2, no. 8, pp. 1417–1419, 2010.

[6] M. Kaiser, C. Würth, M. Kraft, I. Hyppänen, T. Soukka, and U. Resch-Genger, "Power-dependent upconversion quantum yield of NaYF4 :Yb3+ ,Er3+ nano- and micrometer-sized particles – measurements and simulations," *Nanoscale*, vol. 9, no. 28, pp. 10051–10058, 2017.

[7] M. Cvijetic and I. Djordjevic, *Advanced Optical Communication Systems and Networks*. Artech House, 2013.

[8] M. Ding, D. Fan, W. Wang, Y. Luo, and G.-D. Peng, "Basics of optical fiber measurements," *Handbook of Optical Fibers*, pp. 1–39, 2018.

[9] P. T. Kristensen, C. Van Vlack, and S. Hughes, "Generalized effective mode volume for leaky optical cavities," *Optics letters*, vol. 37, no. 10, pp. 1649–1651, 2012.

[10] A. E. Krasnok, A. P. Slobozhanyuk, C. R. Simovski, S. A. Tretyakov, A. N. Poddubny, A. E. Miroshnichenko, Y. S. Kivshar, and P. A. Belov, "Antenna model of the Purcell effect," *Nat. Publ. Gr.*, pp. 1–16, 2015.

[11] F. E. W. Beiglböck, J. Ehlers, K. Hepp, and H. Weidenmüller, *Quantum Information, Computation and Cryptography: An Introductory Survey of Theory, Technology and Experiments*. New York: Springer, 2010.

[12] T. D. Ladd, F. Jelezko, R. Laflamme, Y. Nakamura, C. Monroe, and J. L. O'Brien, "Quantum computers," *Nature*, vol. 464, no. 7285, pp. 45–53, 2010.

[13] E. Knill, R. Laflamme, and G. J. Milburn, "A scheme for efficient quantum computation with linear optics : Abstract : Nature," *Nature*, vol. 409, no. 6816, pp. 46–52, 2001.

[14] A. Migdall, S. V. Polyakov, J. Fan, and J. C. Bienfang, *Single-Photon Generation and Detection: Physics and Applications*, vol. 45. Academic Press, 2013.

[15] D. C. Burnham and D. L. Weinberg, "Observation of simultaneity in parametric production of optical photon pairs," *Phys. Rev. Lett.*, vol. 25, no. 2, pp. 84–87, 1970.

[16] B. Lounis and W. E. Moerner, "Single photons on demand from a single molecules at room temperature," *Nature*, vol. 407, pp. 491–493, 2000.

[17] B. Lounis, H. Bechtel, D. Gerion, P. Alivisatos, and W. Moerner, "Photon antibunching in single CdSe/ZnS quantum dot fluorescence," *Chem. Phys. Lett.*, vol. 329, no. 5-6, pp. 399–404, 2000.

[18] H. J. Kimble, M. Dagenais, and L. Mandel, "Photon antibunching in resonance fluorescence," *Physical Review Letters*, vol. 39, no. 11, p. 691, 1977.

[19] F. Diedrich and H. Walther, "Nonclassical radiation of a single stored ion," *Physical review letters*, vol. 58, no. 3, p. 203, 1987.

[20] X.-L. Chu, S. Götzinger, and V. Sandoghdar, "A single molecule as a high-fidelity photon gun for producing intensity-squeezed light," *Nature Photonics*, vol. 11, no. 1, p. 58, 2016.

[21] O. I. Mićić, H. M. Cheong, H. Fu, A. Zunger, J. R. Sprague, A. Mascarenhas, and A. J. Nozik, "Size-dependent spectroscopy of InP quantum dots," *J. Phys. Chem. B*, vol. 101, no. 25, pp. 4904–4912, 1997.

[22] Y. Wang and N. Herron, "Nanometer-sized semiconductor clusters: Materials synthesis, quantum size effects, and photophysical properties," *J. Phys. Chem.*, vol. 95, no. 2, pp. 525–532, 1991.

[23] M. Benyoucef, H. S. Lee, J. Gabel, T. W. Kim, H. L. Park, A. Rastelli, and O. G. Schmidt, "Wavelength tunable triggered single-photon source from a single CdTe quantum dot on silicon substrate," *Nano Lett.*, vol. 9, no. 1, pp. 304–307, 2009.

[24] A. L. Rogach, *Semiconductor Nanocrystal Quantum Dots*. Springer Wien NewYork, 2008.

[25] D. Englund, D. Fattal, E. Waks, G. Solomon, B. Zhang, T. Nakaoka, Y. Arakawa, Y. Yamamoto, and J. Vučković, "Controlling the spontaneous emission rate of single quantum dots in a two-dimensional photonic crystal," *Phys. Rev. Lett.*, vol. 95, no. 1, pp. 2–5, 2005.

[26] K. H. Madsen, S. Ates, J. Liu, A. Javadi, S. M. Albrecht, I. Yeo, S. Stobbe, and P. Lodahl, "Efficient out-coupling of high-purity single photons from a coherent quantum dot in a photonic-crystal cavity," *Phys. Rev. B - Condens. Matter Mater. Phys.*, vol. 90, no. 15, pp. 1–13, 2014.

[27] J. Claudon, J. Bleuse, N. S. Malik, M. Bazin, P. Jaffrennou, N. Gregersen, C. Sauvan, P. Lalanne, and J. M. Gérard, "A highly efficient single-photon source based on a quantum dot in a photonic nanowire," *Nat. Photonics*, vol. 4, no. 3, pp. 174–177, 2010.

[28] M. E. Reimer, G. Bulgarini, N. Akopian, M. Hocevar, M. B. Bavinck, M. A. Verheijen, E. P. A. M. Bakkers, L. P. Kouwenhoven, and V. Zwiller, "Bright single-photon sources in bottom-up tailored nanowires," *Nat. Commun.*, vol. 3, 2012.

[29] I. E. Zadeh, A. W. Elshaari, K. D. Jöns, A. Fognini, D. Dalacu, P. J. Poole, M. E. Reimer, and V. Zwiller, "Deterministic integration of single photon sources in silicon based photonic circuits," *Nano Lett.*, vol. 16, no. 4, pp. 2289–2294, 2016.

[30] O. Gazzano, S. Michaelis De Vasconcellos, C. Arnold, A. Nowak, E. Galopin, I. Sagnes, L. Lanco, A. Lemaître, and P. Senellart, "Bright solid-state sources of indistinguishable single photons," *Nat. Commun.*, vol. 4, 2013.

[31] N. Somaschi, V. Giesz, L. De Santis, J. C. Loredo, M. P. Almeida, G. Hornecker, S. L. Portalupi, T. Grange, C. Antón, J. Demory, C. Gómez, I. Sagnes, N. D. Lanzillotti-Kimura, A. Lemaítre, A. Auffeves, A. G. White, L. Lanco, and P. Senellart, "Near-optimal single-photon sources in the solid state," *Nat. Photonics*, vol. 10, no. 5, pp. 340–345, 2016.

[32] M. D. Birowosuto, H. Sumikura, S. Matsuo, H. Taniyama, P. J. Van Veldhoven, R. Nötzel, and M. Notomi, "Fast Purcell-enhanced single photon source in 1,550-nm telecom band from a resonant quantum dot-cavity coupling," *Sci. Rep.*, vol. 2, pp. 1–5, 2012.

[33] T. Miyazawa, K. Takemoto, Y. Nambu, S. Miki, T. Yamashita, H. Terai, M. Fujiwara, M. Sasaki, Y. Sakuma, M. Takatsu, *et al.*, "Single-photon emission at 1.5 $\mu$ m from an inas/inp quantum dot with highly suppressed multi-photon emission probabilities," *Applied Physics Letters*, vol. 109, no. 13, p. 132106, 2016.

[34] M. P. Hiscocks, C. J. Kaalund, F. Ladouceur, S. T. Huntington, B. C. Gibson, S. Trpkovski, D. Simpson, E. Ampem-Lassen, and S. Prawer, "Diamond waveguides: toward an all-diamond platform," *Proc. SPIE*, vol. 6801, no. December, p. 68010J, 2007.

[35] R. Albrecht, A. Bommer, C. Pauly, F. Mücklich, A. W. Schell, P. Engel, T. Schröder, O. Benson, J. Reichel, and C. Becher, "Narrow-band single photon emission at room temperature based on a single nitrogen-vacancy center coupled to an all-fiber-cavity," *Appl. Phys. Lett.*, vol. 105, no. 7, 2014.

[36] R. N. Patel, T. Schröder, N. Wan, L. Li, S. L. Mouradian, E. H. Chen, and D. R. Englund, "Efficient photon coupling from a diamond nitrogen vacancy

center by integration with silica fiber," *Light Sci. Appl.*, vol. 5, no. October 2015, pp. 1–6, 2016.

[37] C. Galland, Y. Ghosh, A. Steinbrück, M. Sykora, J. A. Hollingsworth, V. I. Klimov, and H. Htoon, "Two types of luminescence blinking revealed by spectroelectrochemistry of single quantum dots," *Nature*, vol. 479, no. 7372, pp. 203–207, 2011.

[38] S. Hohng and T. Ha, "Near-complete suppression of quantum dot blinking in ambient conditions," *J. Am. Chem. Soc.*, vol. 126, no. 5, pp. 1324–1325, 2004.

[39] R. Kolesov, K. Xia, R. Reuter, R. Stöhr, A. Zappe, J. Meijer, P. Hemmer, and J. Wrachtrup, "Optical detection of a single rare-earth ion in a crystal," *Nature communications*, vol. 3, no. 1, pp. 1–7, 2012.

[40] A. Dibos, M. Raha, C. Phenicie, and J. D. Thompson, "Atomic source of single photons in the telecom band," *Physical review letters*, vol. 120, no. 24, p. 243601, 2018.

[41] C. Yin, M. Rancic, G. G. de Boo, N. Stavrias, J. C. McCallum, M. J. Sellars, and S. Rogge, "Optical addressing of an individual erbium ion in silicon," *Nature*, vol. 497, no. 7447, pp. 91–94, 2013.

[42] S. Wu, G. Han, D. J. Milliron, S. Aloni, V. Altoe, D. V. Talapin, B. E. Cohen, and P. J. Schuck, "Non-blinking and photostable upconverted luminescence from single lanthanide-doped nanocrystals," *Proc. Natl. Acad. Sci.*, vol. 106, no. 27, pp. 10917–10921, 2009.

[43] L. E. Mackenzie, J. A. Goode, A. Vakurov, P. P. Nampi, S. Saha, G. Jose, and P. A. Millner, "The theoretical molecular weight of NaYF4:RE upconversion nanoparticles," *Sci. Rep.*, vol. 8, no. 1, p. 1106, 2018.

[44] H. X. Mai, Y. W. Zhang, L. D. Sun, and C. H. Yan, "Size- and phase-controlled synthesis of monodisperse NaYF4:Yb,Er nanocrystals from a unique delayed nucleation pathway monitored with upconversion spectroscopy," *J. Phys. Chem. C*, vol. 111, no. 37, pp. 13730–13739, 2007.

[45] S. Xu, W. Xu, B. Dong, X. Bai, and H. Song, "Downconversion from visible to near infrared through multi-wavelength excitation in Er3+/Yb3+ co-doped NaYF4 nanocrystals," *J. Appl. Phys.*, vol. 110, no. 11, pp. 1–8, 2011.

[46] A. D. Ostrowski, E. M. Chan, D. J. Gargas, E. M. Katz, G. Han, P. J. Schuck, D. J. Milliron, and B. E. Cohen, "Controlled synthesis and single-particle imaging of bright, sub-10 nm lanthanide-doped upconverting nanocrystals," *ACS Nano*, vol. 6, no. 3, pp. 2686–2692, 2012.

[47] K. J. Russell, T.-L. Liu, S. Cui, and E. L. Hu, "Large spontaneous emission enhancement in plasmonic nanocavities," *Nat. Photonics*, vol. 6, no. 7, pp. 459–462, 2012.

[48] G. M. Akselrod, C. Argyropoulos, T. B. Hoang, C. Ciracì, C. Fang, J. Huang, D. R. Smith, and M. H. Mikkelsen, "Probing the mechanisms of large Purcell enhancement in plasmonic nanoantennas," *Nat. Photonics*, vol. 8, no. 11, pp. 835–840, 2014.

[49] J. Wenger, P.-F. Lenne, E. Popov, H. Rigneault, J. Dintinger, and T. Ebbesen, "Single molecule fluorescence in rectangular nano-apertures," *Opt. Express*, vol. 13, no. 18, pp. 7035–7044, 2005.

[50] A. Nevet, N. Berkovitch, A. Hayat, P. Ginzburg, S. Ginzach, O. Sorias, and M. Orenstein, "Plasmonic nanoantennas for broad-band enhancement of two-

photon emission from semiconductors," *Nano Lett.*, vol. 10, no. 5, pp. 1848–1852, 2010.

[51] E. C. Kinzel, P. Srisungsitthisunti, Y. Li, A. Raman, and X. Xu, "Extraordinary transmission from high-gain nanoaperture antennas," *Appl. Phys. Lett.*, vol. 96, no. 21, pp. 88–91, 2010.

[52] T. W. Ebbesen, "Bright unidirectional fluorescence emission of molecules in a nanoaperture with plasmonic corrugations," *Nano Lett.*, pp. 637–644, 2011.

[53] G. Lu, W. Li, T. Zhang, S. Yue, J. Liu, L. Hou, Z. Li, and Q. Gong, "Plasmonic-enhanced molecular fluorescence within isolated bowtie nano-apertures," *ACS Nano*, vol. 6, no. 2, pp. 1438–1448, 2012.

[54] A. A. Al Balushi, A. Zehtabi-Oskuie, and R. Gordon, "Observing single protein binding by optical transmission through a double nanohole aperture in a metal film," *Biomed. Opt. Express*, vol. 4, no. 9, p. 1504, 2013.

[55] R. Regmi, A. A. Al Balushi, H. Rigneault, R. Gordon, and J. Wenger, "Nanoscale volume confinement and fluorescence enhancement with double nanohole aperture," *Sci. Rep.*, vol. 5, no. 1, p. 15852, 2015.

[56] R. M. Gelfand, S. Wheaton, and R. Gordon, "Cleaved fiber optic double nanohole optical tweezers for trapping nanoparticles," *Optics Letters*, vol. 39, no. 22, pp. 6415–6417, 2014.

[57] K. H. Drexhage, "Influence of a dielectric interface on fluorescence decay time," *J. Lumin.*, vol. 1-2, no. C, pp. 693–701, 1970.

[58] P. Goy, J. M. Raimond, M. Gross, and S. Haroche, "Observation of cavity-enhanced single-atom spontaneous emission," *Phys. Rev. Lett.*, vol. 50, no. 24, pp. 1903–1906, 1983.

[59] P. Anger, P. Bharadwaj, and L. Novotny, "Enhancement and quenching of single-molecule fluorescence," *Phys. Rev. Lett.*, vol. 96, no. 11, pp. 3–6, 2006.

[60] L. Novotny and B. Hecht, *Principles of Nano-Optics*. Cambridge: Cambridge University Press, second ed., 2012.

[61] D. A. Atwood, *The Rare Earth Elements: Fundamentals and Applications*. John Wiley & Sons Ltd, first ed., 2012.

[62] P. Lalanne, C. Sauvan, and J. P. Hugonin, "Photon confinement in photonic crystal nanocavities," *Laser & Photonics Reviews*, vol. 2, no. 6, pp. 514–526, 2008.

[63] C. Sauvan, J. P. Hugonin, I. S. Maksymov, and P. Lalanne, "Theory of the spontaneous optical emission of nanosize photonic and plasmon resonators," *Phys. Rev. Lett.*, vol. 110, no. 23, pp. 1–5, 2013.

[64] R. Chance, A. Miller, A. Prock, and R. Silbey, "Fluorescence and energy transfer near interfaces: The complete and quantitative description of the Eu+ 3/mirror systems," *The Journal of Chemical Physics*, vol. 63, no. 4, pp. 1589–1595, 1975.

[65] R. Loudon, *The Quantum Theory of Light*. OUP Oxford, 2000.

[66] R. Hambury Brown and R. Q. Twiss, "Correlation between photons in two coherent beams of light," *Nature*, vol. 177, no. 4497, pp. 27–29, 1956.

[67] C.-K. Hong, Z.-Y. Ou, and L. Mandel, "Measurement of subpicosecond time intervals between two photons by interference," *Physical review letters*, vol. 59, no. 18, p. 2044, 1987.

[68] G. Armendáriz, J. Cravioto-Lagos, V. Velázquez, M. Grether, E. López-Moreno, and E. Galvez, "Teaching quantum mechanics with the hong-ou-mandel interfer-

ometer," in *Education and Training in Optics and Photonics*, p. EWB4, Optical Society of America, 2013.

[69] P. Biagioni, J.-S. Huang, and B. Hecht, "Nanoantennas for visible and infrared radiation," *Reports Prog. Phys.*, vol. 75, no. 2, p. 024402, 2011.

[70] A. Ahmed, Y. Pang, G. Hajisalem, and R. Gordon, "Antenna design for directivity-enhanced Raman spectroscopy," *Int. J. Opt.*, vol. 2012, 2012.

[71] A. Kinkhabwala, Z. Yu, S. Fan, Y. Avlasevich, K. Müllen, and W. E. Moerner, "Large single-molecule fluorescence enhancements produced by a bowtie nanoantenna," *Nat. Photonics*, vol. 3, no. 11, pp. 654–657, 2009.

[72] Z. Cui, *Nanofabrication: Principles, Capabilities and Limits*. Springer, second ed., 2017.

[73] J. I. Goldstein, D. E. Newbury, J. R. Michael, N. W. Ritchie, J. H. J. Scott, and D. C. Joy, *Scanning Electron Microscopy and X-Ray Microanalysis*. Springer, 2018.

[74] Y. Pang, G. Hajisalem, and R. Gordon, "Directivity-enhanced Raman spectroscopy using a parabolic reflector nanoantenna," *Proc. IEEE Conf. Nanotechnol.*, pp. 564–567, 2011.

[75] M. Ghorbanzadeh, S. Jones, M. K. Moravvej-Farshi, and R. Gordon, "Improvement of Sensing and Trapping Efficiency of Double Nanohole Apertures via Enhancing the Wedge Plasmon Polariton Modes with Tapered Cusps," *ACS Photonics*, vol. 4, no. 5, pp. 1108–1113, 2017.

[76] S. Kumar, T. W. Johnson, C. K. Wood, T. Qu, N. J. Wittenberg, L. M. Otto, J. Shaver, N. J. Long, R. H. Victora, J. B. Edel, *et al.*, "Template-stripped

multifunctional wedge and pyramid arrays for magnetic nanofocusing and optical sensing," *ACS applied materials & interfaces*, vol. 8, no. 14, pp. 9319–9326, 2016.

[77] D. Yoo, T. W. Johnson, S. Cherukulappurath, D. J. Norris, and S.-H. Oh, "Template-stripped tunable plasmonic devices on stretchable and rollable substrates," *Acs Nano*, vol. 9, no. 11, pp. 10647–10654, 2015.

[78] T. W. Johnson, Z. J. Lapin, R. Beams, N. C. Lindquist, S. G. Rodrigo, L. Novotny, and S.-H. Oh, "Highly reproducible near-field optical imaging with sub-20-nm resolution based on template-stripped gold pyramids," *Acs Nano*, vol. 6, no. 10, pp. 9168–9174, 2012.

[79] A. Zehtabi-Oskuie, A. A. Zinck, R. M. Gelfand, and R. Gordon, "Template stripped double nanohole in a gold film for nano-optical tweezers," *Nanotechnology*, vol. 25, no. 49, p. 495301, 2014.

[80] Y. Harada and T. Asakura, "Radiation forces on a dielectric sphere in the Rayleigh scattering regime," *Opt. Commun.*, vol. 124, no. 5, pp. 529–541, 1996.

[81] A. Ashkin, J. M. Dziedzic, J. E. Bjorkholm, and S. Chu, "Observation of a single-beam gradient force optical trap for dielectric particles," *Opt. Lett.*, vol. 11, no. 5, pp. 288–290, 1986.

[82] M. L. Juan, R. Gordon, Y. Pang, F. Eftekhari, and R. Quidant, "Self-induced back-action optical trapping of dielectric nanoparticles," *Nature Physics*, vol. 5, no. 12, pp. 915–919, 2009.

[83] K. Taguchi, H. Ueno, T. Hiramatsu, and M. Ikeda, "Optical trapping of dielectric particle and biological cell using optical fibre," *Electronics Letters*, vol. 33, no. 5, pp. 413–414, 1997.

[84] K. Taguchi, M. Tanaka, and M. Ikeda, "Optical fiber trapping in space," *Opt. Rev.*, vol. 8, no. 3, pp. 156–158, 2001.

[85] Z. Liu, C. Guo, J. Yang, and L. Yuan, "Tapered fiber optical tweezers for microscopic particle trapping: fabrication and application.," *Opt. Express*, vol. 14, no. 25, pp. 12510–12516, 2006.

[86] S. Mohanty and K. Mohanty, "Single fiber optical tweezers for manipulation of microscopic objects," *Proc. SPIE*, vol. 6441, pp. 644116–644116–8, 2007.

[87] Y. N. Mishra, N. Ingle, and S. K. Mohanty, "Trapping and two-photon fluorescence excitation of microscopic objects using ultrafast single-fiber optical tweezers," *J. Biomed. Opt.*, vol. 16, no. 10, p. 105003, 2011.

[88] Y. Zhang, Z. Liu, J. Yang, and L. Yuan, "A non-contact single optical fiber multi-optical tweezers probe: Design and fabrication," *Opt. Commun.*, vol. 285, no. 20, pp. 4068–4071, 2012.

[89] J.-B. Decombe, S. Huant, and J. Fick, "Single and dual fiber nano-tip optical tweezers: trapping and analysis," *Opt. Express*, vol. 21, no. 25, p. 30521, 2013.

[90] J. B. Decombe, S. K. Mondal, D. Kumbhakar, S. S. Pal, and J. Fick, "Single and multiple microparticle trapping using non-gaussian beams from optical fiber nanoantennas," *IEEE J. Sel. Top. Quantum Electron.*, vol. 21, no. 4, 2015.

[91] J.-B. Decombe, F. J. Valdivia-Valero, G. Dantelle, G. Leménager, T. Gacoin, G. Colas des Francs, S. Huant, and J. Fick, "Luminescent nanoparticle trapping with far-field optical fiber-tip tweezers," *Nanoscale*, vol. 8, no. 9, pp. 5334–5342, 2016.

[92] Z. Liu, Y. Chen, L. Zhao, Y. Zhang, Y. Wei, Z. Zhu, J. Yang, and L. Yuan, "Single fiber optical trapping of a liquid droplet and its application in microresonator," *Opt. Commun.*, vol. 381, pp. 371–376, 2016.

[93] C. Ti, M.-T. Ho-Thanh, Q. Wen, and Y. Liu, "Objective-lens-free fiber-based position detection with nanometer resolution in a fiber optical trapping system," *Scientific reports*, vol. 7, no. 1, p. 13168, 2017.

[94] A. Kotnala and R. Gordon, "Quantification of high-efficiency trapping of nanoparticles in a double nanohole optical tweezer," *Nano Lett.*, vol. 14, no. 2, pp. 853–856, 2014.

[95] L. Neumann, Y. Pang, A. Houyou, M. L. Juan, R. Gordon, and N. F. Van Hulst, "Extraordinary optical transmission brightens near-field fiber probe," *Nano Lett.*, vol. 11, no. 2, pp. 355–360, 2011.

[96] A. El Eter, N. M. Hameed, F. I. Baida, R. Salut, C. Filiatre, D. Nedeljkovic, E. Atie, S. Bole, and T. Grosjean, "Fiber-integrated optical nano-tweezer based on a bowtie-aperture nano-antenna at the apex of a SNOM tip," *Opt. Express*, vol. 22, no. 8, p. 10072, 2014.

[97] M. Polyanskiy, "Refractiveindex. info-refractive index database," *RefractiveIndex. INFO,[Online]. Available: http://refractiveindex. info/.[Accessed 25 Jan 2016]*, 2018.

[98] A. D. Yaghjian, "An overview of near-field antenna measurements," *IEEE Trans. Antennas Propag.*, vol. 34, no. 1, pp. 30–45, 1986.

[99] T. K. Sarkar and A. Taaghol, "Near-field to near/far-field transformation for arbitrary near-field geometry utilizing an equivalent electric current and MoM," *IEEE Trans. Antennas Propag.*, vol. 47, no. 3, pp. 566–573, 1999.

[100] F. D'Agostino, F. Ferrara, C. Gennarelli, R. Guerriero, and M. Migliozzi, "Far-field pattern reconstruction from a nonredundant plane-polar near-field sampling arrangement: experimental testing," *IEEE Antennas Wirel. Propag. Lett.*, vol. 15, pp. 1345–1348, 2016.

[101] G. P. Agrawal, *Fiber-Optic Communication Systems*, vol. 222. John Wiley & Sons, 2012.

[102] H. Raether, "Surface plasmons on smooth surfaces," in *Surface Plasmons on Smooth and Rough Surfaces and on Gratings*, pp. 1–37, Springer, 1988.

[103] W. L. Barnes, A. Dereux, and T. W. Ebbesen, "Surface plasmon subwavelength optics," *Nature*, vol. 424, no. 6950, p. 824, 2003.

[104] S. A. Maier, *Plasmonics: Fundamentals and Applications*. Springer Science & Business Media, 2007.

[105] E. Kretschmann and H. Raether, "Radiative decay of non radiative surface plasmons excited by light," *Zeitschrift für Naturforschung A*, vol. 23, no. 12, pp. 2135–2136, 1968.

[106] A. Otto, "Excitation of nonradiative surface plasma waves in silver by the method of frustrated total reflection," *Zeitschrift für Physik A Hadrons and Nuclei*, vol. 216, no. 4, pp. 398–410, 1968.

[107] B. Hecht, H. Bielefeldt, L. Novotny, Y. Inouye, and D. Pohl, "Local excitation, scattering, and interference of surface plasmons," *Physical Review Letters*, vol. 77, no. 9, p. 1889, 1996.

[108] H. Ditlbacher, J. R. Krenn, N. Félidj, B. Lamprecht, G. Schider, M. Salerno, A. Leitner, and F. R. Aussenegg, "Fluorescence imaging of surface plasmon fields," *Applied Physics Letters*, vol. 80, no. 3, pp. 404–406, 2002.

[109] E. Devaux, T. W. Ebbesen, J.-C. Weeber, and A. Dereux, "Launching and decoupling surface plasmons via micro-gratings," *Applied Physics Letters*, vol. 83, no. 24, pp. 4936–4938, 2003.

[110] J. Homola, I. Koudela, and S. S. Yee, "Surface plasmon resonance sensors based on diffraction gratings and prism couplers: sensitivity comparison," *Sensors and Actuators B: Chemical*, vol. 54, no. 1-2, pp. 16–24, 1999.

[111] M. L. Juan, M. Righini, and R. Quidant, "Plasmon nano-optical tweezers," *Nature Photonics*, vol. 5, no. 6, p. 349, 2011.

[112] J. R. Moffitt, Y. R. Chemla, S. B. Smith, and C. Bustamante, "Recent advances in optical tweezers," *Annual Review of Biochemistry*, vol. 77, 2008.

[113] R. Gordon, "Biosensing with nanoaperture optical tweezers," *Optics & Laser Technology*, vol. 109, pp. 328–335, 2019.

[114] R. Regmi, A. A. Al Balushi, H. Rigneault, R. Gordon, and J. Wenger, "Nanoscale volume confinement and fluorescence enhancement with double nanohole aperture," *Scientific Reports*, vol. 5, p. 15852, 2015.

[115] J. Wenger, D. Gérard, J. Dintinger, O. Mahboub, N. Bonod, E. Popov, T. W. Ebbesen, and H. Rigneault, "Emission and excitation contributions to enhanced single molecule fluorescence by gold nanometric apertures," *Optics Express*, vol. 16, no. 5, pp. 3008–3020, 2008.

[116] D. Gérard, J. Wenger, N. Bonod, E. Popov, H. Rigneault, F. Mahdavi, S. Blair, J. Dintinger, and T. W. Ebbesen, "Nanoaperture-enhanced fluorescence: Towards higher detection rates with plasmonic metals," *Physical Review B*, vol. 77, no. 4, p. 045413, 2008.

[117] G. Lu, W. Li, T. Zhang, S. Yue, J. Liu, L. Hou, Z. Li, and Q. Gong, "Plasmonic-enhanced molecular fluorescence within isolated bowtie nano-apertures," *ACS Nano*, vol. 6, no. 2, pp. 1438–1448, 2012.

[118] R. A. Jensen, I. C. Huang, O. Chen, J. T. Choy, T. S. Bischof, M. Loncar, and M. G. Bawendi, "Optical trapping and two-photon excitation of colloidal quantum dots using bowtie apertures," *ACS Photonics*, vol. 3, no. 3, pp. 423–427, 2016.

[119] A. Degiron, H. Lezec, N. Yamamoto, and T. Ebbesen, "Optical transmission properties of a single subwavelength aperture in a real metal," *Optics Communications*, vol. 239, no. 1-3, pp. 61–66, 2004.

[120] Y. Pang and R. Gordon, "Nanophotonics using a subwavelength aperture in a metal film," *Nanotechnology Reviews*, vol. 1, no. 4, pp. 339–362, 2012.

[121] Y. C. Jun, K. C. Huang, and M. L. Brongersma, "Plasmonic beaming and active control over fluorescent emission," *Nature Communications*, vol. 2, p. 283, 2011.

[122] M. Davanço, M. T. Rakher, D. Schuh, A. Badolato, and K. Srinivasan, "A circular dielectric grating for vertical extraction of single quantum dot emission," *Applied Physics Letters*, vol. 99, no. 4, p. 041102, 2011.

[123] S. Ates, L. Sapienza, M. Davanco, A. Badolato, and K. Srinivasan, "Bright single-photon emission from a quantum dot in a circular bragg grating microcavity," *IEEE Journal of Selected Topics in Quantum Electronics*, vol. 18, no. 6, pp. 1711–1721, 2012.

[124] E. I. Moiseev, N. Kryzhanovskaya, Y. S. Polubavkina, M. V. Maximov, M. M. Kulagina, Y. M. Zadiranov, A. A. Lipovskii, I. S. Mukhin, A. M. Mozharov, F. E. Komissarenko, Z. F. Sadrieva, A. E. Krasnok, A. A. Bogdanov, A. V.

Lavrinenko, and A. E. Zhukov, "Light outcoupling from quantum dot-based microdisk laser via plasmonic nanoantenna," *ACS Photonics*, vol. 4, no. 2, pp. 275–281, 2017.

[125] S. K. Andersen, S. Kumar, and S. I. Bozhevolnyi, "Ultrabright linearly polarized photon generation from a nitrogen vacancy center in a nanocube dimer antenna," *Nano Letters*, vol. 17, no. 6, pp. 3889–3895, 2017.

[126] L. Li, E. H. Chen, J. Zheng, S. L. Mouradian, F. Dolde, T. Schroder, S. Karaveli, M. L. Markham, D. J. Twitchen, and D. Englund, "Efficient photon collection from a nitrogen vacancy center in a circular bullseye grating," *Nano Letters*, vol. 15, no. 3, pp. 1493–1497, 2015.

[127] H. Aouani, O. Mahboub, N. Bonod, E. Devaux, E. Popov, H. Rigneault, T. W. Ebbesen, and J. Wenger, "Bright unidirectional fluorescence emission of molecules in a nanoaperture with plasmonic corrugations," *Nano Letters*, vol. 11, no. 2, pp. 637–644, 2011.

[128] J. Dong, Z. Zhang, H. Zheng, and M. Sun, "Recent progress on plasmon-enhanced fluorescence," *Nanophotonics*, vol. 4, no. 1, pp. 472–490, 2015.

[129] H. J. Lezec, A. Degiron, E. Devaux, R. Linke, L. Martin-Moreno, F. Garcia-Vidal, and T. Ebbesen, "Beaming light from a subwavelength aperture," *Science*, vol. 297, no. 5582, pp. 820–822, 2002.

[130] L. Martin-Moreno, F. Garcia-Vidal, H. Lezec, A. Degiron, and T. Ebbesen, "Theory of highly directional emission from a single subwavelength aperture surrounded by surface corrugations," *Physical Review Letters*, vol. 90, no. 16, p. 167401, 2003.

[131] D. Lin, C. Chang, Y. Chen, D. Yang, M. Lin, J. Yeh, J. Liu, C. Kuan, C. Yeh, and C. Lee, "Beaming light from a subwavelength metal slit surrounded by dielectric surface gratings," *Optics Express*, vol. 14, no. 8, pp. 3503–3511, 2006.

[132] Y. Lim, J. Hahn, S. Kim, J. Park, H. Kim, and B. Lee, "Plasmonic light beaming manipulation and its detection using holographic microscopy," *IEEE Journal of Quantum Electronics*, vol. 46, no. 3, pp. 300–305, 2010.

[133] C. Genet and T. Ebbesen, "Light in tiny holes," in *Nanoscience And Technology: A Collection of Reviews from Nature Journals*, pp. 205–212, World Scientific, 2010.

[134] A. Angelini, E. Barakat, P. Munzert, L. Boarino, N. De Leo, E. Enrico, F. Giorgis, H. P. Herzig, C. F. Pirri, and E. Descrovi, "Focusing and extraction of light mediated by bloch surface waves," *Scientific Reports*, vol. 4, p. 5428, 2014.

[135] A. A. Saleh, S. Sheikhoelislami, S. Gastelum, and J. A. Dionne, "Grating-flanked plasmonic coaxial apertures for efficient fiber optical tweezers," *Optics Express*, vol. 24, no. 18, pp. 20593–20603, 2016.

[136] S. K. Andersen, S. Bogdanov, O. Makarova, Y. Xuan, M. Y. Shalaginov, A. Boltasseva, S. I. Bozhevolnyi, and V. M. Shalaev, "Hybrid plasmonic bullseye antennas for efficient photon collection," *ACS Photonics*, vol. 5, no. 3, pp. 692–698, 2018.

[137] F. Werschler, B. Lindner, C. Hinz, F. Conradt, P. Gumbsheimer, Y. Behovits, C. Negele, T. de Roo, O. Tzang, S. Mecking, *et al.*, "Efficient emission enhancement of single cdse/cds/pmma quantum dots through controlled near-field coupling to plasmonic bullseye resonators," *Nano Letters*, vol. 18, no. 9, pp. 5396–5400, 2018.

[138] H. Shen, G. Lu, Y. He, Y. Cheng, H. Liu, and Q. Gong, "Directional and enhanced spontaneous emission with a corrugated metal probe," *Nanoscale*, vol. 6, no. 13, pp. 7512–7518, 2014.

[139] L. Neumann, Y. Pang, A. Houyou, M. L. Juan, R. Gordon, and N. F. van Hulst, "Extraordinary optical transmission brightens near-field fiber probe," *Nano Letters*, vol. 11, no. 2, pp. 355–360, 2010.

[140] S. Kang, H.-E. Joe, J. Kim, Y. Jeong, B.-K. Min, and K. Oh, "Subwavelength plasmonic lens patterned on a composite optical fiber facet for quasi-one-dimensional bessel beam generation," *Applied Physics Letters*, vol. 98, no. 24, p. 241103, 2011.

[141] G. Kostovski, P. R. Stoddart, and A. Mitchell, "The optical fiber tip: An inherently light-coupled microscopic platform for micro-and nanotechnologies," *Advanced Materials*, vol. 26, no. 23, pp. 3798–3820, 2014.

[142] M. Principe, M. Consales, A. Micco, A. Crescitelli, G. Castaldi, E. Esposito, V. La Ferrara, A. Cutolo, V. Galdi, and A. Cusano, "Optical fiber meta-tips," *Light: Science & Applications*, vol. 6, no. 3, p. e16226, 2017.

[143] H. Lee, J. Park, and K. Oh, "Recent progress in all-fiber non-gaussian optical beam shaping technologies," *Journal of Lightwave Technology*, 2018.

[144] J. M. Ehtaiba and R. Gordon, "Template-stripped nanoaperture tweezer integrated with optical fiber," *Optics Express*, vol. 26, no. 8, pp. 9607–9613, 2018.

[145] O. Mahboub, S. C. Palacios, C. Genet, F. Garcia-Vidal, S. G. Rodrigo, L. Martin-Moreno, and T. Ebbesen, "Optimization of bull's eye structures for transmission enhancement," *Optics Express*, vol. 18, no. 11, pp. 11292–11299, 2010.

[146] U. Bog, K. Huska, F. Maerkle, A. Nesterov-Mueller, U. Lemmer, and T. Mappes, "Design of plasmonic grating structures towards optimum signal discrimination for biosensing applications," *Optics Express*, vol. 20, no. 10, pp. 11357–11369, 2012.

[147] T. Sharma, H. Kwon, J. Park, S. Han, G. Son, Y. Jung, and K. Yu, "Coupling performance enhancement using SOI grating coupler design," *Optics Communications*, vol. 427, pp. 452–456, 2018.

[148] R. Chriki, A. Yanai, J. Shappir, and U. Levy, "Enhanced efficiency of thin film solar cells using a shifted dual grating plasmonic structure," *Optics Express*, vol. 21, no. 103, pp. A382–A391, 2013.

[149] A. Kumar, J.-C. Weeber, A. Bouhelier, F. Eloi, S. Buil, X. Quélin, M. Nasilowski, B. Dubertret, J.-P. Hermier, and G. C. Des Francs, "Spatially uniform enhancement of single quantum dot emission using plasmonic grating decoupler," *Scientific Reports*, vol. 5, p. 16796, 2015.

[150] B. Chen, A. Wood, A. Pathak, J. Mathai, S. Bok, H. Zheng, S. Hamm, S. Basuray, S. Grant, K. Gangopadhyay, *et al.*, "Plasmonic gratings with nano-protrusions made by glancing angle deposition for single-molecule super-resolution imaging," *Nanoscale*, vol. 8, no. 24, pp. 12189–12201, 2016.

[151] D. T. Vu, H.-W. Chiu, R. Nababan, Q. M. Le, S.-W. Kuo, L.-K. Chau, C.-C. Ting, H.-C. Kan, and C. C. Hsu, "Enhancing upconversion luminescence emission of rare earth nanophosphors in aqueous solution with thousands fold enhancement factor by low refractive index resonant waveguide grating," *ACS Photonics*, 2018.

[152] P. B. Johnson and R.-W. Christy, "Optical constants of the noble metals," *Physical Review B*, vol. 6, no. 12, p. 4370, 1972.

[153] X. Shou, A. Agrawal, and A. Nahata, "Role of metal film thickness on the enhanced transmission properties of a periodic array of subwavelength apertures," *Optics Express*, vol. 13, no. 24, pp. 9834–9840, 2005.

[154] D. Grupp, H. Lezec, T. Ebbesen, K. Pellerin, and T. Thio, "Crucial role of metal surface in enhanced transmission through subwavelength apertures," *Applied Physics Letters*, vol. 77, no. 11, pp. 1569–1571, 2000.

[155] A. Degiron and T. Ebbesen, "Analysis of the transmission process through single apertures surrounded by periodic corrugations," *Optics Express*, vol. 12, no. 16, pp. 3694–3700, 2004.

[156] F. J. Garcia-Vidal, L. Martin-Moreno, T. Ebbesen, and L. Kuipers, "Light passing through subwavelength apertures," *Reviews of Modern Physics*, vol. 82, no. 1, p. 729, 2010.

[157] J. Berthelot, S. Aćimović, M. Juan, M. Kreuzer, J. Renger, and R. Quidant, "Three-dimensional manipulation with scanning near-field optical nanotweezers," *Nature Nanotechnology*, vol. 9, no. 4, pp. 295–299, 2014.

[158] L. Mandel, "Squeezed states and sub-poissonian photon statistics," *Physical Review Letters*, vol. 49, no. 2, p. 136, 1982.

[159] X. Zou and L. Mandel, "Photon-antibunching and sub-poissonian photon statistics," *Physical Review A*, vol. 41, no. 1, p. 475, 1990.

[160] R. Short and L. Mandel, "Observation of sub-poissonian photon statistics," *Physical Review Letters*, vol. 51, no. 5, p. 384, 1983.

[161] S.-O. Flyckt, *Photomultiplier Tubes: Principles and Applications*. Photonis, 2002.

[162] S. Cova, M. Ghioni, M. A. Itzler, J. C. Bienfang, and A. Restelli, "Semiconductor-based detectors," in *Experimental Methods in the Physical Sciences*, vol. 45, pp. 83–146, Elsevier, 2013.

[163] G. Gol'Tsman, O. Okunev, G. Chulkova, A. Lipatov, A. Semenov, K. Smirnov, B. Voronov, A. Dzardanov, C. Williams, and R. Sobolewski, "Picosecond superconducting single-photon optical detector," *Applied Physics Letters*, vol. 79, no. 6, pp. 705–707, 2001.

[164] C. M. Natarajan, M. G. Tanner, and R. H. Hadfield, "Superconducting nanowire single-photon detectors: Physics and applications," *Superconductor Science and Technology*, vol. 25, no. 6, p. 063001, 2012.

[165] S. Ferrari, C. Schuck, and W. Pernice, "Waveguide-integrated superconducting nanowire single-photon detectors," *Nanophotonics*, vol. 7, no. 11, pp. 1725–1758, 2018.

[166] L. Zhang, L. You, X. Yang, J. Wu, C. Lv, Q. Guo, W. Zhang, H. Li, W. Peng, Z. Wang, *et al.*, "Hotspot relaxation time of nbn superconducting nanowire single-photon detectors on various substrates," *Scientific Reports*, vol. 8, no. 1, p. 1486, 2018.

[167] S. Miki, M. Fujiwara, M. Sasaki, B. Baek, A. J. Miller, R. H. Hadfield, S. W. Nam, and Z. Wang, "Large sensitive-area nbn nanowire superconducting single-photon detectors fabricated on single-crystal mgo substrates," *Applied Physics Letters*, vol. 92, no. 6, p. 061116, 2008.

[168] R. Ghosh and L. Mandel, "Observation of nonclassical effects in the interference of two photons," *Physical Review Letters*, vol. 59, no. 17, p. 1903, 1987.

[169] M. Fox, *Quantum Optics: An Introduction*, vol. 15. OUP Oxford, 2006.

# Appendix A

## A.1 UCNPs: image and emission spectrum

Figure A.1 shows a TEM image of the commercial UCNPs, $\beta - NaYF_4$:20 %$Yb^{3+}$/2 %$Er^{3+}$, from Sigma_Aldrich. The average size of the particles is 30 nm. Figure A.2 shows the emission spectrum of a dense group of particles on 100 nm gold film that are excited by a $\sim$ 0.25 mW laser at 980 nm wavelength. A schematic diagram of the experimental setup used to measure the emission spectra for the UCNPs is shown in figure A.3.

According to the source, these UCNPs have the following properties:

- Physical form: Lyophilized, white crystal
- Excitation wavelength: 976 nm
- Emission maximum: 545 nm
- Morphology: Rods
- Diameter: 10 - 60 nm
- Bioconjugate: PEG (no bioconjugation)
- Crystal Host: Sodium Yttrium Fluoride ($NaYF_4$)

- Activators: Ytterbium (Yb), Erbium (Er)
- Crystal Formula: $NaYF_4$, Yb, Er

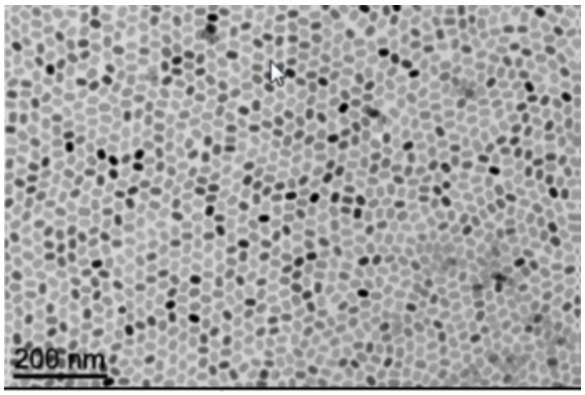


**Figure A.1** – TEM image of the $\beta - NaYF_4{:}20\,\%Yb^{3+}/2\,\%Er^{3+}$ UCNPs. image source SIGMA-ALDRICH, product number 42923, `http://www.sigmaaldrich.com/content/dam/sigma-aldrich/docs/Sigma/Datasheet/10/42923dat.pdf`

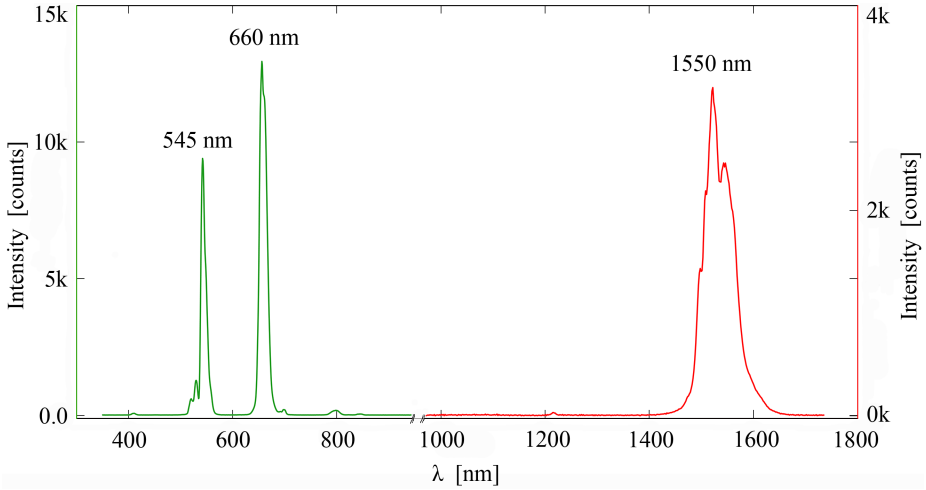


**Figure A.2** – Emission spectra of the $\beta - NaYF_4{:}20\,\%Yb^{3+}/2\,\%Er^{3+}$ UCNPs. $\lambda_{exc} = 980\,\text{nm}$ and incident power density on the dichroic mirror is $\sim 0.25\,\text{mW}/\mu\text{m}^2$.

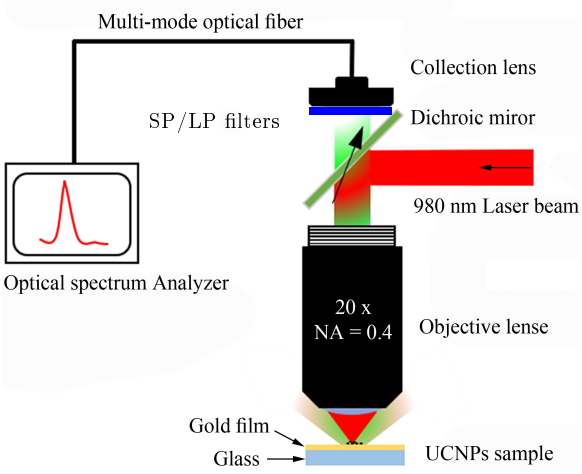


**Figure A.3** – Schematic diagram of the experimental setup used to measure the $\beta - NaYF_4$:20 %$Yb^{3+}$/2 %$Er^{3+}$ emission spectra shown in Fig. A.2. Two optical spectrometers used in this setup; 350 - 1100 nm (OceanOptics, QE65000), and 1100 - 1750 nm (OceanOptics NIR 512). SP and LP are abbreviations for Short and Long Pass filters.

## A.2 UCNPs: molecular weight vs size

Figure A.4 shows the molecular weight of the $\beta - NaYF_4$:x%$Yb^{3+}$/y%$Er^{3+}$ versus the particle's size based on theoritical study [43].

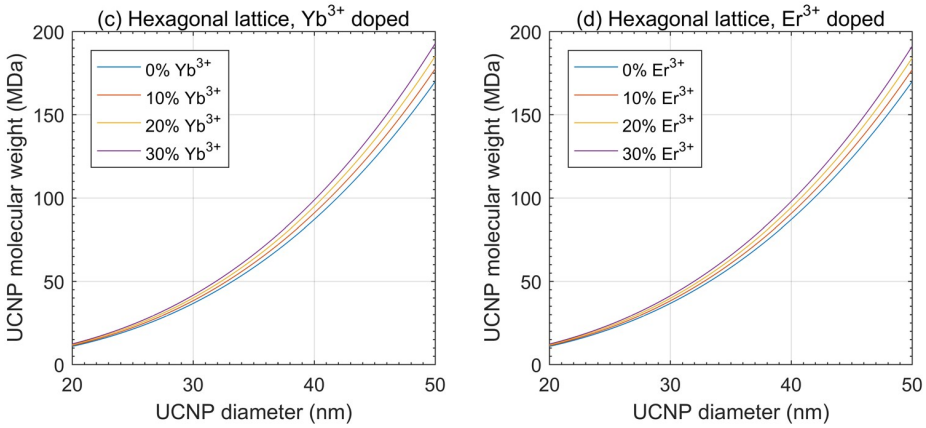


**Figure A.4** – Theoretical molecular weight of $\beta - NaYF_4$:x%$Yb^{3+}$/y%$Er^{3+}$ for different particle size. Taken from Reference [43].

# Appendix B

## B.1 Nanofabrication

Figure B.1 below illustrates a planar nanofabricated multiple circular gold films where each ring centers a nanohole, the nanoantenna. A typical nanoaperture can be viewed in Fig. B.5c. Any of the circular film can be easily template stripped onto a fiber tip.

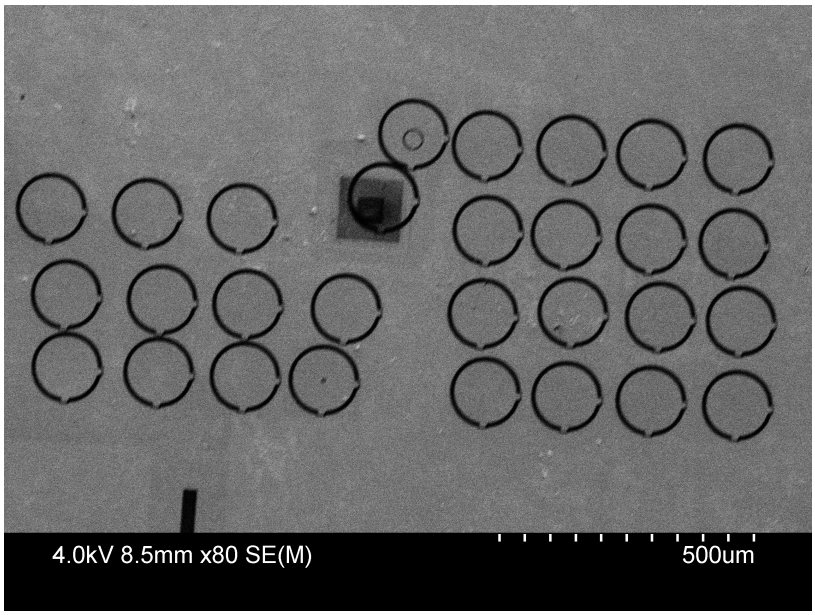


**Figure B.1** – An SEM image of planar nanofabricated multiple 100 nm thick circular gold films. Each circular film has a nanoaperture at its center that centers a nanohole.

## B.2 Bowtie nanoantenna structure and FDTD simulation

Figure B.2 below shows the bowtie nanoantenna top and bottom views. Figure B.2a shows the side of the aperture that is in contact with the fiber's cleaved end through the epoxy layer. The schematic in Fig. B.2b shows the outer side of the bowtie aperture nanoantenna. The actual FDTD software generated aperture structure is shown in Fig. B.3.

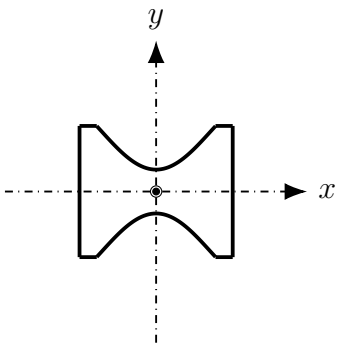


**(a)** Top aperture view

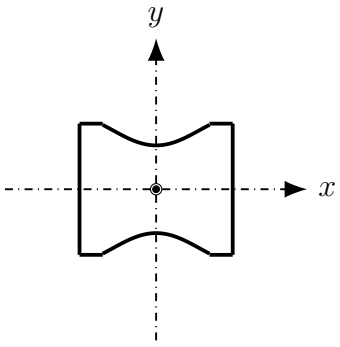


**(b)** Bottom aperture view

**Figure B.2** – Top (a) and bottom (b) views of aperture gap

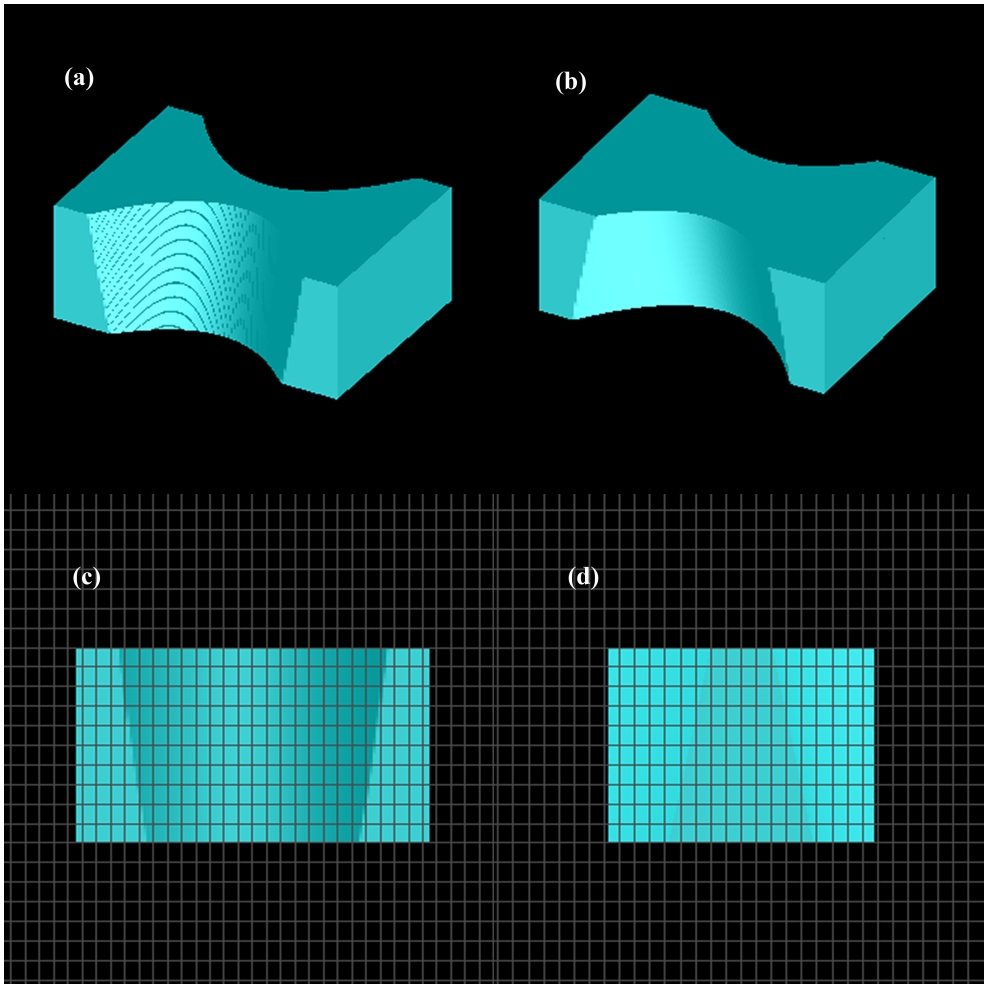


**Figure B.3** – 3D schematic diagram as generated by Lumerical FDTD software. (a) shows the upper gap ($\sim 40\,\mathrm{nm}$). (b) shows the bottom gap ($\sim 95\,\mathrm{nm}$). (c) $xz-$sectional view, and (d) is the $yz-$sectional view.

## B.3 980 nm plane wave source FDTD simulation

Figure B.4 schematically shows an $yz$-plane view of the FDTD simulation region which consists of: an epoxy layer, a 100 nm gold film with the bowtie aperture in its center, water region. A plane wave source polarized along the $y$-axis as shown in Fig. B.4b is used to excite the aperture from the epoxy side. It was injected in the computational space as a plane wave at $z = -2.305\,\mu$m. A 2D monitor is located in the $xy$-plane on the film surface ($z = 0.1\,\mu$m) to record all the field data including the aperture nanoantenna. The refractive index and the size of each of the 3D

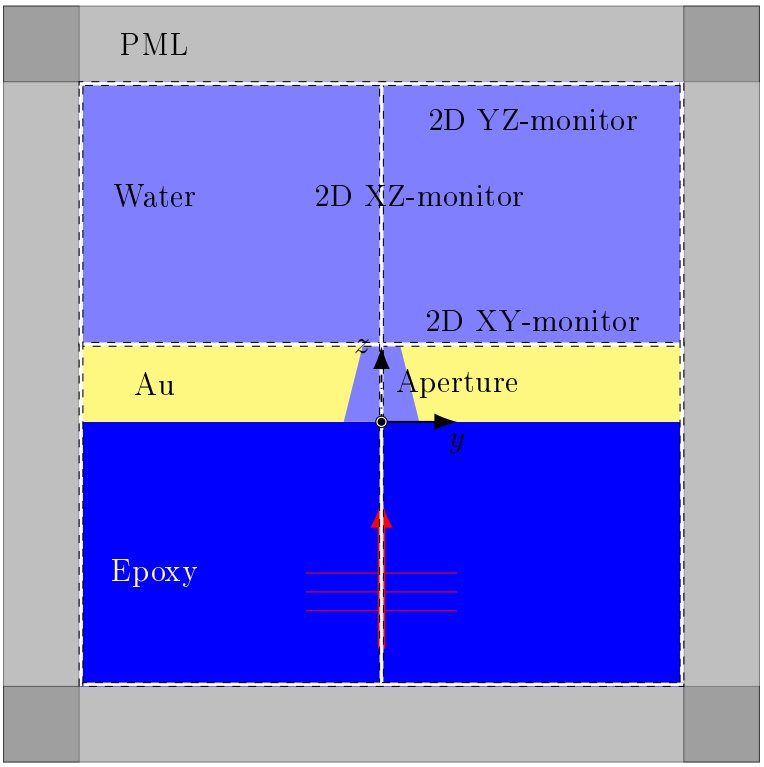


**(a)** 980 nm $yz$-plane FDTD 3D simulation region.

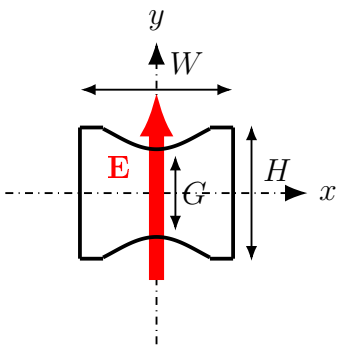


**(b)** Epoxy-side of the bowtie aperture with the red arrow represents polarization of electric field of the incident plane wave shown in (a).

**Figure B.4** – Schematic diagram ($yz$-plane view)of the FDTD simulation region for the electric field intensity profiles shown in Fig. 3.7. The simulation region size is $10\,\mu\text{m}\times10\,\mu\text{m}\times5\,\mu$m. The 2D monitors have dimensions over the entire plane space of each in the FDTD region. The XY-monitor is located at $z = 0.1\,\mu$m, the XZ-monitor is located at $y = 0$, and the YZ-monitor is located at $x = 0$ perpendicular to the XZ-monitor.

simulation regions as well as the aperture size are summarized in Table B.1. The 3D shape of the bowtie hole is shown in Fig. B.2 and its refractive index was set to 1.33 (assuming the hole is filled with water).

**Table B.1** – FDTD simulation data used to produce results shown in Section 3.2.2.1.

| Layer/structure | Dielectric constant, $\epsilon$ | Maximum span, $x \times y \times z$ (each in $\mu$m) |
|---|---|---|
| Epoxy layer | | $10 \times 10 \times 2.5$ |
| 980 nm | 2.3898 | |
| 1540 nm | 2.3746 | |
| Gold film | | $10 \times 10 \times 0.1$ |
| 980 nm | $-39.897 + i2.7534$ | |
| 1540 nm | $-113.46 + i11.050$ | |
| Water | 1.7689 | fills the aperture volume |
| Aperture | 1.76893 | $0.275 \times 0.175 \times 0.100$ |

## B.4 Template stripping of the nanoaperture

Figure B.5a shows the various fabrication and integration steps for the NAFT. In step 1, we evaporate a 100 nm thick gold film on a clean glass substrate without an adhesion layer. The SEM images(b) and (c) show step 2, where we use the FIB to cut the evaporated gold film into multiple circular films, each of 125 $\mu$m inner diameter and has a bowtie-shaped nanoaperture at the center. We chose the 125 $\mu$m diameter for the circular films to match the size of the SMF.

Step 3 shows that multiple circular gold films with apertures were milled in a single sample, allowing for the production of many optical fiber probes with a nanoantenna at the tip from a single FIB nanofabrication run. In step 4, we use the setup in Fig. B.5d to align the optical fiber channel with the nanoantenna, perpendicular to

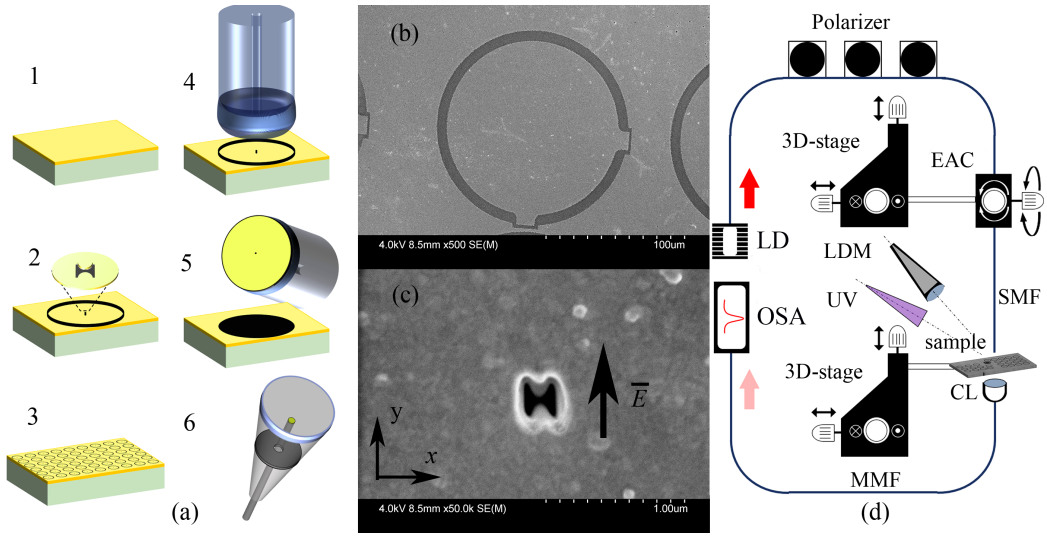


**Figure B.5** – (a) Schematics for the different NAFT integration steps. (b) SEM image of a 100 nm Au film after being milled using the FIB, the ring inner diameter is 125 $\mu$m and the outer diameter is 140 $\mu$m. (c) SEM image for the plasmonic aperture. The aperture gap is $\sim$ 70nm along the y-axis. The black arrow shows the optimum polarization for maximum field confinement and transmission. (d) Schematic for the setup used to integrate the NAFT. LD is laser source (980 nm), EAC is azimuthal and elevation angle controller, LDM is long distance microscope, UV is ultra-violet light source, CL is collimator, MMF is multimode fiber, and OSA is an optical spectrometer.

the gold film. Next, we retract the cleaved-end optical fiber probe using the upper 3D-stage and insert a glass-slide with $\sim$ 5.0 $\mu$L drop of UV-curable epoxy (Norland NOA 61). The cleaved-end fiber can then be carefully immersed in the epoxy drop for a few seconds and retract it up to allow removing the epoxy glass-slide. We then moved the fiber probe so that it is about $\sim 100 - 500\,\mu$m off the targeted circular gold film. Also, we used the top and bottom 3D-stages to align the fiber with the nanoantenna in the targeted gold film by sending light through the optical fiber probe and monitor it on the other side of the film. To improve the alignment process, we used a fiber polarizer where a maximum transmission through the nanoantenna was easy to observe on the spectrometer. Ultimately, at the point of contact, we cure the epoxy to become hardened with a UV light for about 5 minutes.

As shown in step 5, we retracted the fiber, using the upper 3D-stage, with the

gold film attached to the tip. Finally, to provide a mechanical protection for the integrated optical fiber probe, we use a plastic cone (or a glass tube) as shown in step 6. The gap between the fiber-head and the cone-base can be purposely adjusted.

## B.5 Curable epoxy

The ultra-violet curable epoxy used in integrating the optical tweezer is from Norland Products Inc. The epoxy type used is Norland Optical Adhesive 61 (NOA 61). It is a colorless liquid photopolymer that cures when exposed to ultraviolet light. Figure B.6 below shows a graph of the refractive index of the material at 25 °C for a wide range of optical wavelengths. Transmission through this material versus wavelength is also shown in Fig. B.7.

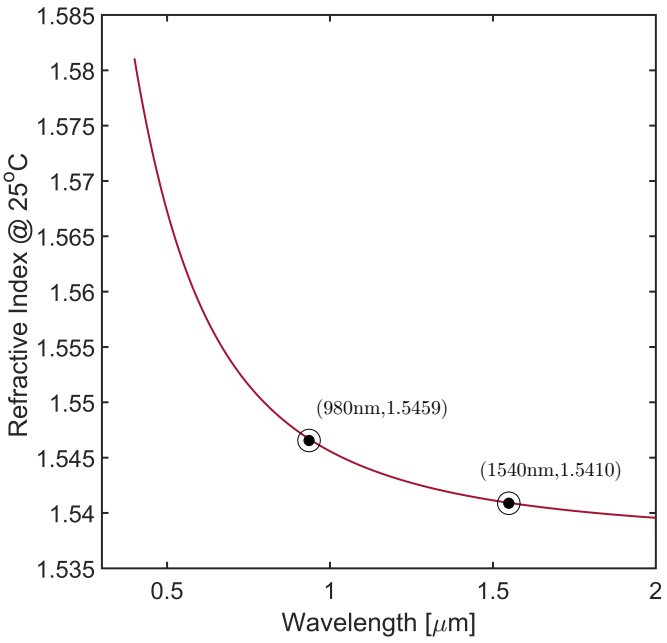


**Figure B.6** – Epoxy NOA61 index of refraction at 25 °C. Graph reproduced according to the formula given by Noland Product Inc.: $n = 1.5375 + \frac{8290.45}{\lambda^2} - \frac{2.11046\times10^8}{\lambda^4}$, where $\lambda$ is in nm.

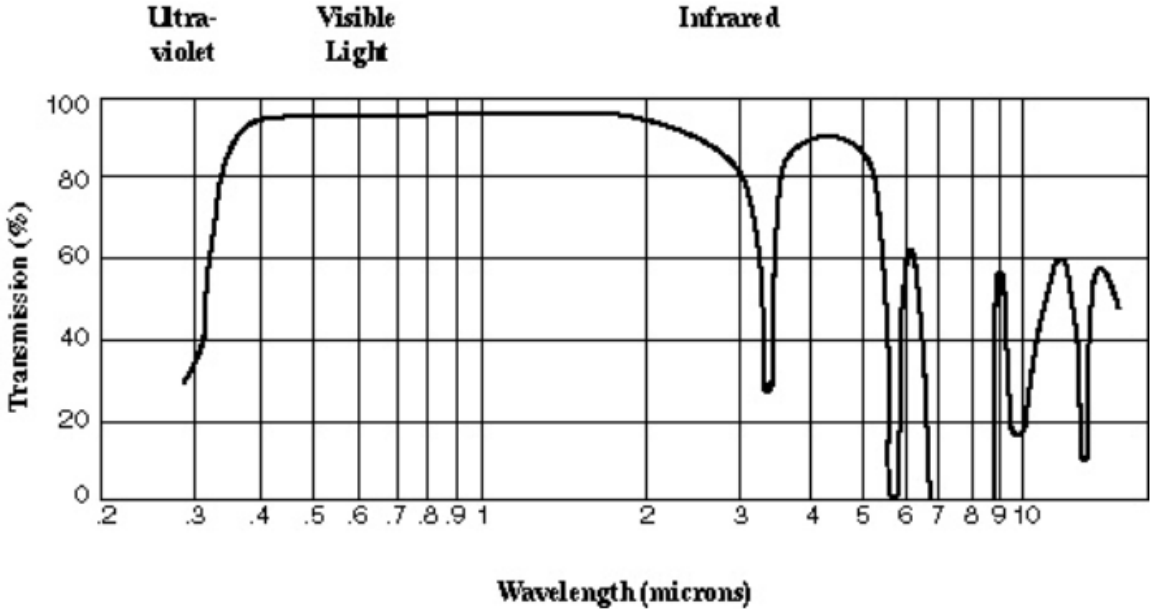


**Figure B.7** – Epoxy NOA61 spectral transmission. Graph copied from Noland Products Inc.: `https://www.norlandprod.com/adhesives/noa%2061.html`

## B.6 Nanoparticles optical trapping

Figure B.8 shows long time traces for UCNPs ($\beta$-$NaYF_4$:20%$Yb^{3+}$/2%$Er^{3+}$) trapping signals recorded using Avalanche Photo Detector, APD. The time signal that is shown in Fig. B.8a is for the case when a pure hexane is used as a trap medium, whereas the time that is signal shown in Fig. B.8a is for the case when the trap medium is a suspension of hexane contains UCNPs, $1.5\,mg/mL$. The trapping signal time record shows a repeatable short time trapping events ($\sim 150\,\text{ms}$). The two time signal were obtained using the setup illustrated in Fig. 4.6b.

The highlighted portions of the two signals appearing as light-red in Fig. B.8 represent the time samples that have been discussed in Section 4.3.2 to demonstrate the trapping process of UCNPs using the optical fiber tweezer, NAFT.

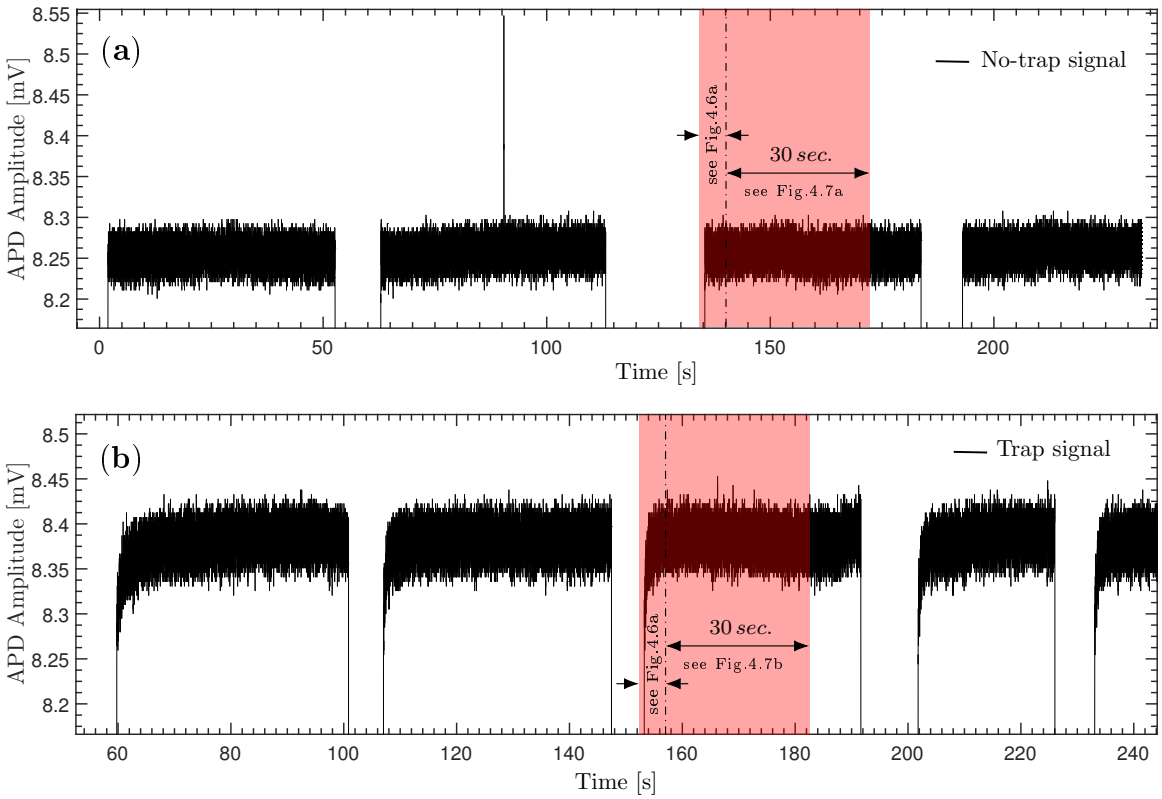


**Figure B.8** – UCNPs' trapping signal traces with 10 kHz sampling frequency. (**a**) No-trap signal and (**b**) trap signal. More details on the highlighted (red-colored) time windows are given in Section 4.3.2. The high lighted time domains are not exact in this figure.

### B.6.1 Trapping-jump of a 25nm polystyrene nanosphere in water

Figure B.9 shows the FDTD simulation of a 25 nm polystyrene nanosphere located close to one edge of the bowtie nanoantenna trapping gap. The simulation results show an increase in the APD received power when the particle is positioned (trapped) at the high field strength within the antenna gap.

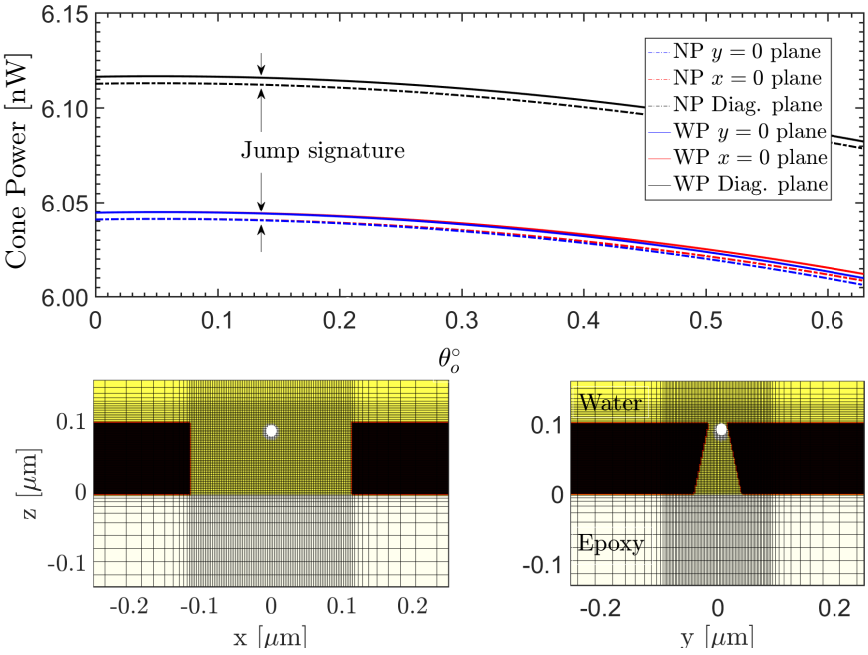


**Figure B.9** – FDTD simulation of a 25 nm polystyrene nanosphere trapping jump (top panel). The sphere is not centered in the gap (bottom right panel), rather it is positioned close to the gap crust.

# Appendix C

This appendix contains two parts that are devoted to giving more details about theoretical and experimental approaches handled in Chapters 5 and 6. In the first part (Section C.1), we demonstrate the dispersion relation of electromagnetic fields supported at a metal-dielectric interface. This part is crucial because it shows how electromagnetic energy, in the form of surface plasmon polariton waves, can be bound to a metal-dielectric interface. This confined electromagnetic energy can be exploited to enhance light transmission through nanoaperture/s perforated in metal films, as we have demonstrated in Chapter 5.

In the second part (Section C.2), we demonstrate photon-counting results for artificial and experimental data that were partially handled in Chapter 6. The experimental results shown in this part reveals the photon statistics of light detected by a two-channel SNSPD using the NAFT in optical trapping measurements on the UCNPs. We have also supported the real data photon statistics calculations by simulating the artificial photon streams.

## C.1 Dispersion relation of SPP wave at a metal-dielectric interface

Nobel metals are characterized by a dielectric constant, $\epsilon_m = \epsilon_m^{'} + j\epsilon_m^{''}$, where, assuming non-magnetic material, each of the real and imaginary parts can be expressed as [104]:

$$\epsilon_m^{'} = 1 - \frac{\omega_p^2}{\omega^2 + \zeta^2}, \tag{C.1}$$

$$\epsilon_m^{''} = \frac{\zeta\omega_p^2}{\omega(\omega^2 + \zeta^2)}, \tag{C.2}$$

where $\omega$ is the excitation frequency, $\omega_p$ is the plasma frequency, and $\zeta$ is the electron collision frequency.

Figure C.1 shows a geometry of an interface of gold, of relative permittivity $\epsilon_g$, and dielectric material of positive and real dielectric constant $\epsilon_d$. Assume a p-polarized TM$^x$ wave with time-harmonic electromagnetic field components $(E_x, E_z, H_y)$, of the form $e^{j\omega t}$, that propagates in the positive $x$-direction with a propagation constant $\beta$. Starting with Faraday's and Ampere's laws of Maxwell's curl equations,

$$\nabla \times \mathbf{E} = -j\omega\mu\mathbf{H} \tag{C.3}$$

$$\nabla \times \mathbf{H} = j\omega\epsilon\mathbf{E} \tag{C.4}$$

moreover, because the geometry of the interface is uniform in the y-direction ($\frac{\partial}{\partial y} = 0$), these curl equations can be rearranged into the following three equations:

$$\frac{\partial E_x}{\partial z} + j\beta E_z = -j\omega\mu H_y \tag{C.5}$$

$$\frac{\partial H_y}{\partial z} = -j\omega\epsilon E_x \tag{C.6}$$

$$\beta H_y = -\omega\epsilon E_z \tag{C.7}$$

Concerning Fig. C.1, an SPP mode is characterized by a decaying field away in the

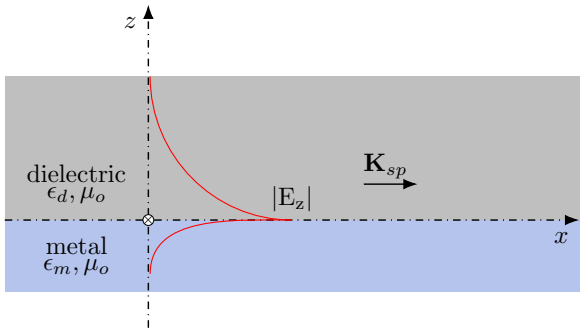


**Figure C.1** – Metal-dielectric interface. The red line represents an evanescent SPP wave that propagates in the positive $x-$direction and decays into the metal and the dielectric material, and perpendicular to the interface.

z-direction in the two regions forming the interface and propagating in the positive x-direction. Therefore, we can assume a solution of the form:

$$\mathbf{E}^i = ({E_x}^i, {E_z}^i)e^{-\alpha_i|z|}e^{-j\beta x} \tag{C.8}$$

$$\mathbf{H}^i = {H_y}^i e^{-\alpha_i|z|}e^{-j\beta x} \tag{C.9}$$

$$i = \begin{cases} d & \forall\, z \geq 0 \\ g & \forall\, z \leq 0 \end{cases} \tag{C.10}$$

where $d$ and $g$ denote either the upper region (dielectric) or the bottom region (gold), and $\alpha_i$ is a positive real-part number representing decay factor. $E_x$, $E_z$, $H_y$ represent field component amplitudes. By substituting these solutions into Equations (C.5)-(C.7) for each region, we get the following two sets of equations:

$$\alpha_d {E_x}^d - j\beta {E_z}^d = j\omega\mu_o\mu_d {H_y}^d \tag{C.11}$$

$$\alpha_d {H_y}^d = j\omega\epsilon_o\epsilon_d {E_x}^d \tag{C.12}$$

$$\beta {H_y}^d = -\omega\epsilon_o\epsilon_d {E_z}^d \tag{C.13}$$

and

$$\alpha_g {E_x}^g + j\beta {E_z}^g = -j\omega\mu_o\mu_g {H_y}^g \tag{C.14}$$

$$\alpha_g {H_y}^g = -j\omega\epsilon_o\epsilon_g {E_x}^g \tag{C.15}$$

$$\beta {H_y}^g = -\omega\epsilon_o\epsilon_g {E_z}^g. \tag{C.16}$$

We can further, using Eqs.(C.13) and (C.16), rearrange the two sets of equations so that, in terms of the electric and magnetic field amplitudes, they become functions of only the field component amplitudes $E_x$ and $H_y$, as follows:

$$\alpha_d {E_x}^d = \frac{j}{\omega\epsilon_o\epsilon_d}({K_o}^2\mu_d\epsilon_d - \beta^2){H_y}^d \tag{C.17}$$

$$\frac{1}{\alpha_d}{E_x}^d = \frac{-j}{\omega\epsilon_o\epsilon_d}{H_y}^d \tag{C.18}$$

$$\alpha_g {E_x}^g = \frac{-j}{\omega\epsilon_o\epsilon_g}({K_o}^2\mu_g\epsilon_g - \beta^2){H_y}^g \tag{C.19}$$

$$\frac{1}{\alpha_g}{E_x}^g = \frac{j}{\omega\epsilon_o\epsilon_g}{H_y}^g, \tag{C.20}$$

where $K_o$ is the free-space wavevector. Solving the two sets of the previous equations yields dispersion relations in the two regions of the following form:

$${\alpha_i}^2 = \beta^2 - {K_o}^2\mu_i\epsilon_i, \tag{C.21}$$

which shows that the surface wave propagation constant must be greater than the propagation constant of light in either of the two media.

Using Equations C.18 and C.20, and applying the boundary conditions at the interface, ${E_x}^d = {E_x}^g$ and ${H_y}^d = {H_y}^g$, we can get the following relation:

$$\frac{\alpha_d}{\epsilon_d} + \frac{\alpha_g}{\epsilon_g} = 0. \tag{C.22}$$

Substituting $\alpha_d$ and $\alpha_g$ of Equation (C.22) into Equation (C.21) and solving for

$\beta$, yields the following general surface plasmon wave dispersion relation:

$$\beta = K_o \sqrt{\epsilon_d \epsilon_g \frac{(\mu_d \epsilon_g - \mu_g \epsilon_d)}{(\epsilon_g + \epsilon_d)(\epsilon_g - \epsilon_d)}}, \tag{C.23}$$

which, for nonmagnetic media, turns to the most known SPP dispersion relation,

$$\beta = K_o \sqrt{\frac{\epsilon_d \epsilon_g}{\epsilon_g + \epsilon_d}}. \tag{C.24}$$

## C.2 Single-photon measurements

### C.2.1 Artificial data simulation

The data demonstrated in Fig. C.2 represent artificial generated photon-streams data for the purpose to virtually simulate (in an approximate way) the photon-statistics of the three different kinds of light. The virtual HBT setup used in simulating these results is illustrated in Fig. 6.4. Figure C.2, parts (a,b,c), were presented in Chapter 6 and they are repeated here only for comparison. The other two figure groups, parts (d,e,f) and (g,h,i), represent the chaotic and coherent light photon statistics, respectively. The following matlab code shows the generation of the three artificial photon-streams:

**Listing C.1** – Matlab code for artificial photon-stream generation

```
N = 10000;% Total time points (photon-clicks).
mu_ChaS = 100;% Chaotic mean (arbitrary)
variance_ChaS = 1.5*mu_ChaS;% (for chaotic light, variance > mean)
sd_ChaS = sqrt(variance_ChaS);% standard deviation
rand_Chaotic = sort(rand(1,N)).^2;% squared random sequence (increase bunching)
rand_Chaotic = rand_Chaotic/max(rand_Chaotic);% normalize
%^^^^^^^^^^^^^^^^^^^^^^^^^^^^^^^^^^^^
to_LaserS = 0;% zero initialization
lambda = 1000;% exponential rate constant (for coherent light generation)
%^^^^^^^^^^^^^^^^^^^^^^^^^
dELTA = 1.0;% time spacing
t_increment = 0;% loop time increment
m= 1;% determines time step size
dt = m*dELTA;% step size
```

```
for i =1:N % looping
%^^^^^^^^^
% Quantum:
%^^^^^^^^^
t_increment = t_increment + m*dELTA;
t_QuaS(i) = t_increment;% Quantum photon-stream time vector
%^^^^^^^^^
% Chaotic:
%^^^^^^^^^
t_ChaS(i) = mu_ChaS + sd_ChaS * rand_Chaotic(i);% Chaotic photon-stream time vector
%^^^^^^^^^^
% Coherent:
%^^^^^^^^^^
t_LaserS(i) = to_LaserS + (-1/lambda) * log(1 - rand('double'));% Coherent photon-stream time vector
to_LaserS = t_LaserS(i);
end
%^^^^^^^^^^^^^^^^^^^^^^^^^^^^^^^^^^^^^^^^^^^^^^^^^^^^^^^^^^^^^^^^^^^^^^^^
% Shift to zer, normalize, and expand over N time units (msec.):
%^^^^^^^^^^^^^^^^^^^^^^^^^^^^^^^^^^^^^^^^^^^^^^^^^^^^^^^^^^^^^^^^^^^^^^^^
t_QuaS = t_QuaS - t_QuaS(1);
t_QuaS = t_QuaS/max(t_QuaS);
t_QuaS = t_QuaS*N;

t_ChaS = t_ChaS - t_ChaS(1);
t_ChaS = t_ChaS/max(t_ChaS);
t_ChaS = t_ChaS*N;

t_LaserS = t_LaserS - t_LaserS(1);
t_LaserS = t_LaserS/max(t_LaserS);
t_LaserS = t_LaserS*N;
```

### C.2.2 Real experimental data

Figure C.3 shows the experimental results regarding photon statistics, in terms of the second-order correlation function $g^{(2)}(\tau)$, for the erbium-doped UCNPs, suspended in hexane ($0.1\,\frac{mg}{ml}$). The results are shown for three apart time slots of 5.0 seconds each, within the total recorded photon clicks by the SNSPD at channels $ch1$ and $ch2$. Also, the experiments have been repeated several times for two cases; first, for pure hexane, where the optical tweezer (NAFT) was placed in hexane suspense that does not contain UCNPs, and second, for the case where the hexane contains erbium-doped UCNPs. Figures C.3(d,e,f) have been demonstrated and discussed with more details in Chapter 6.

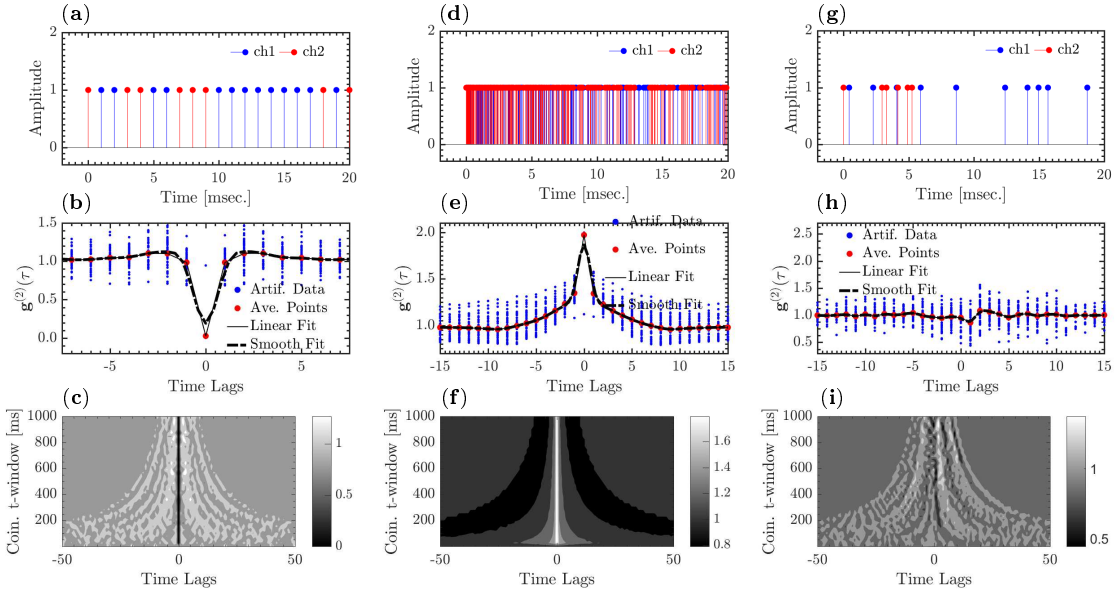


**Figure C.2** – UCNPs trapping and photon emission measurements using two-channel SNSPD. (a-c) photon-counts histograms, $g^{(2)}(\tau)$, and the contour plot of $g^{(2)}(\tau)$ versus coincidence time window, for the suspended UCNPs in hexane. Data given in (b) and (c) are the results of processing 5 sec time slot of total of 5 minutes recorded timestamps using 2-channel SNSPD. (d-f) and (g-i) are the same as (a-c) but for different time slot locations as shown in (d) and (g).

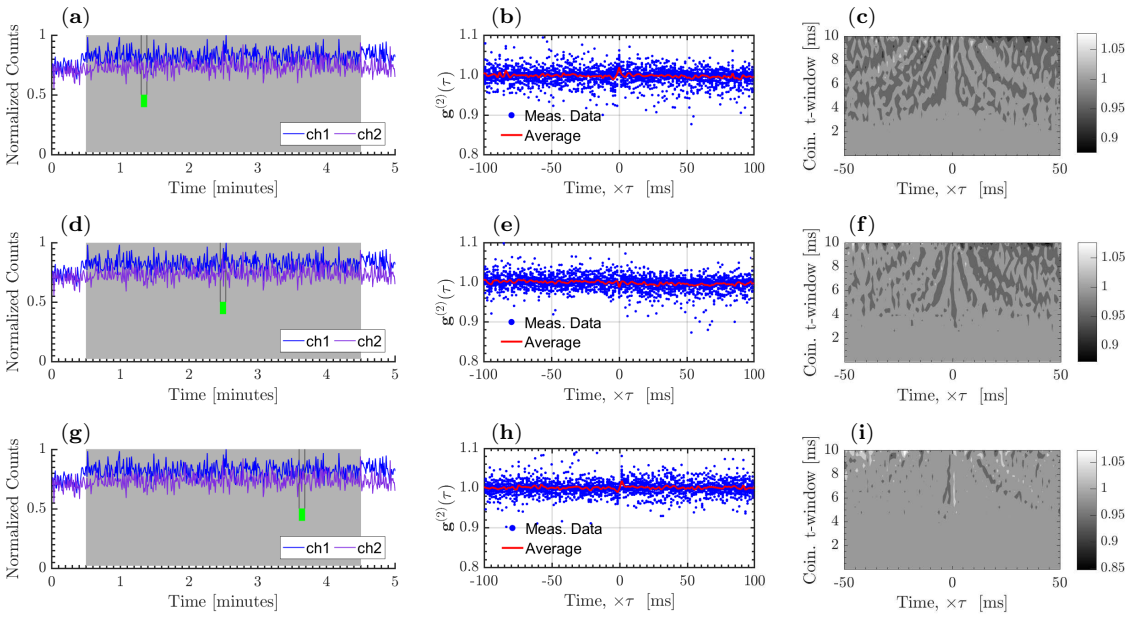


**Figure C.3** – UCNPs trapping and photon emission measurements using two-channel SNSPD. (a-c) photon-counts histograms, $g^{(2)}(\tau)$, and the contour plot of $g^{(2)}(\tau)$ versus coincidence time window, for the suspended UCNPs in hexane. Data given in (b) and (c) are the results of processing 5 sec time slot of total of 5 minutes recorded timestamps using 2-channel SNSPD. (d-f) and (g-i) are same as (a-c) but for different time slot locations as shown in (d) and (g).